2013

Nanoscale metal oxide and supported metal catalysts for Li-air battery

Kan Huang

Department: Chemical and Biochemical Engineering

NANOSCALE METAL OXIDE AND SUPPORTED METAL CATALYSTS FOR LI-AIR BATTERY

by

KAN HUANG

A DISSERTATION

Presented to the Graduate Faculty of the

MISSOURI UNIVERSITY OF SCIENCE AND TECHNOLOGY

In Partial Fulfillment of the Requirements for the Degree

DOCTOR OF PHILOSOPHY

in

CHEMICAL ENGINEERING

2013

Approved by:

Yangchuan Xing, Advisor

Douglas K. Ludlow

Xinhua Liang

Joseph D. Smith

Fatih Dogan

PUBLICATION DISSERTATION OPTION

This dissertation consists of the following five articles that have been published or pending submission for publication:

Paper I, “Increasing Pt oxygen reduction reaction activity and durability with a carbon-doped TiO_2 nanocoating catalyst support” has been published in Journal of Materials Chemistry 22(33): 16824-16832.

Paper II, “Carbothermal synthesis of titanium oxycarbide as electrocatalyst support with high oxygen evolution reaction activity” has been published in Journal of Materials Research 28(03): 454-460.

Paper III, “A hybrid Li-air battery with buckypaper air cathode and sulfuric acid electrolyte” has been published in Electrochimica Acta 81(0): 20-24.

Paper IV, “Increasing round trip efficiency of Hybrid Li-air battery with bifunctional catalysts” has been submitted to Electrochimica Acta.

Paper V, “Synthesis of niobium oxide-carbon nanotubes supported Platinum for oxygen reduction reaction”, pending submission.

ABSTRACT

The dissertation work focuses on research and development of durable nanoscale catalysts and supports for rechargeable Li-air batteries that use aqueous catholytes. Transition metal oxides, TiO_2 and Nb_2O_5 in particular, were prepared from a sol-gel process in the form of nanocoatings (5~50 nm) on carbon nanotubes (CNTs) and studied as catalyst supports. Carbon doping in the oxides and post annealing significantly increased their electronic conductivity. Pt catalyst on the support with TiO_2 (Pt/c-TiO_2/CNTs) showed a much better oxygen reduction reaction (ORR) activity than a commercial Pt on carbon black (Pt/C). Negligible loss (< 3%) in ORR activity was found in Pt/c-TiO_2/CNTs as compared to more than 50% loss in Pt/C, demonstrating a significantly improved durability in the developed catalysts. However, Pt/c-Nb_2O_5/CNTs was found to be worse in ORR activity and durability, suggesting that c-Nb_2O_5/CNTs may not be a good support.

CNTs have fibrous shape and would provide a unique porous structure as electrode. Their buckypapers were made and used to support catalysts of Pt and IrO_2 in the cathodes of Li-air batteries with sulfuric acid catholyte. At low Pt loading (5 wt.%) without IrO_2 on the buckypaper cathode, the Li-air cell achieved a discharging capacity of 306 mAh/g and a specific energy of 1067 Wh/kg at 0.2 mA/cm^2. A significant charge overpotential reduction (~ 0.3 V) was achieved when IrO_2 was also used to form a bifunctional catalyst with Pt on the buckypapers. The round trip efficiency was increased from 72% to 81% with the bifunctional cathode, demonstrating a higher energy conversion efficiency.

ACKNOWLEDGMENTS

The author would like to sincerely express his gratitude to his advisor, Dr. Yangchuan Xing, for his guidance, assistance and financial support during the completion of the work. The author would also like to thank Dr. Douglas K. Ludlow, Dr. Xinhua Liang, Dr. Joseph D. Smith and Dr. Fatih Dogan for their helpful instruction and for serving on the graduate committee. Thanks also to Dr. Yunfeng Li, Dr. Eric Bohannan, Dr. Kai Song and Mr. Brian Porter for research support.

The support from the Department of Chemical and Biochemical Engineering in Missouri University of Science and Technology and Department of Energy ARPA-E BEEST program (DE-AR00066) are greatly acknowledged.

Finally, the author would gratefully thank his parents for their understanding and support in pursing his Ph.D. degree.

TABLE OF CONTENTS

LIST OF ILLUSTRATIONS

LIST OF TABLES

1. INTRODUCTION

Global energy demand will be approximately 30% percent higher in 2040 than it was in 2010 due to both demographic and economic expansion [1]. The energy demand of countries in the Organization for Economic Cooperation and Development (OECD) will remain, essentially, flat as Gross Domestic Product (GDP) doubles. Thus, the greatest demand will come from non-OECD countries, especially China, India, and Africa. Within these countries the demand for energy will rise by nearly 60% by 2040.

At present, oil remains the world's leading fuel, accounting for 34% of global energy consumption. Oil is quite geopolitically sensitive. Any political unrest causes substantial fluctuations in oil prices. For example the turmoil in Middle Eastern countries pushed the oil price to $111.26 per barrel in 2011, an increase of 40% from the 2010 level [2]. Because the majority of oil is used for automobile applications, a transition to electrical/hybrid vehicles should be of profound societal importance. Both the Nissan Leaf® [3] and plug-in hybrid Toyota Prius® [4] are typical representatives of the advancements in electric vehicles in recent years. Nissan Leaf® features 100 miles on a single charge, powered by a 24 kWh lithium-ion battery.

Sony commercialized the Li-ion battery in 1991 and realized the portable electronic devices [5]. This type of Li-ion cell has a potential exceeding 2.6 V and gravimetric energy densities as high as 120-150 Wh/kg. The battery 500 project (proposed by IBM

and its partners) initiated research programs that consider batteries as a potential alternative for vehicle application [6]. The expected target range is 500 miles per charge. This distance would require ~ 125 kWh battery capacities with an average utilization of 250 Wh/mile. Simple calculation indicates ~1000 kg in battery weights are needed if vehicles are propelled by Li-ion cells. Battery adversely adds a huge weight on vehicles and seems impractical.

The theoretical gravimetric energy density of gasoline can reach 13000 Wh/kg; considering ~ 13% tank-to-wheel efficiency, its practical vehicle utilization is approximately 1700 Wh/kg [7]. The theoretical specific energy of current Li-ion battery (C_6Li as anode, $Li_{0.5}CoO_2$ as cathode) is 387 Wh/kg [8] and the efficiency of electric propulsion systems can reach 90% [6]. However, there is no expectation that Li-ion battery will ever come close to the performance of gasoline due to its limitation of energy density.

Lithium-air batteries have recently attracted a great deal of attentions due to their higher theoretical energy densities [6, 8-11]. Figure 1.1 presents the gravimetric energy densities for various types of rechargeable batteries. The Li-air battery holds theoretical energy densities similar to gasoline, and much higher than Li-ion batteries.

Oxidizing 1 kg of lithium metal can generate 11680 Wh of energy, not much lower than that of gasoline [6]. Generating 1700 Wh/kg will only utilizes only 14.5% of the theoretical energy of a fully charged battery. Currently, few realistic prototypes exist, making it difficult to speculate whether or not the practical efficiency can reach this value.

Bruce and co-workers anticipated if several problems can be successfully addressed, at least 2-3 times of energy capacity greater than Li-ion can be achieved. And the energy capacity would be sufficiently to deliver a driving range of more than 550 Km (~342 miles) [8]. It costs nearly 35 years of Research & Development to transform from nickel metal hydride to Li-ion batteries. Though the studies of Li-air batteries have just began, a long-term, intensive R&D should also be anticipated.

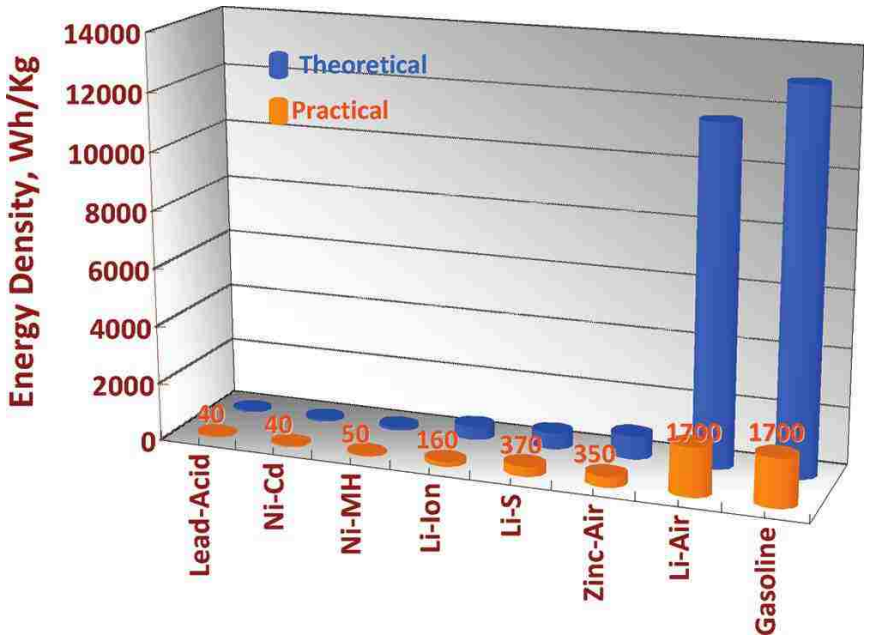

Figure 1.1. The gravimetric energy densities for various types of rechargeable batteries compared to gasoline [6].

The lithium in a Li-air battery was oxidized at the anode; oxygen was reduced at cathode. One of the advantages is that oxygen continuously comes from air instead of from a tank stored on board. Girishkumar [6] argued that the specific air flow (kg air per kW of power generated) into a Li-air battery is comparable to the specific air flow of

internal combustion engines. Currently, there are four types [6, 12] of Li-air batteries: (1) aprotic, (2) aqueous, (3) mixed aprotic/aqueous and (4) all solid-state. These batteries are illustrated in Figure 2.2 Limited reports are available on all solid-state Lithium-air batteries [13, 14]. The following introduction focuses on aprotic and aqueous batteries.

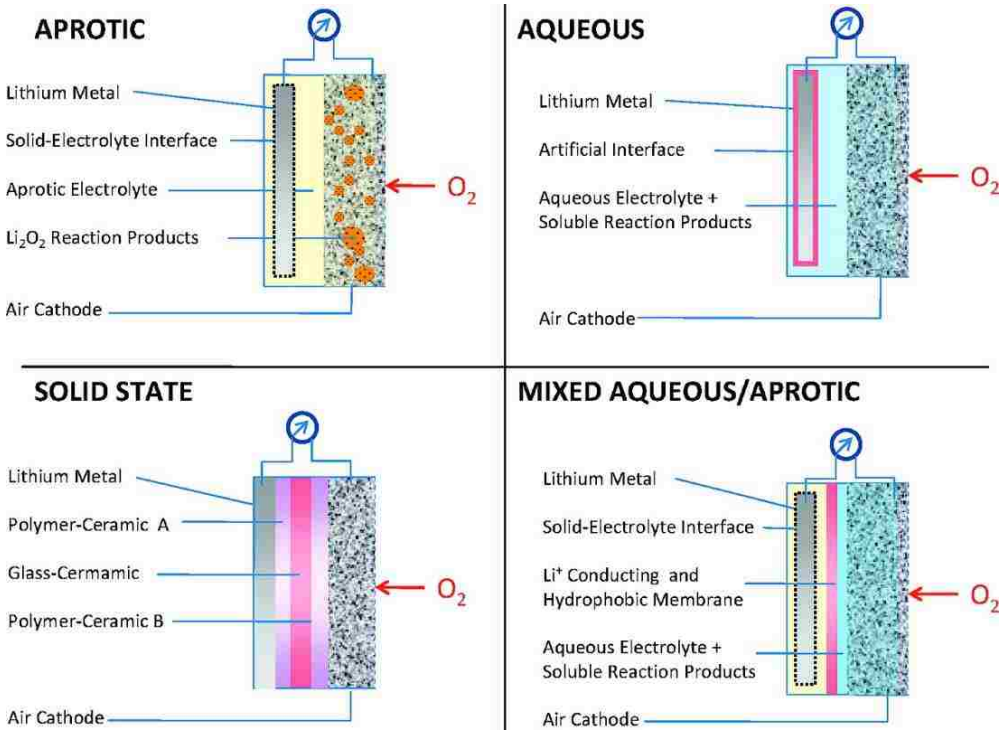

Figure 2.2. Four types architectures of Li-air batteries [6].

1.1. OVERVIEW OF LITHIUM-AIR BATTERY

1.1.1. Aprotic Li-Air Battery. The typical design of an aprotic Li-air battery is composed of a metallic lithium anode, an electrolyte with dissolved lithium salt in an aprotic solvent, and a porous O_2-breathing cathode with both carbon particles and catalyst particles [6]. Abraham and Jiang [9] first reported on rechargeable organic polymer electrolyte Li-air batteries, achieving a 250 Wh/kg specific energy. Follow-up

investigations were focused on aprotic electrolytes [15-19]. In an aprotic electrolyte, lithium metal was oxidized into lithium ions at the anode. Generated electrons flow through an external circuit and lithium ions move to and react at the cathode with oxygen to form lithium oxide [6, 8]. Generally accepted discharge reactions are as follows:

$$2Li+O_2 \rightarrow Li_2O_2$$

and possibly

$$4Li+O_2 \rightarrow 2Li_2O$$

Exact mechanisms were unknown right now, and several suggested reaction pathways were proposed. Hummelshøj *et al*. [20] suggested the following reaction steps based on density functional theory (DFT): (where "*" denotes a surface site on Li_2O_2 where the growth proceeds)

$$Li \rightarrow Li^+ + e^- \text{ (Li electrode)}$$

$$Li^+ + e^- + O_2 + {}^* \rightarrow LiO_2{}^* \text{ (O_2 cathode 1)}$$

$$Li^+ + e^- + LiO_2{}^* \rightarrow Li_2O_2 \text{ (O_2 cathode 2)}$$

Laoire *et al*. [21] considered a solvent influence on the oxygen reduction reaction to elucidate the reaction mechanism of oxygen electrode. They suggested the following possible reaction process:

$$Li^+ + e^- + O_2 \rightarrow LiO_2$$

$$2LiO_2 \rightarrow Li_2O + O_2$$

$$Li^+ + e^- + LiO_2 \rightarrow Li_2O_2$$

$$2Li + e^- + Li_2O_2 \rightarrow 2Li_2O$$

The standard potential for discharge based on Nernst equation is 2.96 V. When potentials higher than 2.96 V are applied, lithium oxide is decomposed, lithium metal is plated out on the anode, and O_2 is evolved at the cathode [6]. The discharge products, (Li_2O_2/Li_2O) are generally insoluble in the organic electrolyte. Both oxides will precipitate in pore of the porous cathode, blocking further O_2 intake [19]. Figure 3.3 illustrates a general decrease in cell capacity with an increase in discharge current. The specific capacity decreased dramatically as the discharge rate increased.

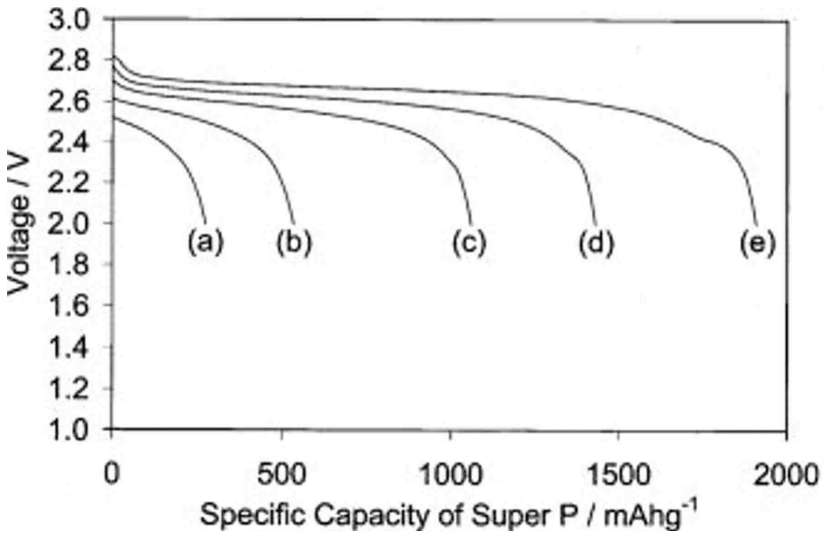

Figure 3.3. Specific capacity of Super P carbon black in polyvinylidene fluoride-hexafluoropropylene (PVDF) air cathodes [15]. (a) 1.0 mA/cm^2, (b) 0.5 mA/cm^2, (c) 0.2 mA/cm^2, (d) 0.1 mA/cm^2 and (e) 0.05 mA/cm^2.

Through scanning electron microscope (SEM) observation, Read [15] found that at lower discharge current density (*e.g.* 0.05 mA/cm^2), the size of the oxide covering the cathode was 150-200 nm. The deposit appeared to be more of a film, severely clogging the porous cathode and limiting further oxygen intake when the current density was

increased to 1.0 mA/cm^2. The cell discharge ends when the pores are almost clogged. Meanwhile, the insulator nature of Li_2O_2 contributes to both the capacity loss and the output voltage drop [22].

Lithium salts *e.g.*, $LiPF_6$, in organic carbonates: ethylene carbonate, propylene carbonate were typically used as aprotic electrolytes due to their high oxidation stabilities [23]. Reducing the solvent species with electron and lithium ion will form precipitates on the lithium electrodes [24] *e.g.*, $CH_3OCO_2CH_3+2Li^++2e^-\rightarrow(CH_2OCO_2Li)_2\downarrow+CH_2=CH_2$.

The contamination of O_2, CO_2, and trace moisture can also react with lithium metal to form Li_2O, Li_2CO_3, and LiOH respectively [23]. These scenarios will lead to the formation of multilayer surface films comprised of Li salts, a solid electrolyte interface (SEI). It would inhibit a further reaction of lithium with the solvents and prevent a further corrosion of the lithium metal. The chemically heterogeneous SEI would result in a brittle, morphologically heterogeneous structure. The accumulating defects will lead to the preferential deposition of lithium metal. The current distribution is non-uniform on the SEI, which would resualt a preferential deposition of lithium and the formation of lithium dendrite [23, 24]. The dendrite growth will impose a hazard potential, such as circuit shortening. An investigation into both linear and cyclic ether-based electrolytes revealed electrolyte degradation on the cycles [25]. Mitchell *et al.* [26] used $LiClO_4$ in dimethoxyethane as an electrolyte. They found enhanced cycling stability compared to typical carbonate based electrolyte, though fading was still present. Suitable electrolytes with high electrochemical stability, high lithium ion conductivity, high oxygen solubility,

and low viscosity still present a challenge regarding the practical application of lithium-air batteries [19]. The removal of unwanted water, carbon dioxide, and nitrogen from incoming air, while still allowing oxygen to pass, imposes a significant challenge on the cathode design [6].

$2Li+O_2 \rightarrow Li_2O_2$ can occur in a porous cathode consisting of only carbon and binder in the absence of a catalyst, yielding a 2.6 V discharging potential and a 4.8 V charging potential [18]. Débart *et al.* [18] examined the use of Pt, $La_{0.8}Sr_{0.2}MnO_3$, Fe_2O_3, NiO, Fe_3O_4, Co_3O_4, CuO and $CoFe_2O_4$ as catalysts, trying to reduce the charge potential and increase the discharge capacity. Among them, Co_3O_4 offered the best compromise between the discharge capacity and the retention on cycling. Manganese oxides, such as α-MnO_2, β-MnO_2, and γ-MnO_2 were also investigated. Among them α-MnO_2 demonstrated the best electrochemical performance [15, 27]. Providing appropriate porosity for air flow and dissolving discharge products still need to be addressed before practical applications.

1.1.2. Aqueous Li-Air Battery. Visco and colleagues [28] pioneered the aqueous version of Li-air battery, opening an alternative way to manufacture the rechargeable aqueous Li-O_2 battery. The state of the art of this type of battery is the development of Li-conducting, but electronically insulating membrane, such as LISICON-type glass (LiGC) [8]. LiGC could protect the Li metal from direct contact with aqueous solution [8]. LISICON has conductivities of 10^{-4} to 10^{-3} S cm^{-1} at ambient temperature, high resistance towards organic and aqueous electrolytes and high mechanical stability [11,

29]. The architectures of aqueous or mixed aqueous/aprotic batteries were illustrated in Figure 3.3.

Because the LiGC will react with metallic Li, an additional inert Li stable separator saturated with an aprotic electrolyte must be inserted between the lithium metal and the LiGC in mixed electrolytes batteries [19]. Mixed electrolyte batteries were intensively investigated in both acidic and alkaline/neutralized cathode electrolytes [10, 11, 30-33]. The discharge fundamental reactions were as follows:

Anode: $Li \rightarrow Li^+ + e^-$ E^o=-3.03 V *vs*. RHE

Cathode: $O_2(g) + 2H_2O + 4e^- \rightarrow 4\ OH^-$ E^o=0.40 V *vs*. RHE (alkaline media)

$O_2(g) + 4H^+ + 4e^- \rightarrow 2H_2O$ E^o=1.23 V *vs*. RHE (acidic media)

The standard discharge potentials of acid and alkaline batteries are 4.23 V and 3.43 V, respectively, higher than that of aprotic batteries. When compared to aprotic batteries, the discharge products from aqueous batteries are, to a large extent, very soluble in aqueous electrolytes; they will clog the pores. Theoretically speaking, these aqueous batteries are “anode-limited”, depending on the lithium metal in the anode [19].

Kowalczk *et al.* [19] reported discharging a Li-air battery in a 3.0 M KOH solution at 0 ^oC and a discharge current of 0.1 mA/cm^2. The battery produced a steady polarization discharge curves, even after 5 days of discharge. They suggested that the end-of-life of the Li-air cell is a result of the complete consumption of the Li anode. LiOH is generated when Li-air battery is discharged in an alkaline electrolyte, as a result leading to a rapid increase of LiOH concentration.

LiOH, however, has a limited solubility (5.3 M in water) corresponding to a specific of 200 mAh/g, barely competitive to that of Li-ion. LiOH must be allowed to precipitate from the solution to achieve a meaningful advantage over Li-ion cells. This precipitation has several negative consequences. LiOH will react with CO_2 to form Li_2CO_3 that blocks the active sites and pores of the cathode, resulting in a rapid degradation of the electrode and loss of cell capacity. Stevens *et al.* [34] introduced an anion-exchange membrane to permit generated OH^- to be transported out while blocking Li^+ entering, this membrane also blocks the ingress of CO_2 to prevent the formation of Li_2CO_3. The integration of this polymer barrier can significantly extend the life of an electrode up to 3000 hours in 7.0 M KOH, when exposed to ambient air. Stevens *et al.* [34] also found that LiOH will precipitate on the surface of LISICON membrane by forming a non-conductive coating, which results in a rapid rise of overpotential. LISICON membrane provides a nucleation site for LiOH to preferentially precipitate on the surface. The integration of an organic polymer coating can prevent LiOH precipitation, thus yielding a steady discharge curve. By combining the two improve methods, the cell cycled steady for 100 cycles at low capacities of 0.1 mAh/cm^2 and 40 cycles at high capacities of 2 mAh/cm^2.

He *et al.* [35] proposed an alternative way to protect the LISION membrane. Using a cation exchange membrane, they divided into the aqueous electrolytes into two compartments. One compartment was filled with $LiNO_3$ to facilitate the Li ion exchange. Another compartment consisted of both a LiOH solution and a recycle unit to separate

LiOH and refill with electrolytes. This novel design produces a steady galvanostatic discharge curve for one week at a discharge current density of 0.5 mA/cm^2.

Alkaline-based cells have a higher specific energy than acid-based cells [36]. Acid-based cells, however, yield a higher output voltage. And acid- based cells could dissolve Li_2CO_3 that requires special design for air cathode to remove CO_2. This type of cell has recently experienced increased attention. The LISION membrane was reported to be unstable in strong acidic and basic electrolytes; most reports were based on weak acidic environment. Zhang *et al*. [10] reported a rechargeable Li-air battery in acetic-water electrolyte. The LISION membrane was immersed in a 90 vol% HOAc solution for 3 weeks at 50 ^oC. The membrane showed no change, suggesting structural stability in this electrolyte. The cell delivered an energy density of 779 Wh/kg; it produced 15 relatively steady cycles. An increasing potential gap between discharge-charge was observed with cycling, indicating the degradation of the cell. Li *et al.* [31] introduced a dual-electrolyte with a buffer solution. The electrolyte consisted of 0.1 M H_3PO_4 and 1.0 M LiH_2PO_4. H_3PO_4 is a moderately strong acid; if used alone, it can corrode the LISION membrane. Using diluted H_3PO_4 allows for this problem to be avoided. It cannot, however, supply enough H^+ for an oxygen reduction reaction. A buffer solution, LiH_2PO_4 that stores H^+, can continuously release the necessary H^+ and keep a moderate pH value. After 20 cycles at a 0.5 mA/cm^2 discharge current density, LISION membrane displays an insignificant increase in resistance; the cell produces ~770 Wh/kg energy density. Again, an increase in the potential gap between discharge-charge was reported.

Oxidation of Li anode occurs quickly, when compared to the sluggish oxygen reduction reaction in an air cathode. A quick supply of H^+ is necessary for practical applications; neither moderate nor weak acid couldn't meet this criterion. Considering limited fuel volume suitable for electrical vehicles, high volumetric energy densities are the primary concerns. H_2SO_4 can be considered as an ideal candidate due to its wide electrochemical window, high internally stored H^+, easy dissociation ability, and good chemical stability. Kowalczk *et al.* [19] reported discharging cell at 5.25 M H_2SO_4 at 0.1 mA/cm^2 for one week with a very steady curve. Li *et al.* [33] developed an air-cathode with low Pt loading for a rechargeable Li-air battery using 1.0 M H_2SO_4 as electrolyte. After 75 hr discharge, the specific capacity and specific energy can reach 306 mAh/g and 1067 Wh/kg, respectively, higher than those of reported values taken from weak acid. Like that in weak acid, the difference between discharge and charge potential increased with the cycles, suggesting somewhat degradation.

1. 2. CATALYST DESIGN FOR ACIDIC LI-AIR BATTERY

In contrast to reduction of O_2 in aprotic electrolyte, the reduction and evolution of O_2 in acidic/alkaline media have been studied extensively for many years. The O-O bond must be split during oxygen reduction and reformed during oxygen evolution. An oxygen reduction reaction (ORR) can occur through a so-called direct four-electron pathway, in which peroxide is not formed. Formation of peroxide involves a two-electron path way

[37]. A 4-electron pathway is preferred when trying to obtain maximum redox efficiency. Pt is primarily used as ORR catalysts [38-40], even though metal free N-doped grapheme [32], manganese oxides [30] and perovskite oxides [41] were reported to exhibit fair ORR activity. Pt as the most effective ORR catalyst, however, has only moderate activity towards the oxygen evolution reaction (OER), because Pt can be easily oxidized to form oxide film and lose its catalytic activity [42]. One of major disadvantages of using single Pt as catalyst for both ORR and OER is that after several discharge-charge cycles, Pt was passivated during OER process. And partially oxidized Pt or Pt-oxide will degrade its catalytic performance. Ruthenium (Ru) metal and ruthenium oxide (RuO_2) present the most catalytically active for OER, but very unstable [43]. Efforts such as adding Pt or Ir to Ru to form alloy [44], or doping RuO_2 with Ir [43] were made trying to increase the activity and stability, however, the stability is still unacceptable for application. Iridium oxide (IrO_2) was found to be the next most catalytically active and chemically stable at high current density [43], commonly serving as an OER catalyst. Recently, Suntivich *et al.* [45] reported a perovskite oxide ($Ba_{0.5}Sr_{0.5}Co_{0.8}Fe_{0.2}O_{3-\delta}$) has intrinsic activity at least one order of magnitude higher than iridium oxide.

Catalysts with both ORR and OER activities are desired for Li-air battery to lower the charging potential and increase round-trip efficiency. Pt-Au nanoparticles were designed for an aprotic Li-air battery to achieve both the lowest charging voltage (3.5 V *vs.* Li) and the highest round-trip efficiency (~77%) possible [46]. Few studies, however, have reported on the development of bifunctional catalysts for aqueous Li-air battery.

Bifunctional catalyst, Pt/IrO_2, was commonly used in regenerative fuel cells to enhance the energy conversion efficiency during discharge/charge [47-50]. Considering the similar reaction media, this type of catalyst can be promising. Another design for aqueous Li-air cell is to use two separate and electrically isolated electrodes for individual charge and discharge. This design can avoid ORR catalysts to be polarized at the high anodic potentials required for OER [34]. However, the complexity of control systems still requires deep investigation. Jörissen [37] suggested integration of two separate catalytic layers for the air electrode, a mildly hydrophilic gas diffusion layer for OER and a highly hydrophobic gas diffusion layer for ORR.

Carbon black (CB) is widely used as a catalyst support due to its high surface area and high electronic conductivity. Pt decorated CB was commercialized and widely used as an ORR catalyst [51]. However, the corrosion of CB is severe, especially in acid media and at high potentials. Amorphous and short-range graphitic crystallites structure in CB is easily attacked by acid [52, 53]. Deposited Pt was reported to catalyze the carbon oxidation and increase its corrosion rate [52, 54]. Attentions were turned to carbon nanotubes (CNTs) as alternative supports. CNTs showed more resistance to electrochemical oxidation than CB, even though oxidation was still inevitable [52, 54, 55]. Carbon corrosion will lead to the Pt detach from support and dissolve into electrolyte, resulting in the loss of Pt electrochemical surface area (ESA) and degradation of catalyst layer [54].

TiO_2 has been found stable in an acidic/alkaline environment. TiO_2supported precious metal as catalysts were intensively investigated [44, 57-59]. However, the semiconductor nature of TiO_2 with wide band gap (E_g=3.0~3.2 eV) and low electronic conductivity (0.132 S cm^{-1} and 0.124 S cm^{-1} reported for anatase and rutile TiO_2) limits its broader applications as catalyst supports that requires a fast electron transport [60]. One reduced form of TiO_2, named as Magneli phase (Ti_nO_{2n-1}, n is an integer between 3~10), with high electronic conductivity have been commercially recognized under Ebonex® trade name [61]. Among the family of Magneli phase, Ti_4O_7 exhibits the highest electrical conductivity and high resistance to corrosion, thus receiving the most attention. There are several routes for Magneli Ti_4O_7 preparation: (1) directly reduce TiO_2 under H_2 at high temperatures (> 1273 K) [61-64]; (2) anneal TiO_2 with metallic titanium [61]; (3) anneal TiO_2 with a carbon contained reagent [65, 66]. Pt supported on Ti_4O_7 was found to exhibit a similar activity towards ORR as commercial Pt/C in fuel cell, but with significantly greater stability at high potential holding test (1.2~1.5 V) and much smaller polarization effect [65]. Metal free Ti_4O_7 was examined in a strong alkaline electrolyte, exhibiting activity for ORR and OER. Durability tests were taken in O_2 saturated 6 M KOH up to 5000 cycles at a potential range of -0.7 V~0.7 V. Only tiny surface oxidation was found and activity was insignificantly affected [63].

The synthesis of Magneli phase requires very high temperatures, resulting in severe sintering and loss of surface area [61-64]. Doping TiO_2 with Nb at relatively low temperature is an alternative route to increase TiO_2 conductivity [67]. Pt decorated Nb

doped TiO_2 was shown to have comparable ORR activity in acidic/alkaline media, and improved durability was also demonstrated [68-70]. Carbon doped TiO_2 was also reported to highly increase its conductivity, during which various titanium suboxide and titanium oxy carbide were formed [71]. Compared to Nb doping, carbon doping is a one step process that can obtain a structure well defined and controllable material. Huang *et al.* [72] reported deposition of Pt on carbon doped TiO_2 coated on CNTs (Pt/c-TiO_2/CNTs) and showed a comparable ORR activity as commercial Pt/C with much improved stability. More recently, facile mixing TiO_2 nanorods with excessive $NaBH_4$ in a solution then annealed in Ar below 400 ^oC can obtain reduced Ti_2O_3, which features as corrosion-resistant electrode materials [73].

Maximizing the utilization of active Pt surface site is always a challenge. The relatively strong OH adsorption on Pt forming PtOH will block further access of oxygen molecules to active Pt surface site [74]. Xing *et al.* [38] suggested enhancing both ORR activity and stability by adding Pt-Au alloy sublayer of Pt monolayer, and argued that the Au in the sublayer may reduce the surface oxidation. Zhang *et al.* [39] mixed Pt with another transition metal, M, where M=Ir, Ru, Re or Os. The M are expected to have a high coverage of OH at considerably lower potential than Pt, or tend to bind with O to form M-O that repulses the adsorption of OH on Pt. However, the preparations of such catalysts are sophisticated and scale-up imposes a great challenge.

Sasaki *et al.* [75] first reported that niobium oxide-supported Pt with ultra-low loading can achieve three times higher Pt mass activity for the ORR than a commercial

Pt/C. The high activity is attributed to either reduced OH or O adsorption caused by lateral repulsion of the oxide's surface. Under the oxidation conditions of 30000 cycles from 0.6 V~1.1 V, niobium oxide supported Pt exhibits a much improved stability. Zhang *et al.* [60, 76] also reported a similarly improved ORR activity and durability of Pt-niobium oxide-carbon nanotube electrodes. They argued that the insertion of a niobium oxide layer will create a transfer of electronic charge density, followed by redistribution of charge and shift of d-band center on Pt surface. One of advantages of incorporating niobium oxide when compared to the sophisticated modification of Pt monolayer is the reduced cost of niobium and relatively easier route for the synthesis.

High electrocatalytic activity and a porous structure cathode are desired for lithium air battery. Li *et al.* [33] has demonstrated air cathode prepared from carbon nanotubes, showing advantages over packed carbon black. Carbon nanotubes were intertwined in horizontal directions and form open channels for easier air diffusion. This observation opens a possible structural design of cathode structure. As previous discussed above, either TiO_2 or Nb_2O_5 exhibit corrosion resistance, and morphologies tailored to form a nanotube/nanorod structure would be considered as one solution for long-term application in acidic/alkaline lithium air battery. TiO_2 nanofilm coated CNTs have been widely reported as an easy and mature synthesis process [77-79]. Depositing desired metals onto a modified electronically conductive TiO_2 (Nb_2O_5)/CNTs hybrid composite was expected to stabilize and extend their life-time.

1. 3. STRUCTURE OF THIS THESIS

This dissertation work focused on developing high catalytically active and corrosion resistant catalyst supports for aqueous Li-air battery, and it was consisted of five papers. Paper I described Pt supported on carbon doped TiO_2 coated CNTs. The incorporation of TiO_2 nanocoating is trying to mitigate the corrosion of CNTs in acidic medium. Final results showed that carbon-doped TiO_2 nanocoating support can significantly improve both the ORR activity and the durability of the Pt electrocatalyst. Dr. Sasaki helped XANES measurements and analysis. Paper V focused on Pt supported on carbon doped Nb_2O_5 coated CNTs. Niobium oxides were expected to facilitate the ORR activity. However, the ORR activity was found to be inferior than commercial Pt/C. After 5000 potential cycles, ORR loss became obvious, even worse than Pt/C. The primary reason may come from the re-oxidation of semiconducting NbO_2 back into insulating Nb_2O_5. Dr. Li help graphics preparation. Paper II investigated titanium oxide carbide which exhibited high OER activity. Carbon doping was found to prevent the particles from sintering during high temperature annealing. Dr. Li helped graphics preparation. Paper III and Paper IV primarily focused on developing air-breathing cathode for Li-air battery. The high porous structure can facilitate the air diffusion within cathode which results the better battery performances. The bifunctional catalyst showed a significant overpotential reduction and a improved round trip efficiency. Dr. Li helped batteries assembly and testing.

PAPER

I. INCREASING Pt OXYGEN REDUCTION REACTION ACTIVITY AND DURABILITY WITH A CARBON-DOPED TiO_2 NANOCOATING CATALYST SUPPORT

Kan Huang[a], Kotaro Sasaki[b], Radoslav R. Adzic[b] and Yangchuan Xing[ac]

[a] Department of Chemical and Biological Engineering, Missouri University of Science and Technology, Rolla, Missouri 65409.
[b] Chemistry Department, Brookhaven National Laboratory, Upton, NY 11973.
[c] Department of Chemical Engineering, University of Missouri, Columbia, Missouri 65211.
E-mail: xingy@missouri.edu

ABSTRACT

We report a conductive TiO_2 nanocoating on carbon nanotubes (CNTs) as a Pt electrocatalyst support that shows a significant enhancement in Pt catalyst activity and durability for the oxygen reduction reaction. By using CNTs as a substrate for TiO_2 nanocoating, the nannoscale morphology of the oxide was retained during heat treatment. After carbon doping in the TiO_2 nanocoating, X-ray photoelectron spectroscopy suggests a shift in the binding energy of Ti 2p, implying a suboxide formation. X-ray absorption near-edge structure showed the mid-edge and post-edge up to 5010 eV, which are attributed to a 1s→4p transition and promotion of a photoelectron to higher vacant orbitals of Ti and Ti-O anti-bonding states. The observed smaller coordination number implies that a suboxide was formed with substitutional carbon. On the other hand, the

extended X-ray absorption fine structure showed that carbon also exists in interstitial positions. Electrochemical studies showed that the carbon-doped TiO_2/CNT support has a much greater electrical conductivity than that of undoped TiO_2/CNT, demonstrating that carbon doping is an effective way to achieve electrical conductivity in the oxide. Pt supported on the carbon-doped TiO_2/CNTs (Pt/c-TiO_2/CNTs) showed a better oxygen reduction activity than a commercial Pt/C catalyst. The catalyst only has a less than 3% loss in activity after electrochemical cycling 5000 times, as compared to about 55% activity loss for the Pt/C catalyst. The much better activity and durability of the TiO_2 nanocoating supported Pt was attributed to the oxygen deficient oxide support surfaces and strong metal-support interactions.

1. INTRODUCTION

Gas diffusion electrodes in fuel cells often involve carbon black as the electrode material on which a metallic electrocatalyst, such as Pt, is supported [1, 2]. Unfortunately, carbon corrosion and loss of Pt activity during electrochemical reactions make those electrochemical devices short-lived and impractical [3]. To make a stable catalyst support, recent studies have focused on metal oxides, in particular, TiO_2 [4]. However, one problem with TiO_2 is that it is not electronically conductive.

To increase conductivity of TiO_2, several methods have been proposed. Reducing TiO_2 into a Magneli phase (Ti_nO_{2n-1}) is one method of achieving conductivity in the oxide

[5-7]. It was shown that Pt supported on Magneli phase Ti_4O_7(Pt/Ti_4O_7) has comparable oxygen reduction reaction (ORR) activity as commercial Pt supported on carbon black (Pt/C) [8]. But to obtain the Magneli phase, very high temperatures (~1000 ^{o}C) have to be used to treat TiO_2. Unfortunately, the thermal process will significantly reduce the oxide's surface areas, which is needed for better catalyst dispersion. Another way to improve the conductivity of TiO_2 is to dope the oxide with a different element. For example, Nb doped TiO_2 has been studied in recent years as an electrocatalyst support [4, 9-11]. Bauer *et a*l. [4] reported doping TiO_2 with Nb and found some ORR activity in the catalysts. Hu *et al*. [12] reported carbonized TiO_2 as catalyst support in ethanol electro-oxidation. Most recently, Hahn *et al*. [13] used carbon to dope TiO_2 and found extremely high conductivity due to the formation of a Magneli-type oxide. Doping of TiO_2 also involves high temperatures (~700 ^{o}C) that increase the oxide particle sizes.

In this work, we demonstrate a nanoscale carbon doped TiO_2 coating on carbon nanotubes (c-TiO_2/CNTs) as support for Pt electrocatalyst. Several works have reported the preparation of TiO_2 and CNTs nanocomposites [14, 15]. In this work, a sol-gel process [16, 17] was used to obtain TiO_2 nanocoating on CNTs. Carbon was doped in the TiO_2 nanocoating in a gas phase process [13]. It was demonstrated that CNTs provide a good backbone for retaining the original nanoscale TiO_2 coatings (<10 nm) without sintering during heat treatment. Furthermore, we demonstrate that heat treatment is necessary to improve the activity of the supported Pt catalysts. The obtained catalysts showed almost no loss in activity in oxygen reduction reaction (ORR) after 5000 cycles.

2. EXPERIMENTAL SECTION

2.1. Synthesis of Pt/c-TiO_2/CNTs Hybrid Catalysts. CNTs with 60~150 nm in diameter and 30~100 microns in length were obtained from Pyrograf Products, Inc. All the CNTs were treated with 3:1 H_2SO_4:HNO_3 (volume ratio) in ultrasonic bath (Fisher Scientific) at 60 ^oC for 2 hours for surface functionalization, followed by filtration and thorough washing with deionized water. 10 mg treated CNTs were dispersed in a solution containing 8 mL ethanol, 2 mL benzyl alcohol plus excess water with the aid of ultrasonication and stirring. Desired amount of titanium isopropoxide was dissolved in ethanol and slowly (drop-wise) dripped into CNT suspension with a pipette. After 2 hours of stirring, the final solution was vacuum-filtered, washed in ethanol, and dried in 80 ^oC in a vacuum oven overnight. The TiO_2/CNTs hybrids were thermally treated under 10% acetylene C_2H_2 in N_2 at 500 ^oC or 700 ^oC for 20 min, designated as c-TiO_2/CNTs-500 or -700. For comparison, samples of the c-TiO_2/CNTs-700 hybrid were further annealed in N_2 at 700 ^oC for 4 hours, named as c-TiO_2/CNTs-700h. The annealing is expected to further crystallize the TiO_2 coating and enhance carbon doping. Deposition of Pt nanoparticles on the c-TiO_2/CNTs was achieved by reducing a Pt salt precursor, K_2PtCl_4, in ethylene glycol-water solution to obtain Pt/c-TiO_2/CNTs [18]. For comparison, Pt was also deposited on undoped TiO_2/CNTs (Pt/TiO_2/CNTs). Some samples of supported Pt catalysts were heat treated under 10% H_2 in N_2 for 1 hour at 500 ^oC for particle stabilization purposes, designated as, for example, Pt/TiO_2/CNTs-700h-500s. The catalysts with different treatment conditions are summarized in Table 1.

2.2. Catalyst Characterization. The morphologies of the catalysts were examined by transmission electron microscope (TEM) (Philips EM430) operating at 300 kV. The crystalline phase of the catalysts was analyzed by X-ray diffraction (XRD) equipped with Cu K (α) and the XRD data were collected with a Philips X-Pert Diffractometer over an angle range of 2θ = 10 - 90^{o} at a scanning rate of 0.026 ^{o} s^{-1}. X-ray photoelectron spectroscopy (XPS) (Kratos Axis 165) was used to analyze C1s, Ti2p, Pt4f, and O1s by employing Al K (α) excitation, operated at 150W and 15kV.

X-ray absorption spectroscopy (XAS) measurements were performed using beamline X19A at the National Synchrotron Light Source (NSLS), Brookhaven National Laboratory. The powder samples were uniformly spread on a Kepton tape for measurements in a fluorescence mode. The adsorption edge observed was Ti K at 4966 eV. Data analysis was performed using Athena and Artemis software to obtain the X-ray absorption near-edge structure (XANES) and the extended X-ray absorption fine structure (EXAFS).

2.3. Electrochemical Testing. All electrochemical experiments were performed with an Electrochemical Workstation (Bioanalytical Sciences, BAS 100) to study the carbon doped TiO_2 catalyst support. The working electrode was a glassy carbon rotating disk electrode (RDE) with a disk diameter of 5 mm (Gamry RDE 710). A Pt wire was used as the counter electrode and Ag/AgCl as a reference electrode. The catalyst powder was dispersed in deionized water by sonication for 20 min to form 1.0 mg/mL catalyst suspension. 20 μL of the suspension was pipetted onto the disk and dried in air. About 5

μL Nafion solution (0.05 wt%, Alfa Aesar) was put on top of the catalyst. Cyclic voltammetry (CV) was carried out at a scan rate of 50 mV/ s^{-1} in N_2 purged 1.0 M H_2SO_4 to evaluate the Pt electrochemical surface area (ESA), based on the hydrogen adsorption-desorption. To study catalyst durability, CV was conducted in air saturated 1.0 M H_2SO_4 in the range of 0.6~1.0 V (*vs.* RHE) up to 5000 cycles. Oxygen reduction reaction (ORR) was investigated in O_2-saturared 1.0 M H_2SO_4 before and after 5000 cycles at the rotating speed of 1600 rpm. For comparison, a commercial Pt/C catalyst (20 wt%, from E-TEK) was also tested under the same conditions.

3. RESULTS AND DISCUSSION

3.1. Characterization of The Pt/c-TiO_2/CNTs Catalysts. Fig. 1 shows typical TEM images of the Pt nanoparticles supported on c-TiO_2/CNTs. The thin TiO_2 coating was found to be well maintained during carbon doping and Pt deposition processes; the coating thickness was measured to be 8~10 nm. From the images it can be seen that aggregation of Pt nanoparticles is minimal and they are highly dispersed on the TiO_2/CNTs support. EDX analysis shows the presence of Ti element in a TiO_2/CNTs sample (see Fig. S1).

The average particle sizes are estimated based on TEM image processing from over 100 randomly picked particles. Fig. 1(a) and (b) show TEM images of Pt/c-TiO_2/CNTs-500 and Pt/c-TiO_2/CNTs-700 with particle sizes of 2.24±0.43 nm and

2.19±0.41 nm, respectively. After thermal treatment at 500 ^{o}C under H_2-N_2 atmosphere, the Pt nanoparticles grow bigger with sizes of 3.31±0.74 nm in Fig. 1(c) and 3.41±1.08 nm in Fig. 1(d). Particle size distribution has also become broader due to sintering under thermal treatment. However, no obvious particle aggregation was found, which may be due to the fact that TiO_2 interacts more strongly with Pt *via* metal-oxide bond [19] than carbon via the Van de Waals force. The last sample in Fig. 1(d) with heat treatment of c-TiO_2/CNTs before Pt deposition shows even bigger spread, possibly indicative of different states of the TiO_2 surface, but it has better electrochemical activity as discussed below.

A typical XRD pattern for the Pt catalysts on support (Pt/c-TiO_2/CNTs-700) is shown in Fig. 2. All the prepared samples have similar patterns. Pt nanoparticles are crystalline, as indicated by the characteristic peaks of Pt [18]. Relatively small deflection peaks of c-TiO_2 were detected due to the thin coating, similar to the results reported by Song *et al*. [20] Compared to pure TiO_2 particles (Degussa, P25), new peaks between 43 and 45^{o} were found in doped TiO_2/CNTs. Hahn *et al*. [13] reported that doping TiO_2 nanotubes at 850 ^{o}C can form titanium oxycarbide and various suboxides, and the most obvious differences between doped TiO_2 nanotubes and pure TiO_2 nanotubes are the emergence of new peaks at $2\theta \approx 42.5^{o}$, 61.5^{o}. As a result, we attribute the new peaks to the formation of suboxides. In a separate experiment, we found that doping crystallized TiO_2 particles (Degussa, P25) under the same condition for 20 min produced no C peaks, indicative of that the carbon is in amorphous phase. Similar results were also found in the

works of Hahn *et al*. [13, 21]. Consequently, we believe the C peak observed in the XRD patterns are only attributed to the graphitic structures of the CNTs.

The chemical states of O, Ti, C and Pt were investigated by XPS [22], and the results were shown in Fig. 3. Pure TiO_2 (Degussa, P25) was chosen for comparison. In Fig. 3(a) Ti peaks of $2p_{1/2}$ and $2p_{3/2}$ in c-TiO_2/CNTs were found at binding energies (BEs) of 465.1 eV and 459.4 eV, respectively. According to Li *et al*. [23], pure TiO_2 displays BEs at 464.2 eV and 458.5eV, while the reduced form, Magneli phase Ti_4O_7, has BEs at 464.7 eV and 459.0 eV. Göpel *et al*. [24] suggested that the shift of Ti 2p from defect-free TiO_2 is caused by surface oxygen vacancy defect. Carbon can be incorporated into TiO_2 lattice or substituted for oxygen, which can have synergistic effect with oxygen vacancies [25], resulting in the change of electron structure between conducting band and valence band.

Thus, the Ti 2p shifts towards higher BEs may be attributed to the partially reduced Ti and combined effects between carbon and oxygen vacancies [24]. Therefore, the Ti2p BE in our catalysts has BEs shifted towards the reduced phase, suggesting that a reduced oxide layer was formed from carbon doping. The O1s found at 530.6 eV in c-TiO_2/CNTs also suffered a shift compared pure TiO_2, which was observed in Hahn's work [13]. Carbon doped TiO_2 is often written as $TiO_{2-x}C_x$, which has oxygen vancancies and sub-stoichiometric titanium oxide (TiO_{2-x}) responsible for the increase the conductivity in the oxides [6, 26].

We noted that C1s shows two peaks at 285.6 eV and 284.5 eV in Fig. 3(c); they should correspond to a carbonate species [27] and the graphite phase [28]. It is also noted that no C1s peak was found near 281.5 eV that belongs to TiC [28], indicative of that no single TiC phase was formed. The graphite phase would come from the CNTs; the carbonate species peak may be due to interstitial carbon, as confirmed by the results from EXAFS discussed below. The BE peaks of Pt 4f at 74.9 eV and 71.6 eV in Fig. 3(b) revealed oxide-free Pt metallic nanoparticles [29]. It is also observed that Pt deposition on the Ti oxide nanocoating does not cause shifts in BEs (see Fig. S2 in the ESI).

3.2. X-ray Absorption of The Pt/c-TiO_2/CNTs Catalysts. Fig. 4 shows XANES spectra of Ti K edge from Pt/TiO_2/CNTs (red curve) and Pt/c-TiO_2/CNTs-700h-500s (blue curve). Both spectra have three small pre-edge peaks designated as A1, A2, and A3; the details are illustrated in the insert of Fig. 4. Several works have rationalized these pre-edge features as arising from mixing of the *p* orbital of absorbing Ti atom with the *d* orbital of the neighboring Ti atoms [30-33]. Prominent differences in the pre-edges between undoped TiO_2 and C-doped TiO_2 are observed for the position and height of the A2 peaks. The A2 peak from the undoped TiO_2 shows a higher peak at a lower energy position compared with that from the C-doped TiO_2. The intensity of the pre-edge peak is sensitive to the symmetry of the surrounding atoms, and therefore they are weak in symmetrical environments and increase in intensity as the environment is distorted [34]. Luca *et al*. [31, 34, 35] demonstrated that the A2 peak intensity increased and the peak position lowered as particle size decreased (from 60 nm to 2 nm), and amorphous TiO_2

particles showed the higher intensity at a lower position than any of those crystalline TiO_2 nanoparticles. The structure of the undoped TiO_2 at the present study is thus amorphous (or assembly of short-range order nano-crystallites), consistent with the fact that the oxide was not thermally treated. The undoped TiO_2 shows no mid-edge peak and two broad post-edge peaks up to 5010 eV, which further support the evidence of amorphous structure [35]. The spectrum from the C-doped TiO_2 shows the mid-edge (B) and the post-edges (C1, C2, C3) up to 5010 eV, which are attributed to a 1s→4p transition and promotion of a photoelectron to higher vacant np orbitals of Ti and Ti-O anti-bonding states in the coordination environment of Ti [31, 36]. The white line feature observed for the C-doped TiO_2 is very similar to that from rutile (it should be noted that anatase displays first a highest white line peak, followed by four small peaks up to 5010 eV, ref. 33-36), consistent with the results from XRD patterns.

Fig. 5 depicts the Fourier transformed EXAFS spectra of Ti K edge k^2-weighted data from Pt/TiO_2/CNTs (Fig. 5(a)) and Pt/c-TiO_2/CNTs (Fig. 5(b)). Also shown are fitted lines (blue dotted lines) based on Ti-Ti and Ti-O paths for pure rutile TiO_2. It should be noted that owing to similar nature between oxygen and carbon, it was difficult to fit the data to distinguish Ti-O and Ti-C paths. Fitting was performed within a *r*-range of 1–2.8 $Å^{-1}$, corresponding to a first shell of Ti nearest-neighbor linkages (Ti-O1 and Ti-Ti1 pairs). We adapted a similar fitting procedure reported in ref. 35 and 37. Good agreement between the original spectra and the fits is seen. The results of coordination numbers ($N_{Ti\text{-}Ti}$ and $N_{Ti\text{-}O}$) and bond lengths ($R_{Ti\text{-}Ti}$ and $R_{Ti\text{-}O}$) are summarized in Table 2, together

with those from anatase and rutileTiO_2. The bond length of Ti-O is shorter and that of Ti-Ti is longer for the undoped TiO_2 compared with those of rutile and anatase phases; these differences could be caused by the local structure distortion; similar phenomena have been observed in amorphous and nanoparticle TiO_2 [35, 38]. The undoped TiO_2 have transformed to rutile-like structure by annealing during carbon doping, as mentioned above. The transformation for nano-crystalline TiO_2 to a rutile structure during heating has also been reported by Zhang and Banfield [35, 39, 40]. The bond length of Ti-O ($R_{Ti\text{-}O}$ at 1.96 Å) for the C-doped TiO_2 is close to that for rutile (see Table 1), while the coordination number of TiO ($N_{Ti\text{-}O}$) is somewhat smaller (5.7 *vs.* 6). The smaller coordination number may indicate that some TiO_2 is reduced to a suboxide during carbon doping as observed from the above XPS study and oxygen vacancy is left. However, a marked feature observed here is that the bond length of Ti-Ti (3.16 Å) becomes much longer than that of rutile (2.96 Å), even though the local distortion should have been released through crystallization during the annealing process. This suggests that carbon may have also been incorporated interstitially in TiO_2 lattice and therefore expanded the Ti-Ti bonds. This notion is in line with other investigations for carbon-doped TiO_2 for use as photocatalysts that demonstrated the presence of carbon atoms at interstitial positions [41-43].

3.3. Electrochemical Activity of The Catalysts. Fig. 6 shows comparison of the electrochemical activity of Pt/TiO_2/CNTs with that of Pt/c-TiO_2/CNTs. It clearly

demonstrated that Pt nanoparticles supported on c-TiO_2/CNT exhibit much higher electrochemical activity, and Pt on TiO_2/CNTs shows negligible catalytic activity due to the low conductivity of undoped TiO_2 as support. *In situ* XANES spectra of Pt L3 edge from Pt/TiO_2/CNTs show the very slow reduction of Pt oxides on TiO_2 (Fig. S3 in ESI); this is presumably due to the poor conductivity of the support. Such a long delay in reduction was not observed for the conductive supports, such as Pt/c-TiO_2/CNTs. These results demonstrate that carbon doping indeed significantly increased the electronic conductivity in TiO_2. We believe in our case that the combined effects of substitutional carbon, interstitial carbon and oxygen vacancy contributed to the change in electronic band structure of TiO_2 [25], resulting in the increase of its conductivity. The close contact of Pt with its conducting support enables the catalyst to have typical Pt electrochemical activity in the CV, as displayed in the regions of hydrogen adsorption/desorption, platinum oxidation, and platinum-oxide reduction [4].

Fig. 7 shows the CV results of initial cycling and that after 1000 cycles for two catalysts with TiO_2 C-doped at two different temperatures, *i.e.*, 500 ^{o}C and 700 ^{o}C. Table 3 lists the electrochemical surface areas (ESA) of the supported catalysts obtained at initial cycling and after 1000 cycles. The ESA was obtained by integrating the area of hydrogen adsorption region (~ 0.05 - 0.3 V) [44]. Comparing the catalysts C-doped at 500 ^{o}C and 700 ^{o}C, the ESA loss of the latter is much smaller, indicative of doping temperature effect. At the lower temperature, doping is mostly a surface deposition process rather than bulk doping [21] and free carbon are formed on the TiO_2 surface;

consequently, those amorphous carbon with short-range of crystallites were easily attacked by acid and therefore affected the durability of the Pt supported on it [3].

The measurements of ORR for three Pt/c-TiO_2/CNTs catalysts and a Pt/C E-TEK catalyst are illustrated in Fig. 8. The measured electrochemical surface areas (ESA) of Pt/c-TiO_2/CNTs-700-500s, Pt/c-TiO_2/CNTs-700h-500s and Pt/C were around 1000~1100 cm^2 mg_{Pt}^{-1}, which makes them suitable for comparing their catalytic activities. The half-wave potentials for Pt/c-TiO_2/CNTs-700, Pt/c-TiO_2/CNTs-700-500s, Pt/c-TiO_2/CNTs-700h-500s and Pt/C are 0.719 V, 0.728 V, 0.746 V and 0.766 V, respectively. The better performance of Pt/C are mainly due to the higher total Pt surface area as a result of its higher Pt loading (20 wt% *vs.* 10 wt% for the Pt/c-TiO_2/CNTs catalysts). It may be also the results from the higher conductivity of pure carbon support. Among the three oxide supported catalysts, Pt/c-TiO_2/CNTs-700h-500s yielded the best ORR activity. This catalyst was heat treated twice, one for the oxide and one for the Pt. It is obvious that with the aid of post-thermal treatments, the performance can be much improved.

The thermal treatment can improve the crystallinity of TiO_2 and further increase the reaction between free carbon and TiO_2 to form $TiO_{2-x}C_x$, increasing the electronic transport within the support (green curves *vs.* blue curve). In addition, thermal treatment to the supported Pt increased its sizes and enhanced the synergistic interaction between oxide support and Pt nanoparticles (blue curve *vs.* red curve). Tafel plots derived from the kinetic currents, j_k, of the catalysts using Koutecky-Levich theory [45] are shown in Fig.

9(a); all Tafel curves are normalized to the individual ESA of the Pt catalysts. In the range of kinetically controlled region (~0.67-0.85 V), the kinetic current densities of Pt/c-TiO_2/CNTs-700h-500s are higher than those of Pt/C. The Pt mass based kinetic currents are displayed in Fig. 9(b), which further demonstrated the better performance of the double heat-treated catalyst.

To gain understanding on the durability of the catalysts under potential cycling conditions, we cycled the catalysts 5000 times in the range of 0.6 ~ 1.0 V (RHE) in air-saturated 1.0 M H_2SO_4. Comparison of the ORR activity before and after the cycling was made. The insets in Fig. 10 show the CVs of the catalysts before and after cycling. After 5000 cycles, the ESA losses were 15% for Pt/c-TiO_2/CNTs-700-500s and Pt/c-TiO_2/CNTs-700h-500s, 28% for Pt/c-TiO_2/CNTs-700, and 30% for Pt/C. A marked improvement in ESA loss was found for the Pt catalysts with heat treatment. As described above, the heat treatment increased the Pt particle sizes and made the catalyst more stable. In the meantime, it also enhanced the attachment of the Pt nanoparticles to the oxide support. Both effects would lead to more durable catalysts.

Figure 10 shows the polarization curves of ORR of the catalysts before and after cycling. As can be seen the half-wave potentials of Pt supported on c-TiO_2/CNTs do not suffer much loss after cycling. Especially, the loss in ORR activity of Pt/c-TiO_2/CNTs-700h-500s is only is 2.7% at 0.75 V and 1.7% at 0.8 V (see Figure 10(e)). In comparison, the loss of ORR activity for the Pt/C catalyst is 53% at 0.75 V and 56% at 0.8 V. Considering that the ESA loss for Pt/C is only twice that of

Pt/c-TiO_2/CNTs-700h-500s, there must be an increase in the activity of ORR for the carbon doped TiO_2 nanocoating supported Pt.

Surface defects in TiO_2 (110), especially oxygen vacancies, have been considered as active sites for water splitting; they form donor level in the upper part of the energy band gap [46, 47]. Göpel *et al*. [24] also reported that surface oxygen vacancies can interact with chemisorbed O_2 and H_2. It is speculated that the improved ORR activity is associated with the oxygen vacancies in the TiO_2 nanocoating. The interactions of water with the catalyst during surface oxidation may have occurred first with the oxygen deficient support before it can form Pt-OH, which is considered as a barrier for ORR. In addition, the metal-support interactions would be much stronger for Pt on oxide than on carbon, which help stabilize the Pt catalyst. A further investigation is needed to elucidate the mechanism of the observed enhanced activity and durability.

4. CONCLUSIONS

Here we report a study of carbon doped TiO_2 nanocoating as a support for the Pt electrocatalyst for ORR. The TiO_2 were coated on CNTs in a sol-gel process, leading to nanoscale thin TiO_2 coating on CNTs. Doping the TiO_2 nanocoating with carbon was successfully achieved by a gas phase process. Carbon doping transformed the wide band-gap semiconductor oxide into a highly conductive material. The high electrical conductivity of carbon doped TiO_2 was attributed to a suboixde formation with

substitutional and interstitial carbon, as revealed by XPS and XANES studies. Pt supported on the carbon doped TiO_2 nanocoating support showed high activity when compared to that of Pt on semiconducting TiO_2. Rotating disk electrode measurements showed a high ORR activity on the oxide supported Pt. The results indicated that post-thermal treatment can significantly improve the catalyst activity and stability. Under oxidizing conditions of 5000 potential cycles from 0.6 V~1.0 V, Pt on c-TiO_2/CNTs suffered almost no loss in ORR activity loss as compared with more than 50 % loss in commercial Pt/C catalyst at 0.75 V. This work demonstrated that carbon-doped TiO_2 nanocoating support can significantly improve both the activity and the durability of the Pt electrocatalyst.

5. ACKNOWLEDGMENTS

This work is partially supported by the Department of Energy ARPA-E BEEST program (DE-AR 000066). We thank Dr. Eric Bohannan for the XRD analysis, Mr. Brian Porter for the XPS analysis and Dr. Dan Zhou at Nanoscience Center at University of Missouri in St Louis for taking the TEM images. We also thank Prof. Anatoly Frenkel and Dr. Nebojsa Marinkovic for great help in the EXAFS analysis.

REFERENCES

[1] A. Débart, J. Bao, G. Armstrong and P. G. Bruce, J. Power Sources, 2007, 174, 1177-1182.

[2] T. Ogasawara, A. Débart, M. Holzapfel, P. Novák and P. G. Bruce, J. Am. Chem. Soc., 2006, 2006, 128, 1390-1393.

[3] S. K. Natarajan and J. Hamelin, J. Electrochem. Soc., 2009, 156, B210-B215.

[4] A. Bauer, K. Lee, C. Song, Y. Xie, J. Zhang and R. Hui, J. Power Sources, 2010, 195, 3105-3110.

[5] J. R. Smith, F. C. Walsh and R. L. Clarke, J. Appl. Electrochem., 1998, 28, 1021-1033.

[6] W.-Q. Han and Y. Zhang, Appl. Phys. Lett., 2008, 92, 203117-203113.

[7] F. C. Walsh and R. G. A. Wills, Electrochim. Acta, 2010, 55, 6342-6351.

[8] T. Ioroi, H. Senoh, S.-i. Yamazaki, Z. Siroma, N. Fujiwara and K. Yasuda, J. Electrochem. Soc., 2008, 155, B321-B326.

[9] M. D. Koninck, P. Manseau and B. Marsan, J. Electroanal. Chem., 2007, 611, 67-79.

[10] K.-W. Park and K.-S. Seol, Electrochem.Commun., 2007, 9, 2256-2260.

[11] N. R. Elezovic, B. M. Babic, L. Gajic-Krstajic, V. Radmilovic, N. V. Krstajic and L. J. Vracar, J. Power Sources, 2010, 195, 3961-3968.

[12] F. Hu, F. Ding, S. Song and P. K. Shen, J. Power Sources, 2006, 163, 415-419.

[13] R. Hahn, F. Schmidt-Stein, J. Salonen, S. Thiemann, Y. Song, J. Kunze, V.-P. Lehto and P. Schmuki, Angew. Chem. Int. Ed., 2009, 48, 7236-7239.

[14] J. Yu, J. Fan and B. Cheng, J. Power Sources, 2011, 196, 7891-7898.

[15] J. Yu, T. Ma and S. Liu, Phys.Chem. Chem.Phys., 2011, 13, 3491-3501.

[16] D. Eder and A. H. Windle, J. Mater. Chem., 2008, 18, 2036-2043.

[17] D. Eder and A. H. Windle, Adv. Mater., 2008, 20, 1787-1793.

[18] Y. Xing, J. Phys.l Chem. B, 2004, 108, 19255-19259.

[19] Y. Zhang and H. Dai, Appl. Phys. Lett., 2000, 77, 3015-3017.

[20] H. Song, X. Qiu, F. Li, W. Zhu and L. Chen, Electrochem. Commun., 2007, 9, 1416-1421.

[21] R. Hahn, A. Ghicov, J. Salonen, V.-P. Lehto and P. Schmuki, Nanotechnology, 2007, 18, 105604.

[22] J. Yu, G. Dai, Q. Xiang and M. Jaroniec, J. Mater. Chem., 2011, 21, 1049-1057.

[23] X. Li, A. L. Zhu, W. Qu, H. Wang, R. Hui, L. Zhang and J. Zhang, Electrochim. Acta, 2010, 55, 5891-5898.

[24] W. Göpel, G. Rocker and R. Feierabend, Phys. Rev. B, 1983, 28, 3427-3438.

[25] C. Di Valentin, G. Pacchioni and A. Selloni, Chem. Mater., 2005, 17, 6656-6665.

[26] J. H. Park, S. Kim and A. J. Bard, Nano Lett., 2005, 6, 24-28.

[27] E. A. Reyes-Garcia, Y. Sun, K. R. Reyes-Gil and D. Raftery, Solid State Nucl. Magn. Reson., 2009, 35, 74-81.

[28] Y. Luo, S. Ge, Z. Jin and J. Fisher, Appl. Phys. A: Mater. Sci. Process., 2010, 98, 765-768.

[29] R. Li, W. Chen, H. Kobayashi and C. Ma, Green Chemistry, 2010, 12, 212-215.

[30] T. Uozumi, K. Okada, A. Kotani, O. Durmeyer, J. P. Kappler, E. Beaurepaire and J. C. Parlebas, Europhys. Lett., 1992, 18, 85.

[31] Z. Y. Wu, G. Ouvrard, P. Gressier and C. R. Natoli, Phys. Rev. B: Condens. Matter, 1997, 55, 10382-10391.

[32] K. Okada and A. Kotani, J. Electron Spectrosc. Relat. Phenom., 1993, 62, 131-140.

[33] Y. V. Zubavichus, Y. L. Slovokhotov, M. K. Nazeeruddin, S. M. Zakeeruddin, M.

Grätzel and V. Shklover, Chem. Mater., 2002, 14, 3556-3563.

[34] V. Luca, S. Djajanti and R. F. Howe, J. Phys. Chem. B, 1998, 1998, 102, 10650-10657.

[35] H. Zhang, B. Chen, J. F. Banfield and G. A. Waychunas, Phys. Rev. B:Condens. Matter Mater. Phys., 2008, 78, 214106.

[36] K. E. Lee, M. A. Gomez, T. Regier, Y. Hu and G. P. Demopoulos, J. Phys. Chem. C, 2011, 115, 5692-5707.

[37] W. Li, A. I. Frenkel, J. C. Woicik, C. Ni and S. I. Shah, Phys. Rev. B: Condes. Matter Mater. Phys., 2005, 72, 155315.

[38] V. Schwartz, D. R. Mullins, W. Yan, H. Zhu, S. Dai and S. H. Overbury, J. Phys. Chem. C, 2007, 111, 17322-17332.

[39] H. Zhang and J. F. Banfield, J. Phys. Chem. B, 2000, 104, 3481-3487.

[40] H. Zhang and J. F. Banfield, J. Phys. Chem. C, 2007, 111, 6621-6629.

[41] H. Li, D. Wang, H. Fan, P. Wang, T. Jiang and T. Xie, J. Colloid and Interface Sci., 2011, 354, 175-180.

[42] K. Gutbrod, P. Greil and C. Zollfrank, Appl. Catal. B, 2011, 103, 240-245.

[43] Y. Wu, M. Xing, J. Zhang and F. Chen, Appl. Catal. B, 2010, 97, 182-189.

[44] L. Li and Y. Xing, J. Phys. Chem. C, 2007, 111, 2803-2808.

[45] L. R. F. Allen J. Bard, Electrochemical Methods: Fundamentals and Applications., John Wiley & Sons, New York, 2001.

[46] R. Schaub, P. Thostrup, N. Lopez, E. Lægsgaard, I. Stensgaard, J. K. Nørskov and F. Besenbacher, Phys. Rev. Lett., 2001, 87, 266104.

[47] J. Nowotny, T. Bak, M. K. Nowotny and L. R. Sheppard, J. Phys. Chem. B, 2006, 110, 18492-18495.

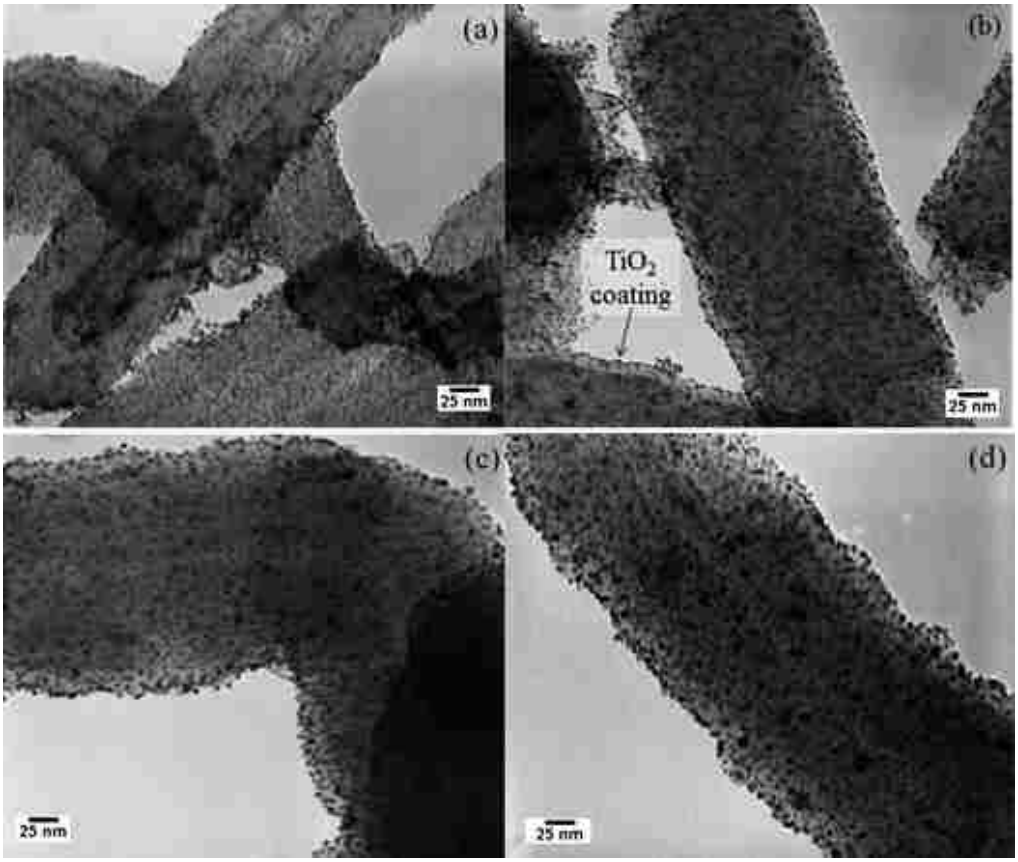

Fig. 1 TEM images of 10wt% Pt nanoparticles on c-TiO_2/CNTs. (a) Pt/c-TiO_2/CNTs-500; (b) Pt/c-TiO_2/CNTs-700; (c)Pt/c-TiO_2/CNTs-700-500s; (d) Pt/c-TiO_2/CNTs-700h-500s.

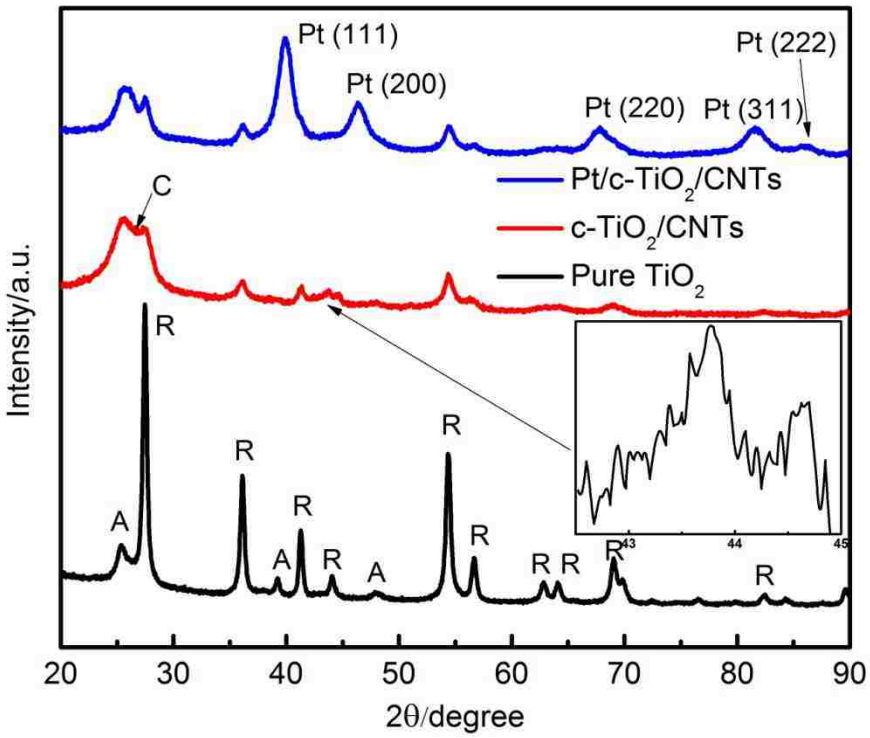

Fig. 2 XRD pattern of Pt/c-TiO_2/CNTs, c-TiO_2/CNTs and pure TiO_2 (annealed under 700 o C for 1 hour). The inset shows the emergence of new diffraction between 43 and 45 degrees of 2θ. The peaks labeled A and R are anatase and rutile phases.

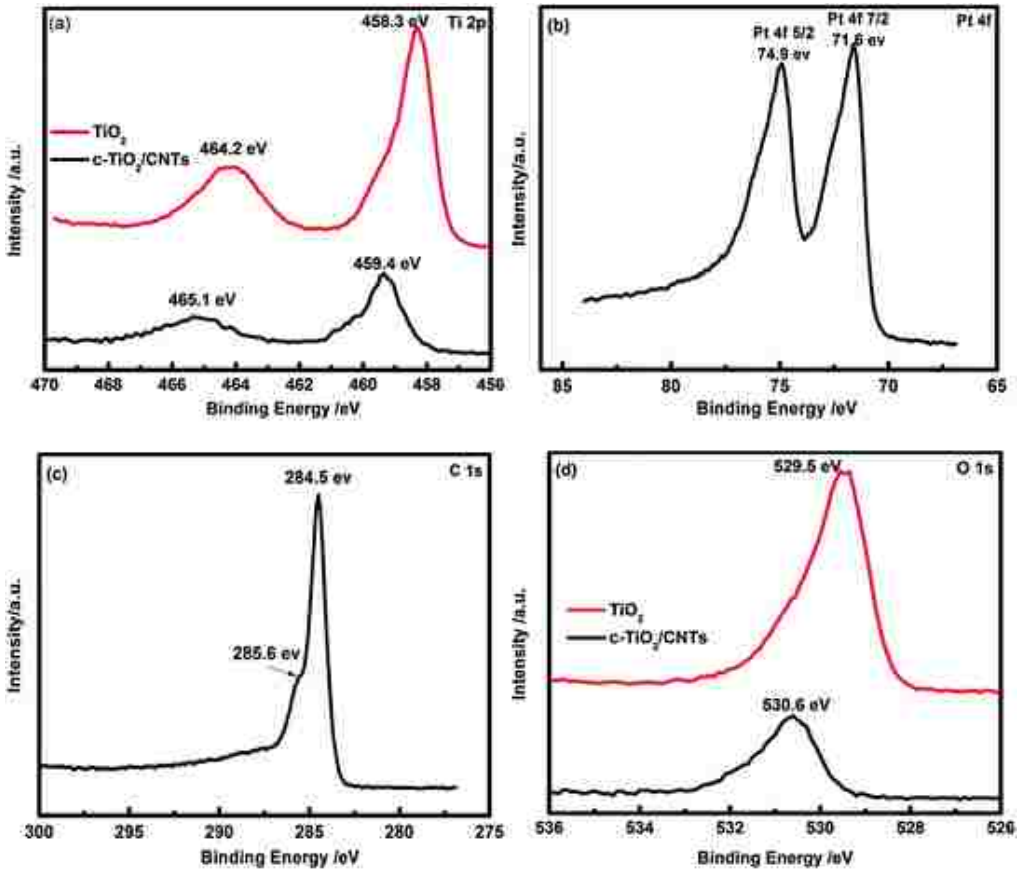

Fig. 3 XPS results of Ti 2p, O 1s, C 1s, and Pt 4f from the Pt/c-TiO_2/CNTs catalyst and pure TiO_2.

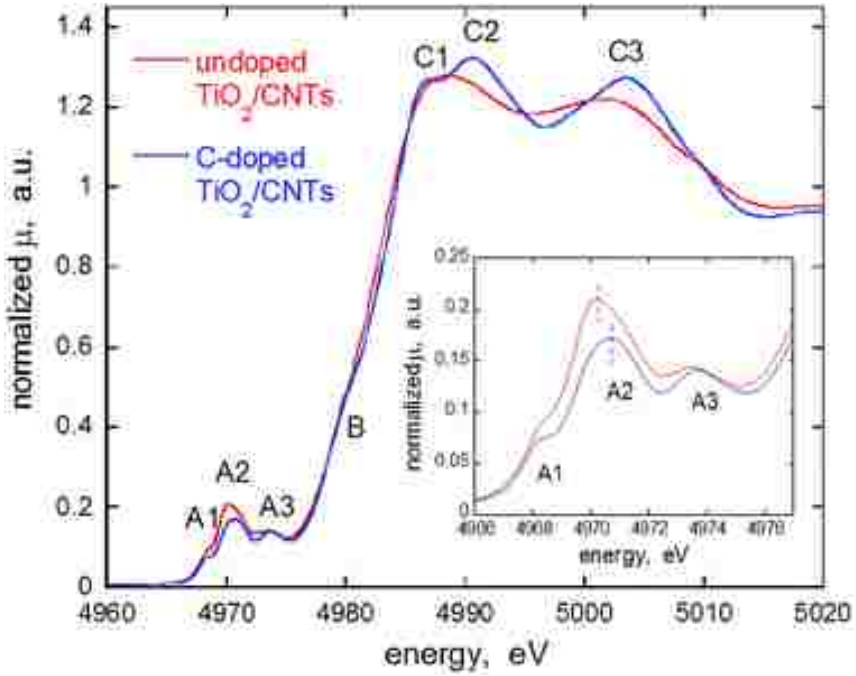

Fig. 4 XANEs spectra of Ti K edge from Pt/TiO_2/CNTs (red curve) and Pt/c-TiO_2/CNTs (blue curve). A1, A2 and A3: pre-edge peaks, B: mid-edge peak, C1, C2 and C3: post-edge peaks.

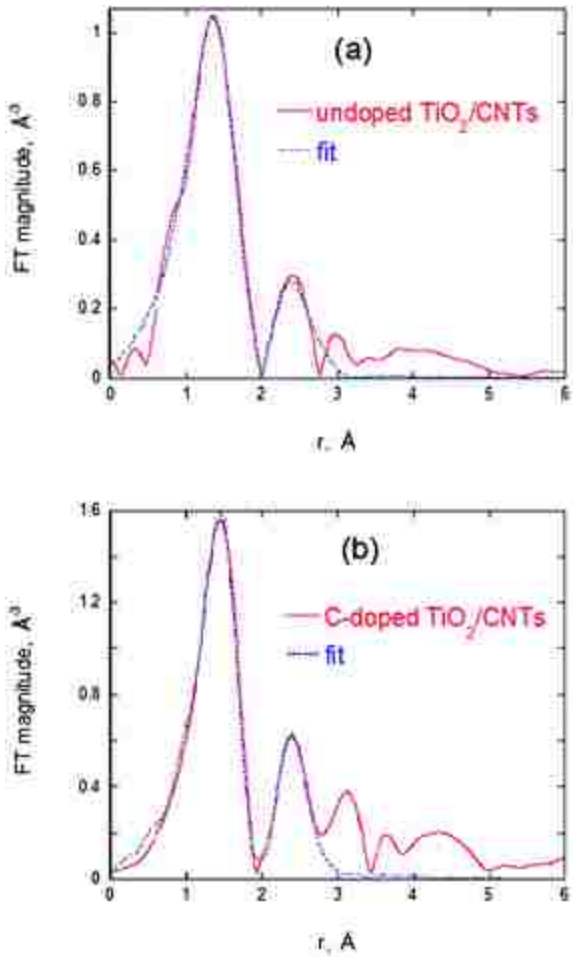

Fig. 5 Fourier transformed magnitudes of Ti K edge k2-weighted data from (a) $Pt/TiO_2/CNT$ and (b) $Pt/c\text{-}TiO_2/CNT$ together with the respective first shell fits.

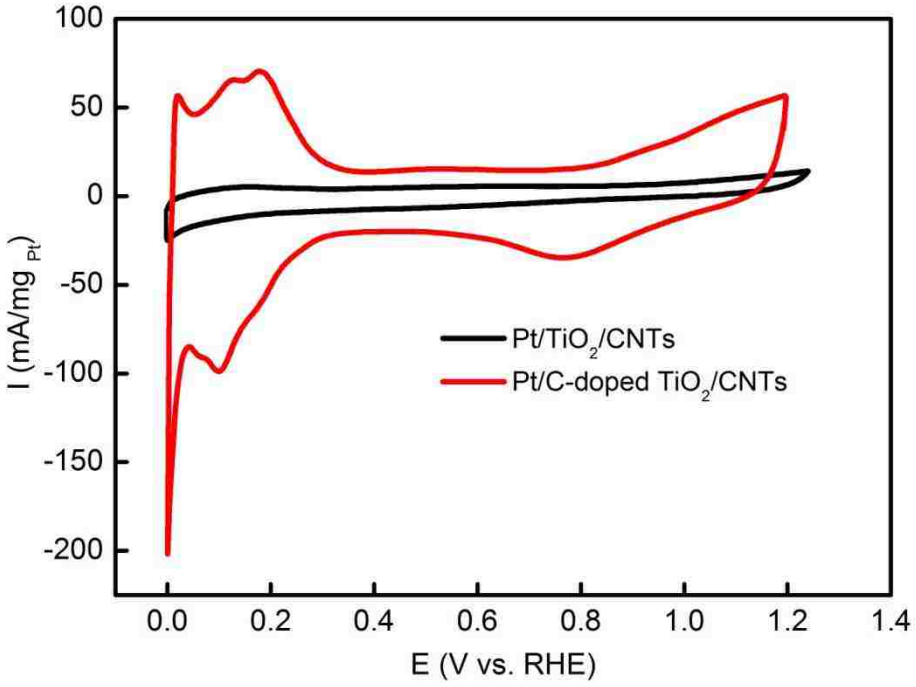

Fig. 6 Cyclic voltammetry comparison between Pt/c-TiO_2/CNTs with Pt/TiO_2/CNTs, showing that carbon doping improved the conductivity of the support oxide. Electrolyte: N_2 purged 1.0 M H_2SO_4; scan rate: 50 mV s^{-1}.

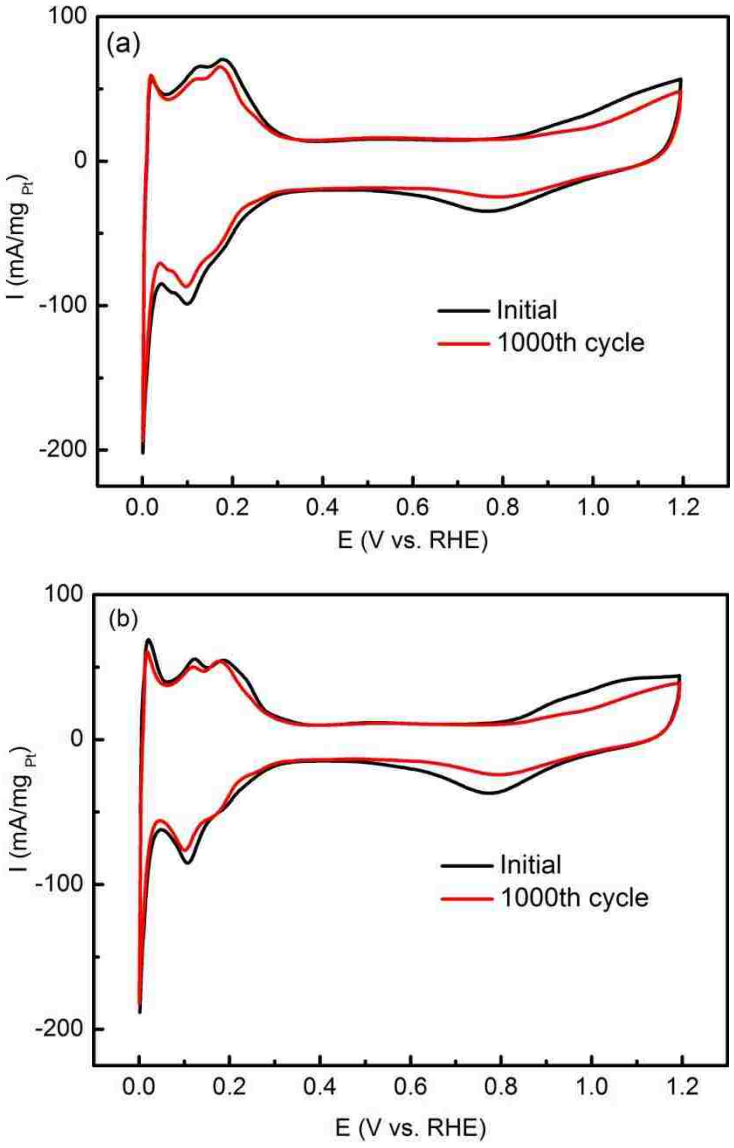

Fig. 7 CV of initial cycle and that after 1000 cycles, showing reduced loss when the doping temperature is high. (a) Pt/c-TiO_2/CNTs-500; (b) Pt/c-TiO_2/CNTs-700. Electrolyte: air-saturated 1.0 M H_2SO_4, scan rate: 50 mV s^{-1}.

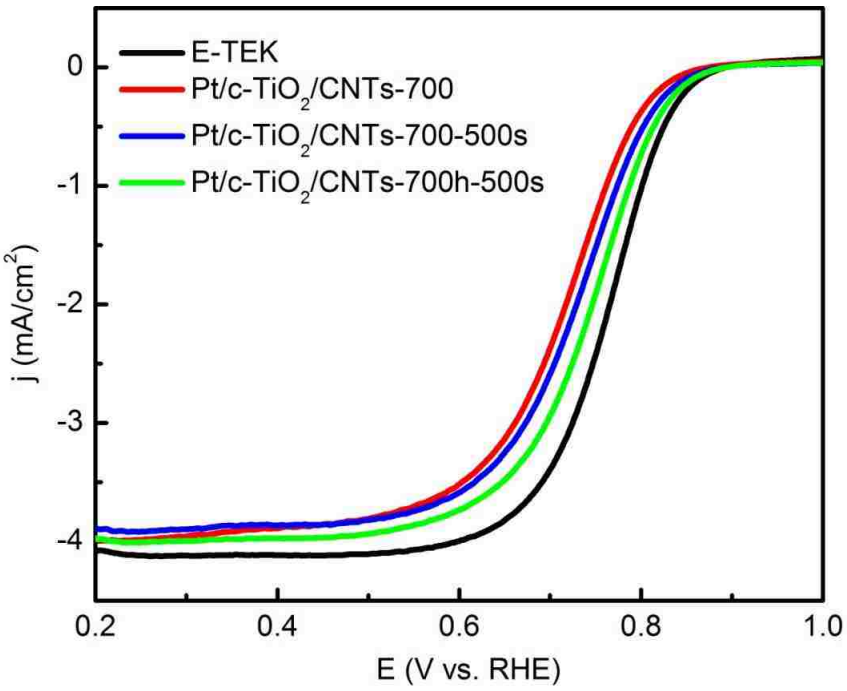

Fig. 8 Polarization curves for the ORR on different catalysts. The Pt loading on the oxides is 10 wt%, while that of the E-TEK is 20 wt%. Electrolyte: O_2 saturated 1.0 M H_2SO_4, Rotating speed: 1600 rpm, scan rate: 10 mV s^{-1}.

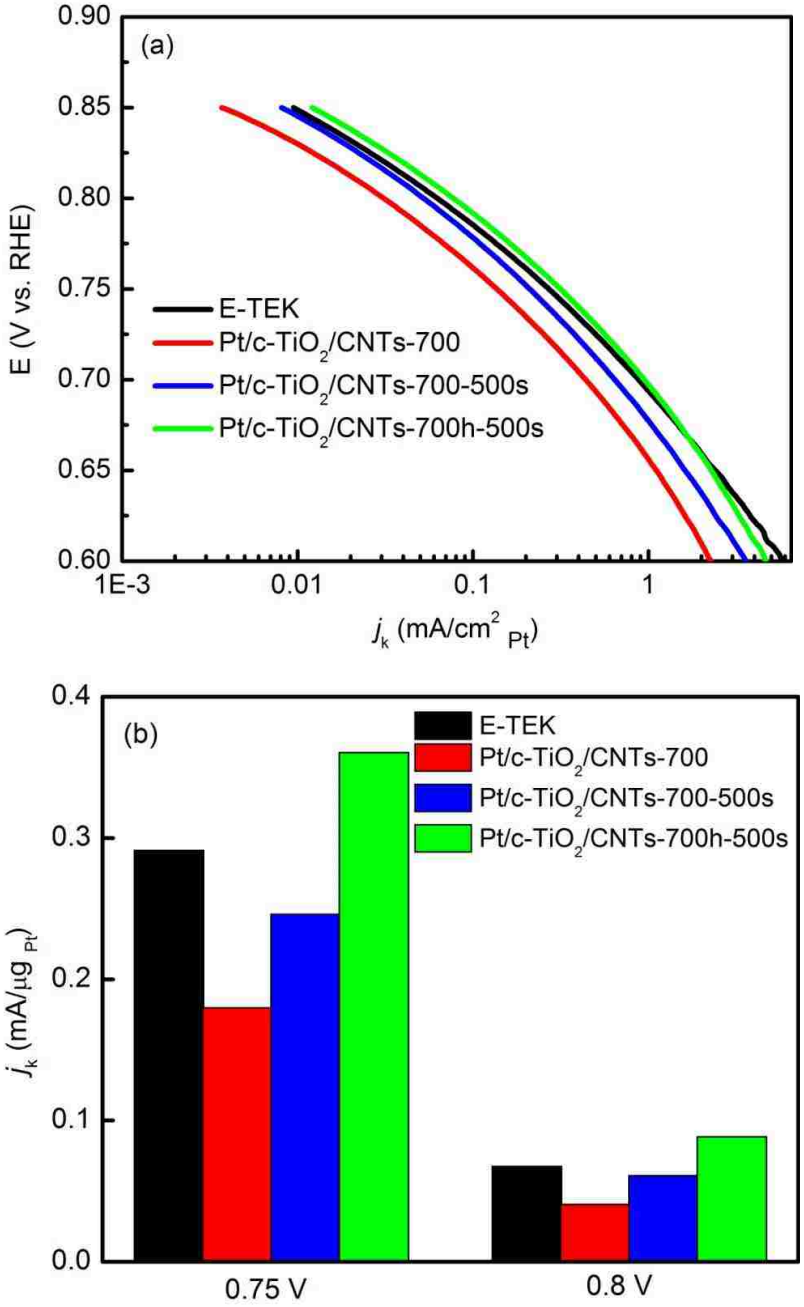

Fig. 9 (a) Tafel plot derived from the ORR curves for the various catalysts, showing that the kinetic mass based current, j_k, of the Pt/c-TiO_2/CNTs-500s catalyst is comparable or better that that of the E-TEK Pt/C catalyst. (b) Comparison of the Pt mass activities of the various catalysts at 0.75 V and 0.80 V.

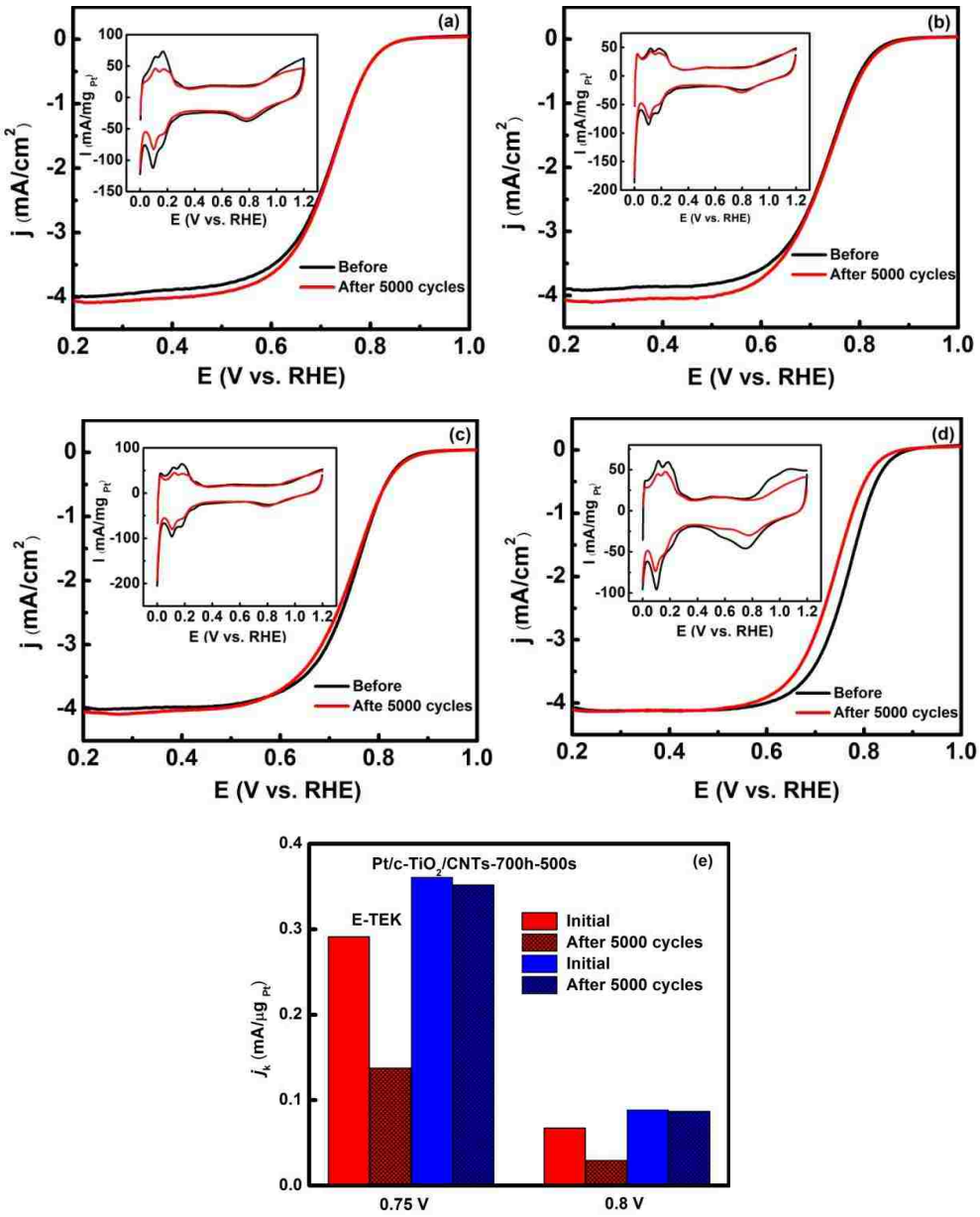

Fig.10 Polarization curves of the ORR before and after 5000 cycles for various catalysts. (a) Pt/c-TiO_2/CNTs-700; (b) Pt/c-TiO_2/CNTs-700-500s; (c)Pt/c-TiO_2/CNTs-700h-500s (d) E-TEK ; (e) comparison of Pt mass activity of Pt/c-TiO_2/CNTs-700h-500s and E-TEK at 0.75 V and 0.80 V. Electrolyte: O_2 saturated 1.0 M H_2SO_4; electrode rotating speed: 1600 rpm, scan rate: 10 mV s^{-1}. The potential cycling was performed from 0.6-1.0V in air saturated 1.0 M H_2SO_4. The insert shows the CV curves before and after 5000 cycles.

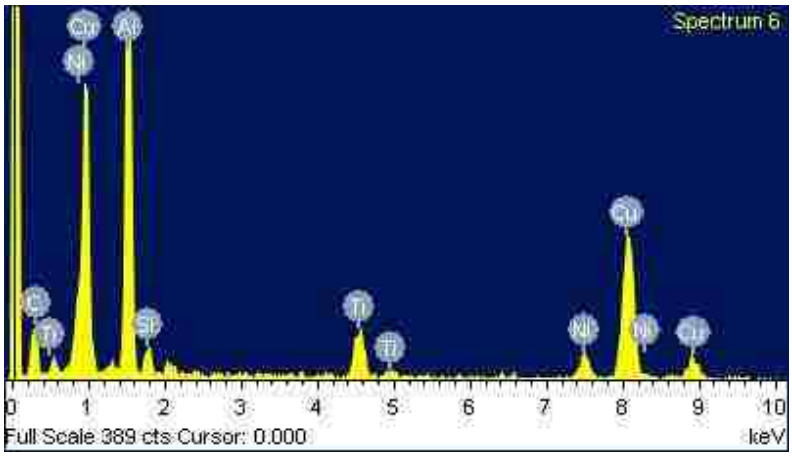

Fig. S1. EDX of a TiO_2/CNT sample supported on a copper mesh TEM grid, showing the presence of Ti element. Some background elements (Cu, Ni, Al) of the sample support (TEM grid) are also present.

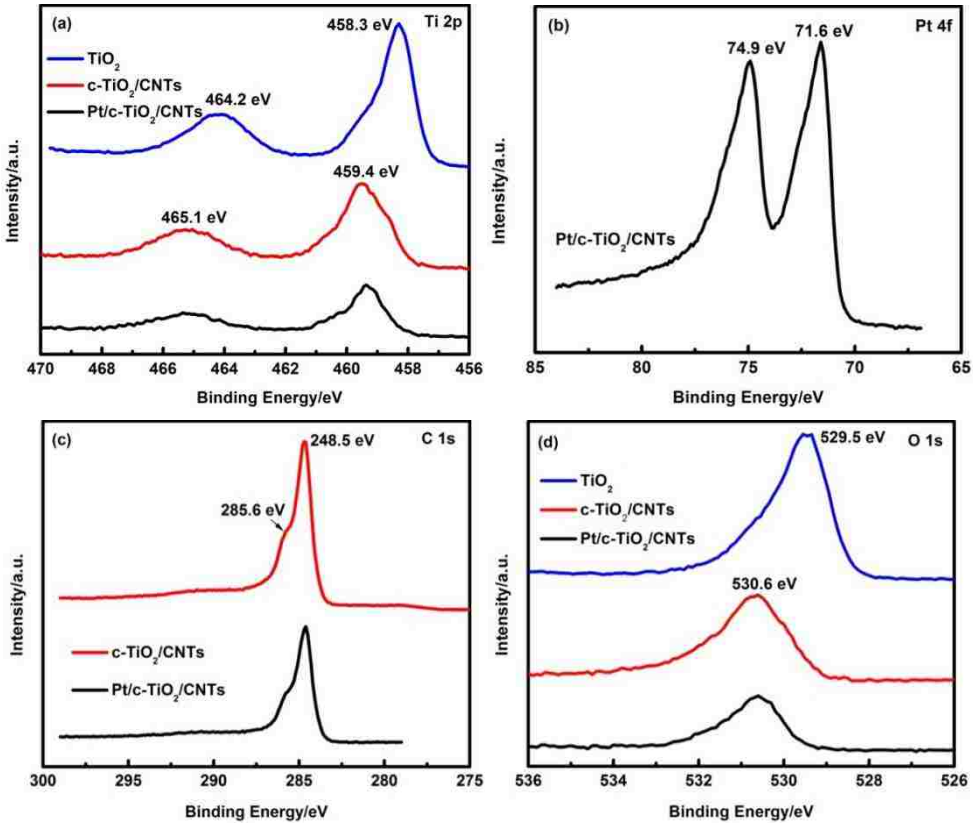

Fig. S2. Comparison of XPS results of Ti 2p, O1s, C 1s and Pt 4f from samples of pure TiO_2, c-TiO_2/CNTs and Pt/c-TiO_2/CNTs. They show that although carbon doping shifts the binding energies, Pt deposition does not.

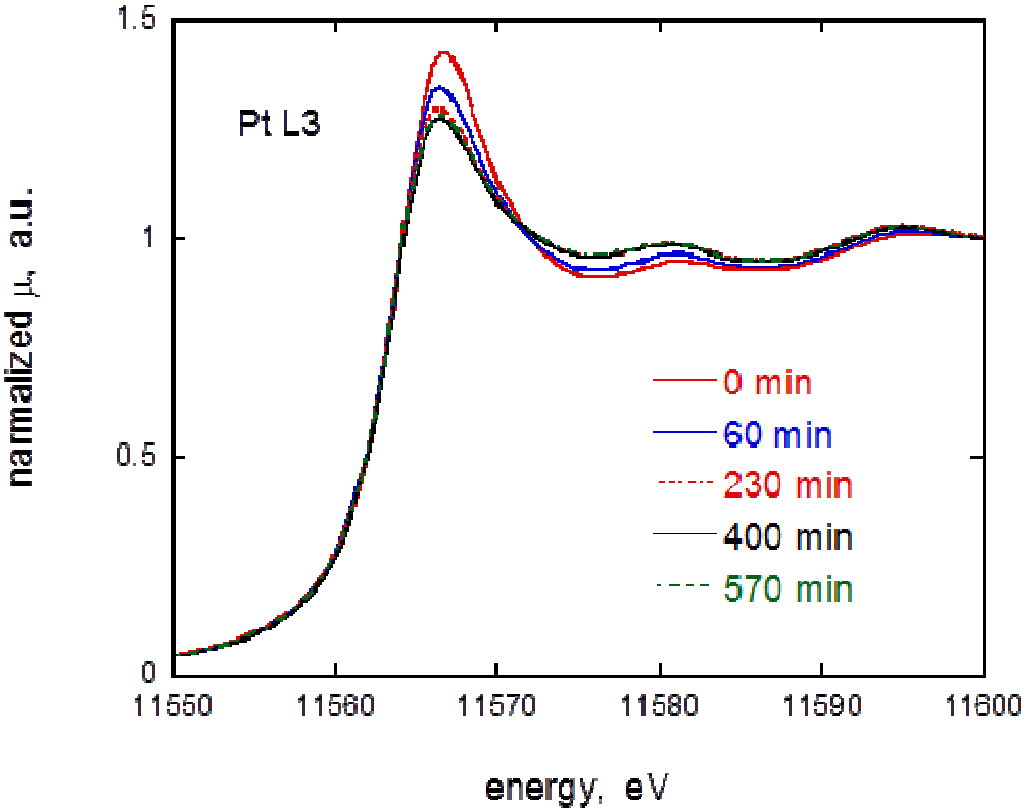

Fig. S3. In situ XANES spectra of Pt L3 edge from $Pt/TiO_2/CNTs$ in 1M $HClO_4$ at a potential of 0.41 V with polarization time.

Figure S3 shows in situ XANES spectra of Pt L3 edge from $Pt/TiO_2/CNTs$ in 1M $HClO_4$ at a potential of 0.41 V with polarization time. The intensity of the white line (the first peak) is high immediately after applying the potential, due to the presence of Pt oxides; it decays very slowly with polarization time due to reduction of the Pt oxides. The slow reduction is likely caused by the poor conductivity of the TiO_2 support. Such that the long delay in reduction is not observed for the conductive supports, such as $Pt/c\text{-}TiO_2/CNTs$.

Table 1 Processing temperature (T) and duration (t) of the catalysts

Catalysts	Carbon doping		Oxide annealing		Pt heat treatment	
	T (°C)	t (min)	T (°C)	t (min)	T (°C)	t (min)
$Pt/TiO_2/CNTs$	-	-	-	-	-	-
$Pt/c\text{-}TiO_2/CNTs\text{-}500$	500	20	-	-	-	-
$Pt/c\text{-}TiO_2/CNTs\text{-}700$	700	20	-	-	-	-
$Pt/c\text{-}TiO_2/CNTs\text{-}700\text{-}500s$	700	20	-	-	500	60
$Pt/c\text{-}TiO_2/CNTs\text{-}700h$	700	20	700	240	-	-
$Pt/c\text{-}TiO_2/CNTs\text{-}700h\text{-}500s$	700	20	700	240	500	60

Table 2 Coordination numbers (N) and bond lengths (R) from $Pt/TiO_2/CNTs$ and $Pt/c\text{-}TiO_2/CNTs$ and comparison to those of rutile and anatase TiO_2

	$N_{Ti\text{-}Ti}$	$N_{Ti\text{-}O}$	$R_{Ti\text{-}Ti}$ (Å)	$R_{Ti\text{-}O}$ (Å)
Undoped TiO_2	5.1 (±2.4)	6.4 (±0.8)	3.25 (±0.05)	1.93 (±0.01)
C-doped TiO_2	4.3 (±1.5)	5.7 (±0.6)	3.16 (±0.05)	1.96 (±0.01)
Rutile TiO_2	2	6	2.96	1.959[a]
Anatase TiO_2	4	6	3.04	1.946[b]

[a] Four bonds, 1.948 Å; two bonds, 1.980 Å; average, 1.959 Å. [b] Four bonds, 1.937 Å; two bonds, 1.965 Å; average, 1.946 Å

Table 3 ESA of different catalysts

Samples	Initial (cm^2/mg_{-Pt})	After 1000 cycles (cm^2/mg_{-Pt})	ESA Loss (%)
Pt/c-TiO_2/CNTs-500	1216.6	996.2	18.1
Pt/c-TiO_2/CNTs-700	1198.1	1108.5	7.5

II. CARBONTHERMAL SYNTHESIS OF TITANIUM OXY CARBIDE AS ELECTROCATALYST SUPPORT WITH HIGH OXYGEN EVOLUTION REACTION ACTIVITY

Kan Huang[1], Yunfeng Li[1], Yangchuan Xing[2a]
[1]Department of Chemical and Biological Engineering, Missouri University of Science and Technology, Rolla, MO, 65409
[2]Department of Chemical Engineering, University of Missouri at Columbia, Columbia, MO, 65211
[a]Address all correspondence to this author. Email: xingy@missouri.edu

ABSTRACT

Carbothermal reduction of semiconducting TiO_2 into highly conductive titanium oxy carbide (TiO_xC_y) was investigated. The thermally produced uniform carbon layer on TiO_2 (Degussa P25) protects the TiO_2 nanoparticles from sintering and, at the same time, supplies the carbon source for doping TiO_2 with carbon. At low temperatures (*e.g.*, 700 ^{o} C), carbon only substitutes part of the oxide and distorts the TiO_2 lattice to form $TiO_{2-x}C_x$ with only substitutional carbon. When the carbon-doped TiO_2 is annealed at a higher temperature (1100 ^{o} C), x-ray diffraction and x-ray photoelectron spectroscopy results showed at TiO_xC_y, a solid solution of TiO and TiC, was formed, which displays different diffraction peaks and binding energies. It was shown that TiO_xC_y has much better oxygen revolution reaction activity than TiO_2 or $TiO_{2-x}C_x$. Further studies showed that the

obtained TiO_xC_y can be used as support for metal electrocatalyst, leading to a bifunctinal catalyst effective for both oxygen reduction and evolution reactions.

1. INTRODUCTION

Carbon black has for a long time served as electrocatalyst support for porous electrodes in fuel cell and metal-air batteries [1-7]. These carbon particles contribute as reaction sites for the oxygen reduction reaction (ORR) or oxygen evolution reaction (OER), especially during discharge and recharge processes. However, the fact of severe corrosion of carbon materials at high potentials during electrochemical reactions [8] makes such application impractical under long term cell operation in acidic media [9]. Therefore, alternative catalyst supports have to be sought, and recent attentions have been focused on TiO_2 as a stable support candidate [10-12]. Due to the semi-conducting nature of TiO_2, great efforts were taken to improve its electron conductivity.

One type of reduced TiO_2, called Magneli phase (Ti_nO_{2n-1}), has been shown to have high stability and electron conductivity in corrosive electrolyte and at high potentials [13-16]. Yet, the reduction condition for making the Magneli phase is generally rather harsh, requiring very high temperatures under hydrogen, leading to severe sintering and consequently significant loss of surface areas. On the other hand, carbon-modified TiO_2 nanoparticles and nanotube arrays under relatively mild conditions have been demonstrated to be effective in photocatalysis and applied in dye-sensitized solar cells [17-21]. The TiO_2 carbon modification methods include carbon monoxide reduction [20], acetylene recduction [22], flame-made with TiC [19, 23], or polymer TiO_2 composites

[17, 24]. X-ray photoelectron spectroscopy (XPS) results of these samples revealed the presence of carbon in all of them [21]. However, the particles size distributions obtained by these processes are rather broad [25, 26].

Carbon coating has been reported to suppress sintering of TiO_2 during high temperature annealing [17, 22, 24]. The technique could allow tuning the TiO_2 nanoparticle electronic conductivity while maintaining its high surface areas, making it possible to obtain the titanium oxy carbide (TiO_xC_y), which can be viewed as a solid solution of TiO and TiC and various titanium suboxides (TiO_x, $x < 2$) [27]. For example, Hahn *et al.* [27] have reported TiO_2 arrays that were converted into TiO_xC_y with high conductivity and stability during redox cycles. The current work aims at preparing nanoscale TiO_xC_y in a carbothermal process from Degussa P25, which is commercially and cheaply available.

To date, it is quite common that platinized TiO_2 were reported as catalysts in the field of photocatalysis [28, 29]. Also, those active components for OER in bifunctional electrocatalysts in regenerative fuel cells are normally precious metals or their oxides, such as Ir or IrO_2 [30, 31]. However, there is not much literature on such electronically conductive TiO_2 as the substrate for loading Pt electrocatalyst for ORR but also for OER. Herein, we report a carbothermal reduction technique to convert P25 TiO_2 nanoparticles into nanoscaled TiO_xC_y in a one-step, two-stage process. It is shown that the carbon modified TiO_2 has a narrow size distribution. Their sizes increased but remained small at less than 50 nm, even annealed at 1100 ^{o} C. Electrochemical characterizations revealed

that the obtained TiO_xC_y is a very active OER catalyst. Together with Pt, the catalyst is bifunctional, good for both ORR and OER.

2. EXPERIMENTAL

Amorphous TiO_2 powders (P25, Degussa Corp.) with a mean size at 22 nm were thermally coated with carbon under 10% acetylene C_2H_2 in N_2 for 20 min at 700 ^oC in a tubular quartz furnace. After carbon coating, the products were further annealed under 10% H_2 in N_2 between 900 ^oC and 1100 ^oC for another 4 h. The samples were designated as P25-700 for thermally carbon coated TiO_2 at 700 ^oC and P25-700-1100h for the annealed and carbon doped TiO_2 at 1100 ^oC. The latter notation is also referred to c-TiO_2. Pt (10wt.%) loaded on the samples for electrochemical measurements was achieved using a salt reduction method reported previously [32].

The morphologies of the powders were examined by transmission electron microscope (TEM) (Tecnai F20) operating at 300 kV and scanning electron microscope (SEM) (Helios Nano Lab 600) operating at 30 kV. The crystalline phase of the catalysts was analyzed by x-ray diffraction (XRD) equipped with Cu K (α); the XRD data were collected with a Philips X'Pert Diffractometer. XPS (Kratos Axis 165) was used to analyze C(1*s*), Ti(2*p*), and O(1*s*) by employing Al K (α) excitation, operated at 150W and 15kV.

Electrochemical techniques such as cyclic voltammetry (CV), ORR, and OER were used for testing electronic conductivity and measuring the electrochemical activities of the titanium oxide nanopowders. CV of 10 wt.% Pt loaded or Pt-free was carried out at a scan rate of 20 mV/s in N_2 purged 1.0 M H_2SO_4 from 0-1.2 V vs. RHE. All measurements were performed with a standard three-electrode cell using a glassy carbon rotating disk electrode (Pine Instruments) supporting 0.02 mg catalyst as working electrode. A Pt wire was used as the counter electrode and a saturated Ag/AgCl as reference electrode. CV, OER and durability of the catalysts were carried in a N_2-saturated 1.0 M H_2SO_4 electrolyte solution. ORR was carried in an O_2-saturated 1.0 M H_2SO_4 electrolyte solution.

3. RESULTS AND DISCUSSION

Fig. 1 (a)-(f) show the morphologies of P25 untreated and thermally treated at different temperatures. After carbon coating process at 700 ^{o} C, the amorphous TiO_2 crystallized and the mean size grows from the original 22 nm to about 35 nm (see Fig. 1(b)). Further annealing up to 1000 ^{o}C, the particles only yield tiny growth and are still in a range of 30~40 nm; no obvious sintering was detected and the shape of particles still appears spherical, shown in Figs. 1 (c) and 1 (d). When the annealing temperature was increased to 1100 ^{o} C, some particles agglomerated and their sizes increased to about 55 nm, see Fig. 1 (e). A sample of P25 was directly annealed in air 800 ^{o} C for the same

duration, resulting in a substantial growth of particles size (up 300 nm), as can be seen from Fig. 1 (f). It is clearly shown that the carbon nanocoating is necessary to prevent severe sintering in the TiO_2 nanoparticles.

Further investigation of these carbon doped TiO_2 morphology by TEM revealed the reason of the suppression of particle growth. Fig. 2 presents the TEM micrographs of P25-700 in Fig. 2 (a) and P25-700-1100h in Fig. 2 (b). The dark areas are crystalline TiO_2 particles, whose lattice spacing is shown in the inset (Fig. 2(a)), and the lighter area surrounding the darker areas are amorphous carbon coatings with a thickness of *ca*. 5 nm. Apparently, the coating process produces an extremely uniform thin carbon coating on the TiO_2 surface. The TEM images also indicate that carbon existed as amorphous which is consistent with the XRD finding and will be further discussed below.

The carbon coating prevents the interaction of individual TiO_2 particles through surface or solid diffusion, limiting their sintering. With further annealing under N_2/H_2 at 1100 ^oC, as shown in Fig. 2 (b), the particles started to coarsen and grow. It was found that some surrounding carbon coating has disappeared. However, some free carbon still can be seen. Koc *et al.* [33] suggested that the reaction of carbon with TiO_2 only complete above 1500 ^oC. No further studies were conducted at higher temperature to avoid growth.

Fig. 3 shows the XRD patterns of the samples annealed at different temperatures. After carbon coating at 700 ^oC, all peaks are related to the TiO_2 anatase and rutile phase, implying pyrolytic carbon formed was amorphous (no graphitic phase) [21, 34].

Annealing at 900 ^{o}C did not produce new phases either. However, annealing at 1000 ^{o}C, clearly five new diffraction peaks at $2\theta \approx 37^{o}$, 43^{o}, 62^{o}, 74^{o} and 78^{o} were formed, which all can be attributed to the formation of titanium oxy carbide (TiO_xC_y) [27, 33]. As Hahn *et al.* [27] suggested, titanium oxy carbide is a solid solution of TiO in TiC and various suboxides. XPS analysis below will further support the formation of titanium oxy carbide. Further increasing temperature to 1100 ^{o}C, the anatase and rutile phases disappeared; the TiO_xC_y peaks became shaper and well defined, which means the formation of TiO_xC_y was completed in the duration of treatment.

The chemical states of O, Ti and C were investigated by XPS, and the results were shown in Fig. 4. Two C 1*s* peaks found at binding energies (BEs) of 284.6 eV and 285.7 eV in all powders are attributed to the carbon source from carbon tape (for sample mounting) and carbonaceous species (in sample) [35]. No additional C1s peak was found near 281.5 eV, which would correspond to TiC [36]. This result is indicative that even annealing at 1100 ^{o}C, the doped carbon can only interact with TiO_2 to form TiO_xC_y, but not TiC. Generally, TiC can be produced by carbon reduction of TiO_2 only at temperature of 1500 ^{o}C or above [33].

Fig. 4(b) presents the Ti 2*p* spectra. For pure TiO_2 samples, Ti $2p_{3/2}$ and $2p_{1/2}$ peaks can be found at BEs of 458.3 eV and 464.1 eV, respectively. Small peak shifts of Ti 2*p* towards higher binding energies can be observed in all samples. According to Li *et al.* [14], pure TiO_2 displays BEs at 464.2 eV and 485.5 eV, while the reduced form, Magneli phase Ti_4O_7, has BEs at 464.7 eV and 459.0 eV. Göpel *et al.* [37] suggested that the shift

of Ti 2*p* from defect-free TiO_2 is caused by surface oxygen vacancy defects. Carbon can be incorporated into TiO_2 lattice or substituted for oxygen, which can have synergistic effect with oxygen vacancies, resulting in the change of electron structure between conducting band and valence band [38]. Our recently observations also reported this Ti 2*p* shift [39]. Therefore, the Ti2*p* shift suggests that a reduced oxide layer was formed from carbon doping. When annealing at 1100 ^{o}C, a typical shoulder belonging to TiO_xC_y was detected [27]. This broad shoulder can be divided into several groups, titanium suboxide (TiO_x), TiO&TiC and Ti, as Blackstock *et al.* suggested [40]. The Ti 2*p* spectra in sample P25-700-1100h consolidated our previous argument that TiO_xC_y was formed.

The O 1*s* spectra showed one peak at 529.6 eV in pure TiO_2, which is due to the Ti-O bonding in TiO_2. By doping with carbon and further annealing at 1000 ^{o}C, two new peaks were discovered. The peak at 529.9 eV can be ascribed to the contribution of Ti-O bond, even though there is a small shift. The shift may be caused by replacement of oxygen by carbon to form $TiO_{2-x}C_x$, with trace carbon distortion to the TiO_2 lattice. The other peak found at 533.6 eV can be assigned to C-O in carboxyl groups [41]. When annealed at above 1000 ^{o}C, the O 1*s* peak at 533.6 eV disappeared and an obvious shift was observed for the Ti-O binding, which was also found by Hahn *et al.* [27]. Both XRD and Ti 2*p* spectra have shown the formation of TiO_xC_y, and we can ascribe the O 1s at 530.5 eV to the Ti-O bonding in TiO_xC_y.

Fig. 5 compares the electrochemical activity of Pt/P25 with that of Pt/P25-700. It clearly demonstrates that Pt nanoparticles supported on P25-700 exhibit much higher

electrochemical activity, while Pt loaded on undoped TiO_2 shows negligible catalytic activity due to low conductivity of the support. These results demonstrate that carbon doping indeed significantly increased the electronic conductivity in P25 with carbonthermal treatment. The combined effects of substitutional carbon, interstitial carbon and oxygen vacancy contribute to the change in electronic band structure of TiO_2 [38], resulting in the increase of its conductivity. The close contact of Pt with its conducting support enables the catalyst to have typical Pt electrochemical activity in the CV, as displayed in the regions of hydrogen adsorption/desorption, platinum oxidation, and platinum-oxide reduction [11].

CV tests of thermally treated TiO_2 were performed to investigate the electrochemical activities of different powders, results of which are shown in Fig. 6. The anodic peaks at ~0.65 V and cathodic peaks at ~0.58 V in Fig. 6 (a) are associated with the oxidation and reduction of the surface oxide group. The bigger double layer capacity in P25-700-1000h and P25-700-1100h can be attributed to the formation of TiO_xC_y since surface carbon coating is consumed during annealing, as observed from the TEM images (Fig. 2(b)). OER was carried to investigate the catalytic activity towards oxidation of water to generate molecular oxygen in acidic electrolyte medium $2H_2O=4e^-+4H^++O_2$, and the onset potential for this reaction is a basic criterion to evaluate the efficiency of the catalyst.

According to Nowotny *et al.* [42], the presence of defects at TiO_2 surface, *e.g.*, oxygen vacancies, is essential for the water splitting. Undoped TiO_2 showed the worst

OER activity, as can be seen in Fig. 6 (b). The sample has the highest onset potential and lowest current, which could be attributed to its low surface defects [42-44]. Introducing carbon doping and further annealing can create oxygen vacancy as predominant defects, as confirmed by the formation of reduced Ti from previous XPS analysis [11, 14, 20, 27]. Annealed at 1100 ^{o}C, carbon coated TiO_2 has almost completed the transformation from TiO_2 to TiO_xC_y, which has the most oxygen vacancies. As a result, the catalyst showed the best OER catalytic activity, with lowest onset potential at 1.45 V.

Many efforts have been made in seeking other replace the expensive OER catalyst, IrO_2, which is considered to be the state of the art. Among various candidates, perovskites exhibited comparable or better OER activity than previous reports. Suntivich *et al.* [45] most recently reported perovskites with an onset potential at range of 1.5 V~165 V (*vs.* RHE). At 0.4 V overpotential vs. RHE (1.23 V), the OER activities fall into the range of 0.12~14 mA/mg $_{catal.}$. The TiO_xC_y in Fig. 6 (b) yield a ~5 mA/mg $_{catal.}$ current density at 1.6 V, therefore having a comparable OER activity as the reported perovskites and further demonstrating the substantial OER activity of the titanium oxy carbide.

However, none of our samples exhibit ORR activity, as shown in Fig. 6 (c), in which large overpotentials and negligible currents were observed. To obtain ORR activity, Pt was deposited on the TiOxCy and typical ORR curves [46] were obtained (Fig. 6(c)). An onset potential at ~0.85 V shows that the TiO_xC_y support is an excellent alternative support to the high surface area carbon black. Altogether, the catalyst Pt/TiO_xC_y has both OER and ORR activities, demonstrating an effective bifunctional catalyst.

4. CONCLUSIONS

In this paper, we demonstrated a carbonthermal technique that allows making nanoscale TiO_xC_y from commercial TiO_2 P25 nanoparticles. The process is a simple one-step, two-stage process. It can be achieved in most lab furnaces under relatively low temperature. This process involves a carbon coating stage, followed by an annealing stage. By doing so, sintering of the nanoparticles is substantially suppressed, allowing us to maintain the large surface areas needed for catalyst support. It was also found that partial carbon substitution in the TiO_2 lattice occurred at below 1000 ^oC. But at 1100 ^oC, the TiO_2 nanoparticles can be completely converted to TiO_xC_y, with only a small increase in particle size. It was found that markedly improved electronic conductivity can be obtained in TiO_xC_y, which makes it a good substrate for supporting Pt electrocatalyst. The TiO_xC_y nanopowder obtained showed a significant activity towards OER. By depositing Pt on it, a bifunctional catalyst, Pt/TiO_xC_y, was demonstrated to be effective for both ORR and OER.

5. ACKNOWLEDGMENTS

The authors would like to thank partial financial support for this research from the U.S. Department of Energy ARPA-E grant DE-AR0000066. We thank Dr. Eric Bohannan for XRD analysis, Mr. Brian Porter for XPS analysis and Dr. Kai Song for taking TEM images.

REFERENCES

[1] J. Newman and W. Tiedemann, AIChE Journal, 1975, 21, 25-41.

[2] S. Litster and G. McLean, J. Power Sources, 2004, 130, 61-76.

[3] A.L. Dicks, J. Power Sources, 2006, 156, 128-141.

[4] X.L. Wang, H.M. Zhang, J.L. Zhang, H.F. Xu, Z.Q. Tian, J. Chen, H.X. Zhong, Y.M. Liang and B.L. Yi, Electrochim., 2006, 51, 4909-4915.

[5] S.-W. Eom, C.-W. Lee, M.-S. Yun and Y.-K. Sun, Electrochim. Acta, 2006, 52, 1592-1595.

[6] T. Ogasawara, A. Débart, M. Holzapfel, P. Novák and P.G. Bruce, J. Am. Chem. Soc., 2006, 128, 1390-1393.

[7] A. Débart, J. Bao, G. Armstrong and P.G. Bruce, J.Power Sources, 2007, 174, 1177-1182.

[8] J. Willsau and J. Heitbaum, J. Electroanalytical Chemistry and Interfacial Electrochemistry, 1984, 161, 93-101.

[9] S.K. Natarajan and J. Hamelin, J. Electrochem. Soc., 2009, 156, B210-B215.

[10] H. Song, X. Qiu, F. Li, W. Zhu and L. Chen, Electrochem. Commun., 2007, 9, 1416-1421.

[11] A. Bauer, K. Lee, C. Song, Y. Xie, J. Zhang and R. Hui, J. Power Sources, 2010, 195, 3105-3110.

[12] R.E. Fuentes, J. Farell and J.W. Weidner, Electrochem. Solid-State Lett., 2011, 14, E5-E7.

[13] F.C. Walsh and R.G.A. Wills, Electrochim. Acta, 2010, 55, 6342-6351.

[14] X. Li, A.L. Zhu, W. Qu, H. Wang, R. Hui, L. Zhang and J. Zhang, Electrochim. Acta, 55, 2010, 55, 5891-5898.

[15] T. Ioroi, H. Senoh, S.-i. Yamazaki, Z. Siroma, N. Fujiwara and K. Yasuda, J. Electrochem. Soc., 2008, 155, B321-B326.

[16] W.-Q. Han and X.-L. Wang, Appl. Phys. Lett., 2010, 97, 243104-243103.

[17] T. Tsumura, N. Kojitani, I. Izumi, N. Iwashita, M. Toyoda and M. Inagaki, J. Mater. Chem., 2002, 12, 1391-1396.

[18] H. Irie, Y. Watanabe and K. Hashimoto, Chem. Lett., 2003, 32, 772-773.

[19] Y. Choi, T. Umebayashi and M. Yoshikawa, J. Mater. Sci., 2004, 39, 1837-1839.

[20] J.H. Park, S. Kim and A.J. Bard, Nano Lett., 2005, 6, 24-28.

[21] C.A. Grimes and G.K. Mor: TiO2 Nanotube Arrays: Synthesis, Properties, and Applications , Springer Science, New York USA, 2009.

[22] H.K. Kammler and S.E. Pratsinis, J. Mater. Res., 2003, 18, 2670-2676.

[23] Y. Choi, T. Umebayashi, S. Yamamoto and S. Tanaka, J. Mater. Sci. Lett., 2003, 22, 1209-1211.

[24] M. Inagaki, Y. Hirose, T. Matsunaga, T. Tsumura and M. Toyoda, Carbon, 2003, 41, 2619-2624.

[25] M. Inagaki, F. Kojin, B. Tryba and M. Toyoda, Carbon, 2005, 43, 1652-1659.

[26] M. Toyoda, T. Yano, B. Tryba, S. Mozia, T. Tsumura and M. Inagaki, Appl. Catal. B: Environmental, 2009, 88, 160-164.

[27] R. Hahn, F. Schmidt-Stein, J. Salonen, S. Thiemann, Y. Song, J. Kunze, V.-P. Lehto and P. Schmuki, Angew. Chem. Int. Ed., 2009, 48, 7236-7239.

[28] H.S. Kibombo and R.T. Koodali, J. Phys. Chem. C, 2011, 115, 25568-25579.

[29] J. Lee and W. Choi, J. Phys. Chem. B, 2005, 109, 7399-7406.

[30] T. Ioroi, N. Kitazawa, K. Yasuda, Y. Yamamoto and H. Takenaka, J. Electrochem. Soc., 2000, 147, 2018-2022.

[31] S. Song, H. Zhang, X. Ma, Z.-G. Shao, Y. Zhang and B. Yi, Electrochem. Commun., 2006, 8, 399-405.

[32] Y. Xing, J. Phys. Chem. B, 2004, 108, 19255-19259.

[33] R. Koc and J.S. Folmer, J. Mater. Sci. , 1997, 32, 3101-3111.

[34] X. Chen and S.S. Mao, Chem. Rev. 2007, 107, 2891-2959.

[35] E.A. Reyes-Garcia, Y. Sun, K.R. Reyes-Gil and D. Raftery, Solid State Nuclear Magnetic Resonance, 2009, 35, 74-81.

[36] Y. Luo, S. Ge, Z. Jin and J. Fisher, Appl. Phys. A: Materials Science & Processing, 2010, 98, 765-768.

[37] W. Göpel, G. Rocker and R. Feierabend, Phys. Rev. B, 1983, 28, 3427.

[38] C. Di Valentin, G. Pacchioni and A. Selloni, Chem. Mater., 2005, 17, 6656-6665.

[39] K. Huang, K. Sasaki, R. Adzic and Y. Xing, J. Mater. Chem., 2012, 22, 16824-16832 .

[40] J.J. Blackstock, C.L. Donley, W.F. Stickle, D.A.A. Ohlberg, J.J. Yang, D.R. Stewart and R.S. Williams, J. Am. Chem. Soc., 2008, 130, 4041-4047.

[41] C. Moreno-Castilla, F.J. Maldonado-Hódar, F. Carrasco-Marín and E. Rodríguez-Castellón, Langmuir, 2002, 18, 2295-2299.

[42] J. Nowotny, T. Bak, M.K. Nowotny and L.R. Sheppard, J. Phys. Chem. B, 2006, 110, 18492-18495.

[43] M. Calatayud, A. Markovits, M. Menetrey, B. Mguig and C. Minot, Catal. Today, 2003, 85, 125-143.

[44] M. Menetrey, A. Markovits and C. Minot, Surf. Sci., 2003, 524, 49-62.

[45] J. Suntivich, K.J. May, H.A. Gasteiger, J.B. Goodenough and Y. Shao-Horn, Science, 2011, 334, 1383-1385.

[46] Y. Xing, Y. Cai, M.B. Vukmirovic, W.-P. Zhou, H. Karan, J.X. Wang and R.R. Adzic, J. Phys. Chem. Lett., 2010, 1, 3238-3242.

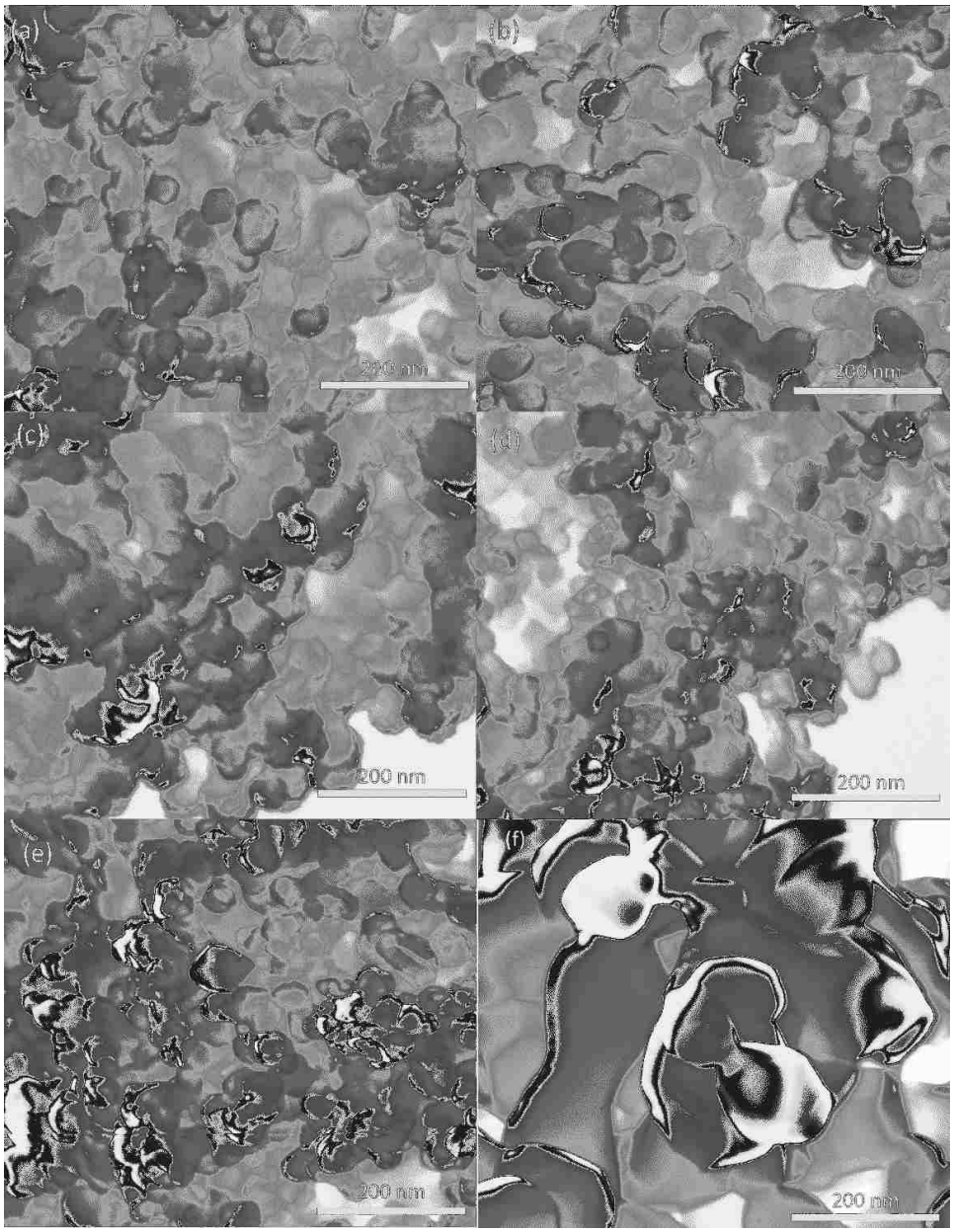

Fig. 1 SEM images of titanium oxide nanopowders obtained under different thermal treatments. (a) P25: original TiO_2, (b) P25-700: P25 carbon coated at 700 ^{o}C, (c) P25-700-900h: P25 carbon coated at 700 oC and further annlead at 900 ^{o}C, (d) P25-700-1000h: P25 carbon coated at 700 oC and further annealed at 1000 ^{o}C, (e) P25-700-1100h: P25 carbon coated and further annlead at 1100 ^{o}C, and (f) P25 anneald in air at 800 ^{o}C. Annealing time was 4 h for all samples.

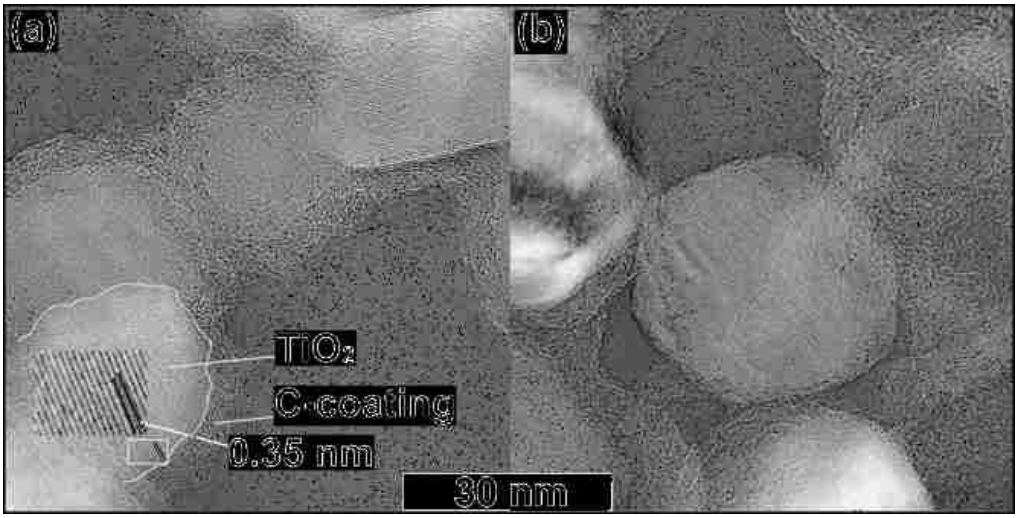

Fig. 2 TEM micrographs of (a) P25-700, and (b) P25-700-1100h, showing uniform carbon coating on the oxide nanoparticles. A contrast is observed between the amorphous carbon and the crysalline titanium oxide or oxy carbide. The inset in (a) shows the lattice spacing of TiO_2.

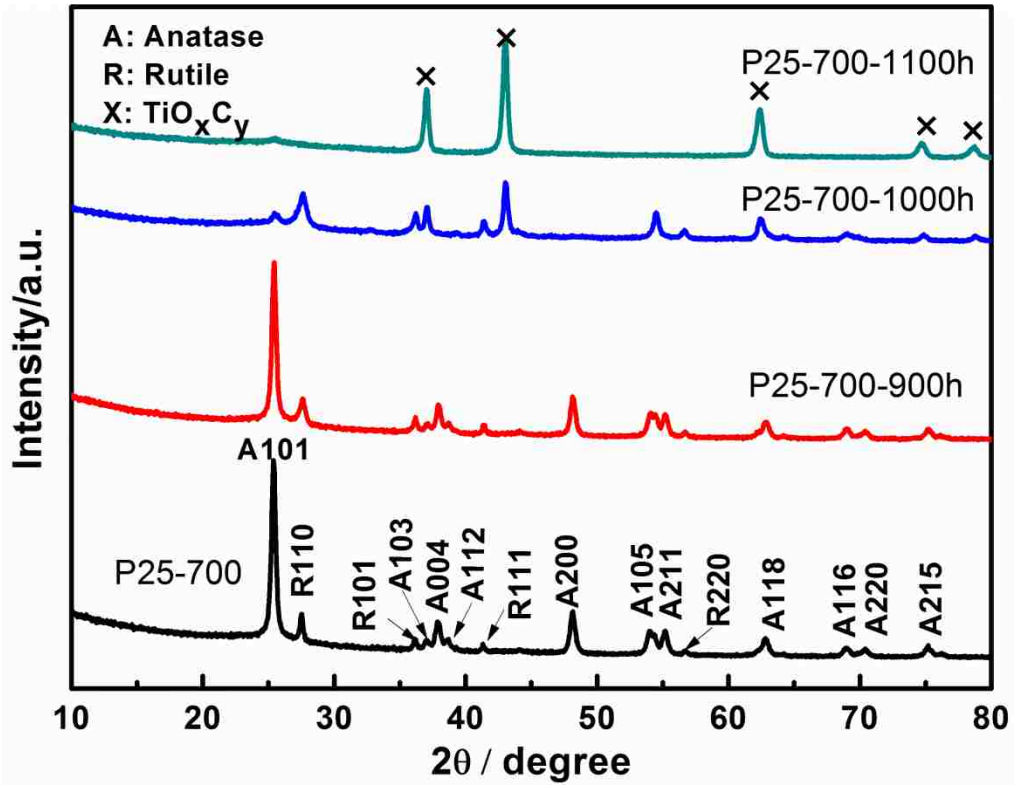

Fig. 3 XRD patterns of P25-700 and P25-700 post annealed at 900, 1000, and 1100 ^{o}C. Complete conversion to TiO_xC_y was found at 1100 ^{o}C.

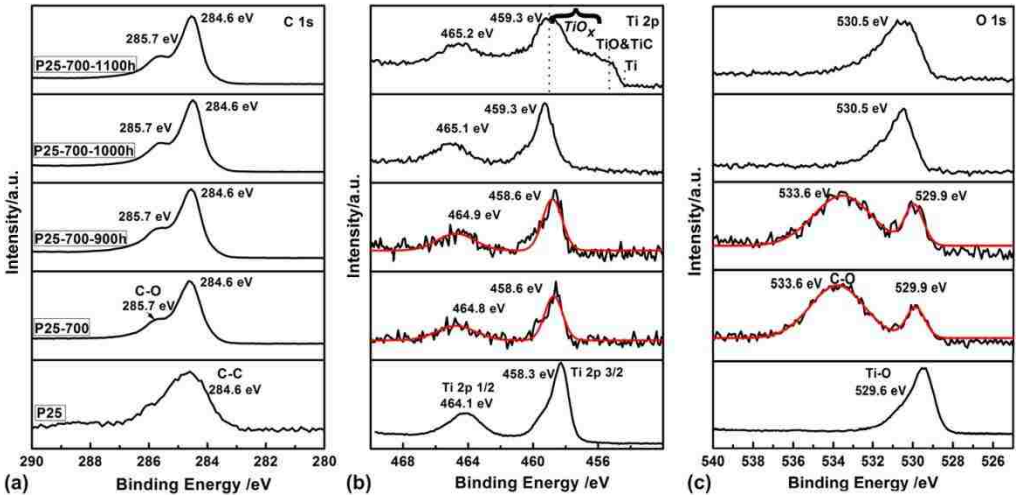

Fig. 4 XPS results of C 1s, O 1s and Ti 2p for P25, P25-700, P25-700-900h and P25-700-1100h. A broad shoulder is observed in the last sample, showing formation of TiO_xC_y.

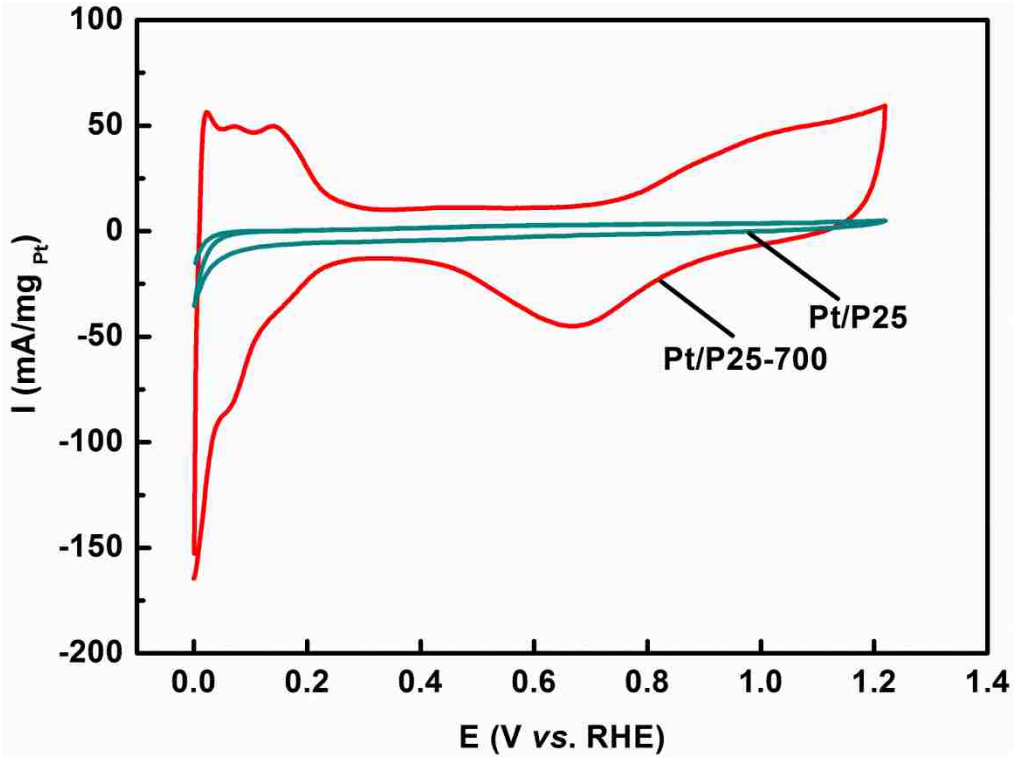

Fig. 5 Cyclic voltammograms of 10 wt.% Pt supported on samples P25 and P25-700 in 1 M H_2SO_4. Much larger currents were observed in the latter sample, which is attibuted to the much higher conductivity of the carbon doped support.

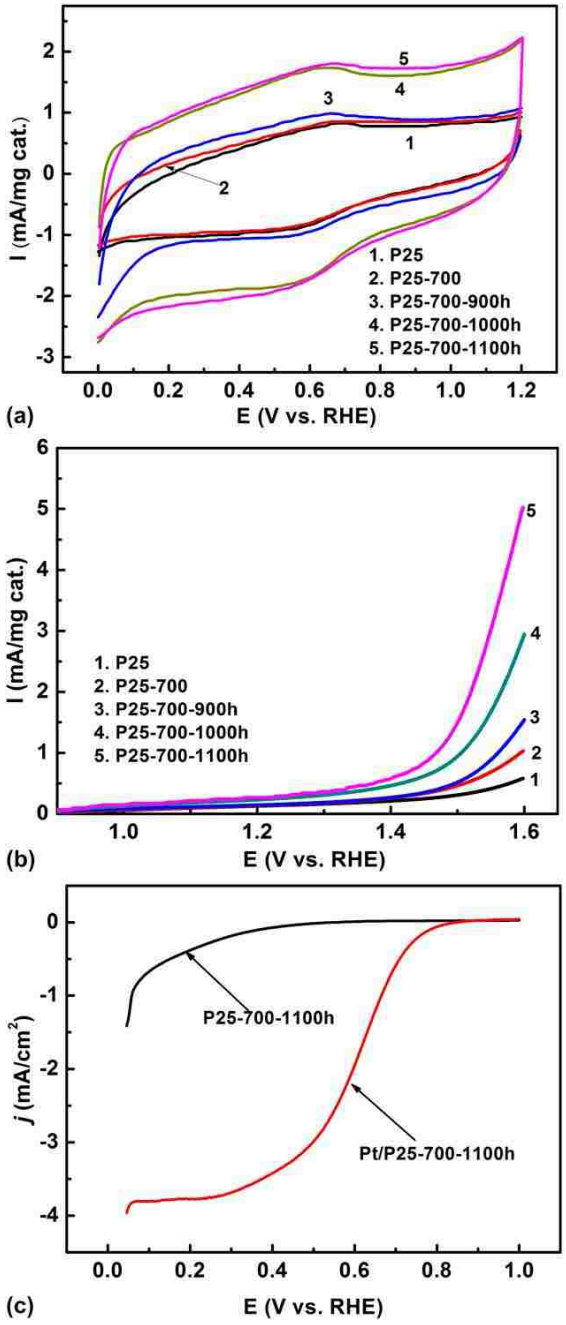

Fig. 6 Electrochemical characterization: (a) cyclic voltammograms of undoped and doped TiO_2 in N_2 saturated 1.0 M H_2SO_4 with scanning rate at 50 mV/s, (b) OER results of the corresponding nanopowder in N_2 saturated 1.0 H_2SO_4 with scanning rate at 5 mV/s. (c) Typical ORR reuslts of TiO_xC_y nanopowders in O_2 saturated 1.0 M H_2SO_4 with scanning rate at 5mV/s, with or without Pt electrocatalyst.

III. A HYBRID LI-AIR BATTERY WITH BUCKYPAPER AIR CATHODE AND SULFURIC ACID ELECTROLYTE

Yunfeng Li[1], Kan Huang[1], Yangchuan Xing[2a]

[1]Department of Chemical and Biological Engineering, Missouri University of Science and Technology, Rolla, MO, 65409
[2]Department of Chemical Engineering, University of Missouri at Columbia, Columbia, MO, 65211
[a]Address all correspondence to this author. Email: xingy@missouri.edu

ABSTRACT

We demonstrate a type of carbon nanotube based buckpaper cathode in a hybrid electrolyte Li-air battery (HyLAB) that showed outstanding discharing performances. The HyLAB has sulfuric acid as the catholyte and a large active electrode area (10 cm^2). The active cathode layer was made from a buckypaper with 5 wt.% Pt supported on carbon nanotubes (Pt/CNTs) for oxygen reduction and evolution. A similar cathode was constructed with a catalyst of 5 wt.% Pt supported on carbon black (Pt/CB). It is demonstrated that sulfuric acid can achieve high discahrgeing current densities while maintaining relatively high cell potentials. The cell with Pt/CNTs showed a much better performance than Pt/CB at high current densities. The HyLAB with Pt/CNTs achieved a discharging capacity of 306 mAh/g and a cell voltage of 3.15 V at 0.2 mA/cm^2. The corresponding specific energy is 1067 Wh/kh based on the total weight of the sulfuric

acid. Slow decrease in performance was observed, but it can be recovered by refilling the cell with new electrolyte after continuous discharging of more than 75 h. A charge-discharge experiment at 0.2 mA/cm^2 showed that the cell was rechargeable with a capacity of more than 300 mAh/g.

1. INTRODUCTION

Li-air batteries have gained much attention as energy storage systmes due to their high energy dnesities, comparable to that of gasoline in the theoretical values [1-3]. An advantage of Li-air batteries is that oxygen is not stored in the cthode but acquired free from ambient air during discharge. Major efforts have been focused on non-electrolyte Li-air batteries to avoid the intensive reaction between water and the Li metal [4-10]. However, Li-air battery with non-aqueous electrolytes is cathode-limited due to that the electrolytes cannot dissolve the solid lithium oxide products, which clog the pores and choke the air breathing cathode. In addition, moisture in ambient air can still degreade non-aqueous electrolytes and react with lithium metal causing self-discharge. These problems directly lead to a short life of non-aqueous Li-air battery.

Aqueous-based systems represent an alternative approach to long operational battery lifr. A water-stable lithium electrode can be devdloped by employment of a LISICON-type lithium ion conducting glass ceramic (LICGC) membrane [11-14]. This impermaeable LiCGC membrane can prevent direct lithium reaction with water.

Consequently, a hybrid electrolyte Li-air battery (HyLAB) can be constructed. Already demonstrated, aqueous electrolytes of acidic [13, 15], neutralized [12], and basic [14, 15] solutions have been used in HyLABs in recent years. Neutralized and basic electrolytes have overall reaction of $2Li+H_2O+0.5O_2 = 2LiOH$, and the theoretical cell potential is 3.43 V [15]. In acidic electrolytes, especially strong acid solutions, the cell reaction is $2Li+0.5O_2+2H^+ = 2\ Li+H_2O$, which yields a theoretical open circuit voltage (OCV) of 4.274 V. Acid can dissolve lithium oxide, preventing clogging in the air breathing channels in the cathode. Such cell can have a practical discharge of 0.2 mA/cm^2 [12, 13], which is much higher than that of non-aqueous electrolyte cell (*ca.* 2.6-2.7 V) [5, 6, 15]. Furthermore, smaller charge-discharge polarizations have been observed in acidic electrolyte cells with the use of Pt catalyst, necessary for the oxygen reduction reaction (ORR) at the cathode, which is $O_2+4H^++4e^- = 2H_2O$, involving 4 electron transfer in acidic medium.

There are two most relevant studies of rechargeable HyLAB using acidic electrolytes. Zhang *et al*. [13] reported a HyLAB using an acetic acid-lithium acetate electrolyte, and most recently Li *et al.* [16] reported a HyLAB based on 0.1 M phosphous acid and 1 M lithium dihydrogen phosphate as catholyte. Both cells reached a high discharge capacity of *ca.* 220 mAh/g and a specific energy of ca. 770Wh/kh, wherea the mass is based on that of the acid in the electrolytes. The test duration of the charge-discharge to reach this capacity was between 1 and 3 h. Those cell used high loading Pt catalysts (Pt-black or 40wt.% Pt/C) in the cathodes. In a priamry Li-air cell,

Kowalczk *et al.* [15] showed that it can be discharged for more than 6 days at 0.1 mA/cm^2 in 5.25 M H_2SO_4 catholyte at a cell potential of 3.2 V.

In this work, we demonstrated a rechargeable HyLAB with sulfuric acid aqueous solution as the catholyte and investigated its charge-discharge performance. We chose sulfuric acid as the catholyte, in addition to the advantages of acids mentined above, due to its electrochemical stability and non-volatility during battery charge-discharge. As lithium sulfate has much solubility in water, and theoretically, all sulfuric acid in 1.0 M H_2SO_4 can be electrochemically converted into lithium sulfate, it can keep the product, lithium sulfate, completely dissolve in the solution. Sulfuric acid also has a relatively high theoretical capacity (479 mAh/g with Li mass included and 546 mAh/g without Li metal) and a specific energy (2046 Wh/kg) [17]. Since carbon nanotubes (CNTs) and carbon black (CB) can yield different porosity and structures in the air diffusion cathode, we prepared two structures of the catalyst layer, one with CNTs and the other with CB, and make a comparison on their cell performances. In addition, a large electroactive area cell (10 cm^2) is demonstrated in a full cell charge-discharge experiment.

2. EXPERIMENTAL METHODS

2.1. Air Cathode Preparation. The air cathode consists of an active catalyst layer, a transition layer and the backing layer of Toray® paper, which are laminated together. The preparation of Pt/CNT catalysts (CNTs from NanoLab, 50± 15 nm) was

reported elsewhere [18]. The air-breathing cathodes were prepared as follows. 10mg carbon nanofibers (CNT ~150 nm in diameter and ~10 μm long, Pyrograf, PR-24-XT-LHT) and 10 mg Pt/CNT catalysts (5 wt.% Pt) were dispersed under sonication in *ca.* 8 mL ethanol in two separated beakers. First, the CNF ethanol dispersion was vacuum filtered through a 0.4μm Millipore ISOPORE® membrane (47 mm diameter). Then filtration of the 10 mg pt/CNT ethanol dispersion was done on the same Millipore membrane covered with the CNF layer. This produced a buckypaper of catalyst layer based on the Pt/CNTs. The resulted total thickness of this buckypaper layer is *ca.* 60 μm. This buckypaper was laminated onto a Toray carbon paper (Fuel Cell Store, TGP-H-030) at 140 °C and a pressure of 2 atm, with the CNF side on the Toray paper. Repeating the same process using 5 wt.% Pt/CB E-TEK catalysts produced the catalyst layer with the CB structure. Again, the transition layer is CNF. We found that the transition CNF layer can serve well to support both the Pt/CNT and the Pt/CB catalyst layers. The whole cathode thickness after hot press was at *ca.* 150μm.

2.2. Li-Air Assembly. The HyLAB assembled in this work consists of a sealed anode made by MaxPower Inc. (a pouch half-cell) [15] and an air-breathing cathode described above. Fig. 1 shows a schematic structure of the Li-air cells. The effective area of electrode reported here is 10 cm^2. In order to prevent electric shorts between the carbon paper and the Li anode pouch cell, a Teflon® tape was used to cover the rim of the pouch. The advantage of using a Teflon tape is that its hydrophobic property prevents the aqueous electrolyte solution from leaking. The catholyte in our study of cell discharge is

a pure 1.0 M H_2SO_4 to start with. The volume of the acid was 5.0 mL, to fill up the recess in the pouch in the cathode side.

2.3. Li-Air Cell Test. Tests of the HyLABs were performed in an ambient environment and at room temperature (25 ºC). An Arbin battery test station (GT2000) connecting to a computer installed with the Arbin Data Pro software was used in the charge-discharge and data collection. For each cell tested, the discharge current density was chosen as 0.01 mA/cm^2, 0.1 mA/cm^2, 0.2 mA/cm^2, 0.5 mA/cm^2, or 1.0 mA/cm^2. For long-term discharge and charge experiments, a current density of 0.2 mA/cm^2 was used.

3. RESULTS AND DISCUSSION

The thickness of 10 mg of CNFs filtered onto the filter membrane produced a transition layer of 30-35 μm in thickness and 10 mg of Pt-loaded carbon produced 20-25 μm active layer, which were confirmed by their cross-sections through SEM. The cross-section and surface morphology of typical air-breathing cathodes were characterized by SEM and shown in Fig. 2. In either case of Pt/CNT or Pt/CB, the total thickness of the buckypaper is about 50μm after hot press, as can be seen from Fig. 2. Similar to proton exchange membrane (PEM) fuel cell electrode preparation, a hot press procedure was needed in order to yield a strong interaction between the carbon paper backing and catalyst layers. It is inevitable that CB particulate structure (with low aspect ratio particulates) was constricted in each direction under high pressure, and this leads to

compactness, low porosity, as well as formation of lots of dead-ended channels in this process. However, due to the fibrous structure of CNTs. They were compressed only along the direction of pressure (perpendicular to the electrode surface) in the hot press process. The CNTs are intertwined in the horizontal directions (in plane), forming open channels for air diffusion. Consequently, Pt/CNT formed an open buckypaper layer (see Fig. 2 (A) and (B)) on the transition layer and remained porous after hot press, but Pt/CB formed a compact layer with less porous channels after hot press (see Fig. 2 (C) and (D)). The surface morphologies of these cathodes are very much different in the catalyst layers, as can be seen from their SEM images. Consequently, their porous structures have direct effect on the Li-air cell performance as shown below

For acidic electrolytes, the calculated discharge OCV is 4.274 V at 25 ºC, assuming a 4 electron reaction for the reduction of oxygen [15]. The cells exhibited OCVs in the range of 3.95 – 4.02 V, depending on the different carbon materials and electrocatalysts. Therefore, the difference between the theoretical and actual OCVs is small. The result was attributed to the better ORR activity in H_2SO_4 because of higher concentration of protons in the H_2SO_4 solution, despite that the air cathode used a low loading Pt catalyst (5 wt.%). Geometric loading is of Pt in the cathode is calculated to be only 0.05 mg/cm^2 (electrode area), but it was found good enough to produce a current flow comparable to that of non-aqueous electrolyte cells. It noted that this loading is much less than the long term (for the year of 2015) DOE target (0.125 mg/cm^2) for noble metal loading in PEM fuel cells.

The HyLAB cell potential dropped from 3.72 V discharging at 0.1 mA/cm^2 to 3.43 V at 0.5 mA/cm^2 for the buckypaper cathode (Pt/CNTs), as shown in Fig. 3. The polarization of the cell was mainly due to the cell resistance derived from contact resistance at the anode side, especially the one between the aprotic electrolyte and the LiCGC membrane [13, 19]. At low discharge currents, the cell performance (potential) was about the same as the one based on the cathode made with Pt/CB; the cell potentials for both cells were around 3.72 V at 0.1 mA/cm^2 and 3.58V at 0.2 mA/cm^2. However, as the discharge current density was increased to 0.5 mA/cm^2, the cell potential with Pt/CNTs surpassed that with Pt/CB (3.27 V), with a difference of 160 mV. When the current density went up to 1.0 mA/cm^2, the potential difference became further apart at 220 mV, with 3.21 V for Pt/CNTs and 2.99 V for Pt/CB, demonstrating the advantage of CNT electrode structures.

At high discharging current densities, air diffusion would become a limiting factor to the cell performance. This was especially evident in the HyLAB cell when the cathode with Pt/CB was discharged at 1.0 mA/cm^2. It was observed that the potential of this cell was dropping along with discharge time (~10 hours, see Fig. 3), as a result of diffusion limitation in the less porous CB layer [20-23]. In contrast, the cell with Pt/CNTs showed an even increased potential level during the discharge cycle. Although this increase needs further study to understand, the result demonstrated that the fibrous CNTs as catalyst support are superior to the granular CB. It is noted that when the cells were stopped for discharging, their potentials reached back and rose to the OCVs. This discharge behavior

was also observed in other aqueous electrolyte based LABs [14, 16, 24].

The results shown in Fig. 4 were obtained from a long-time cell discharge at 0.2 mA/cm^2 with an excess amount of sulfuric acid, *i.e.*, 5 mL of 1.0 M H_2SO_4 (0.49 g acid in weight). The cell potential was stable for a period of 49.5 hours with a cell potential as high as 3.534 V, which gives 202 mAh/g in specific capacity, based on the mass of sulfuric acid. This is comparable to the previously reported numbers for other acids [13, 16]. The utilization of the sulfuric acid was 36.9% at 49.5 hours. The specific energy at this point calculated from the discharge capacity and cell potential is 717 Wh/kg.

After the *ca.* 50 h discharge, the cell potential starts to decrease slowly. When the cut off potential was set to 3.15 V, the cell has a total discharge time of 75 hours. The utilization of acid was at 55.6%, which is about the same as the previously reported 56% acetic acid utilization of Zhang *et al.* [13]. At this point, however, the cell produced a specific capacity of 306 mAh/g and a specific energy of 1067 Wh/kg. These numbers are much higher than those previously reported based on different acids and cathodes [13, 16]. According to a recent review [25], a Li-air cell specific energy at 1000 Wh/kg would enable a driving range of 380 miles, a practical distance approaching that of gasoline powered cars. Given that the utilization of the acid in our cell is just above half, further improvement in performance of the HyLAB cell is very likely and could lead to reaching the goal for long range driving with a single charge.

It is noted that the corrosion of lithium-ion conducting solid electrolyte separator is inevitable in some acidic media [19, 26, 27]. In sulfuric acid, our XRD results showed

that there is a small difference between the pristine ceramic membrane and that after long term (75 hours) discharge (in Fig. 5). Two peaks at $2\theta \approx 17.2°$ and 23.2° appeared after discharge. Compared to the major peaks, the intensity of these new peaks are very small, indicative of that the chemical changes are small. According to a most recent study [28], the protons only adsorb on the ceramic membrane surface and do not diffuse into the bulk, and therefore, only the surface of the membrane is modified. Our observation seems consistent with that conclusion. However, more studies are being conducted for the ceramic membrane stability in sulfuric acid and will be reported in a future paper.

According to a previous study [29], the effect of Li ions on the ORR activity cannot be ignored. The increase of Li ion concentration in the catholyte during a long-term discharging obviously decreased the oxygen diffusion rate in the acid electrolyte, leading to lower ORR rate [29]. During discharge the production of Li ions and conversion of the electrolyte from sulfuric acid to lithium sulfate will shrink the volume of the aqueous electrolyte. It is inevitable that the hydrophobic Teflon tape covered rim of the pouch produced a gap between the catholyte and the cathode surface. Water vapor can form in the gap and escape through the porous cathode carbon paper, which would further reduce the contact area between the electrolyte and the cathode. It was found that about 10-15% electrode area was no longer wetted by the electrolyte after the long-duration (75 h) discharge. Consequently, the decrease in performance was largely attributed to this active area reduction. Indeed, we have confirmed that this reduced performance can be recovered by refilling the cell with new sulfuric acid solution, as shown in Fig. 3. This

result further confirms that the LiCGC was stable during the period of discharge experiments and did not degrade cell performance notably; otherwise, refilling the electrolyte would not recover the performance if it were to do with the LiCGC membrane.

Cycling results of the cell at 0.2 mA/cm^2 are presented in Fig. 6(A). The durations for charge and discharge of the cell were 1.5 hours in each cycle, and there were 9 cycles with a total of 27 h. The potential difference between the discharge and charge potentials at the beginning was about 1.25 V, and it increased slowly to 1.45 V after 5 cycles and to 1.59 V at the end of the cycling test. While Pt is good for ORR, its surface oxide formation at high overpotentials does not facilitate oxygen evolution reaction (OER), which is the reverse reaction of ORR occurred during recharge. It was reported that Pt in sulfuric acid would have a 210 mV overpotential at the first 3 h [30] and up to 970 mV for a longer term [31]. The overpotentials observed in this study fall in this reasonable range. It is also noted that the Li ions generated during discharge produced an electrolyte with ever increasing Li ion concentrations. The cations could further complicate the OER on the Pt, which would need a separate study. In the later cycles, the potential difference increased along with each cycle, possibly due to that the Pt catalyst was slowly but incrementally oxidized during the OER process [32]. Such high overpotentials, however, can be reduced by suing an effective OER catalyst, which is under study in our lab and will be reported in the future.

Further discharge-charge experiments are presented in Fig. 6(B). Although we demonstrated that the ceramic membrane does not degrade much, we nevertheless used a diluted 0.01 M sulfuric acid in a new cell to investigate rechargeability so that the LiCGC membrane would not be a factor in affecting the cell performance. Diluted acid would also reduce oxidation rate of the Pt catalyst. In order to keep constant capacity in long-term discharge, the charge capacity was cut off at 306 mAh/g. Again, the acid has a utility percentage of *ca.* 56% at the capacity of 306 mAh/g. It is interesting to note that the concentration of sulfuric acid did not notably impact the cell performance, indicating the good ORR activity in sulfuric acid. The cell was discharge/charged 10 times in the same manner. The presented is the performance of charge/discharge capacity vs. cell potential in cycle 1, 2, 5, and 10. The potential difference between the discharge and charge potentials at the beginning was about 0.89 V, and it increased slowly to 1.19 V after 5 cycles and further to 1.37 V at the end of the cycling test, which are smaller than those in the more concentrated acids, as expected.

4. CONCLUSIONS

In summary, sulfuric acid is demonstrated to be a viable catholyte in a HyLAB cell that has a large electrode area at 10 cm^2. A low loading 5 wt.% Pt as electrocatalyst can produce a high battery capacity and specific energy in the rechargeable Li-air cell. It was found that cathode catalyst layer made with Pt/CNT buckpaper is better than that made

with Pt/CB. The better performance was attributed to the more open porous structures formed in fibrous CNTs. At a cut-off voltage of 3.15 V, the HyLAB cells achieved a discharge capacity of 306 mAh/g and a specific energy of 1067 Wh/kg at 0.2 mA/cm^2 based on the total weight of acid in the cell. Increased overpotentials during charge/discharge were observed in cycling. It is suggested that a bifunctional electrocatalyst is needed for better rechargeability.

5. ACKNOWLEDGMENTS

Financial support by the U.S. Department of Energy ARPA-E grant DEAR0000066 is gratefully acknowledged. We thank MaxPower, Inc. to supply the sealed anodes for our tests and NanoLab, Inc. to supply the carbon nanotubes. We thank Dr. Mark Salomon and Dr. David Chua for useful discussions.

REFERENCES

[1] P.G. Bruce, S.A. Freunberger, L.J. Hardwick and J.-M. Tarascon, Nat. Mater., 2012, 11, 19-29.

[2] G. Girishkumar, B. McCloskey, A.C. Luntz, S. Swanson and W. Wilcke, J. Phys. Chem. Lett., 2010, 1, 2193-2203.

[3] K.M. Abraham and Z. Jiang, J. Electrochem. Soc., 1996, 143, 1-5.

[4] J. Read, J. Electrochem. Soc., 2002, 149, A1190-A1195.

[5] J. Read, K. Mutolo, M. Ervin, W. Behl, J. Wolfenstine, A. Driedger and D. Foster,

J. Electrochem. Soc., 2003, 150, A1351-A1356.

[6] J. Read, J. Electrochem. Soc., 2006, 153, A96-A100.

[7] W. Xu, J. Xiao, D. Wang, J. Zhang and J.-G. Zhang, Electrochem. Solid-State Lett., 2010,13, A48-A51.

[8] W. Xu, J. Xiao, D. Wang, J. Zhang and J.-G. Zhang, J. Electrochem. Soc., 2010, 157, A219-A224.

[9] S.S. Zhang, D. Foster and J. Read, J. Power Sources, 2010, 195, 1235-1240.

[10] S.S. Zhang, K. Xu and J. Read, J. Power Sources, 2011, 196, 3906-3910.

[11] S.J. Visco, Protected Li Anodes for use in Conventional & Aggressive Electrolytes, Advanced Anode Workshop, Berkeley, CA, 2004.

[12] T. Zhang, N. Imanishi, S. Hasegawa, A. Hirano, J. Xie, Y. Takeda, O. Yamamoto and N. Sammes, J. Electrochem. Soc., 2008, 155, A965-A969.

[13] T. Zhang, N. Imanishi, Y. Shimonishi, A. Hirano, Y. Takeda, O. Yamamoto and N. Sammes, Chem. Commun., 2010, 46, 1661-1663.

[14] E. Yoo and H. Zhou, ACS Nano, 2011, 5, 3020-3026.

[15] I. Kowalczk, J. Read and M. Salomon, Pure Appl. Chem., 2007, 79, 851-860.

[16] L. Li, X. Zhao and A. Manthiram, Electrochem. Commun., 2012, 14, 78-81.

[17] O. Crowther, B. Meyer, M. Morgan and M. Salomon, J. Power Sources, 2011,196, 1498-1502.

[18] Y. Xing, J. Phys. Chem. B, 2004, 108, 19255-19259.

[19] Y. Shimonishi, T. Zhang, P. Johnson, N. Imanishi, A. Hirano, Y. Takeda, O. Yamamoto and N. Sammes, J. Power Sources, 2010, 195, 6187-6191.

[20] J. Newman and W. Tiedemann, AIChE Journal, 1975, 21, 25-41.

[21] E. Antolini, R.R. Passos and E.A. Ticianelli, J. Appl. Electrochem., 2002, 32, 383-388.

[22] H.-S. Chu, C. Yeh and F. Chen, J. Power Sources, 2003, 123, 1-9.

[23] A. Ermete, Appl. Catal. B: Environmental, 2009, 88, 1-24.

[24] S.J. Visco, E. Nimon, B. Katz, L.D. Jonghe and M.Y. Chu, Proc. The 210th Electrochemical Society Meeting, Cancun, Mexico, 2006.

[25] J. Christensen, P. Albertus, R.S. Sanchez-Carrera, T. Lohmann, B. Kozinsky, R. Liedtke, J. Ahmed and A. Kojic, J. Electrochem. Soc., 2012, 159, R1-R30.

[26] S. Hasegawa, N. Imanishi, T. Zhang, J. Xie, A. Hirano, Y. Takeda and O. Yamamoto, J. Power Sources, 2009, 189, 371-377.

[27] J. Wolfenstine, J. Mater. Sci., 2010, 45, 3954-3956.

[28] F. Ding, W. Xu, Y. Shao, X. Chen, Z. Wang, F. Gao, X. Liu and J.-G. Zhang, J. Power Sources, 2012, 214, 292-297.

[29] H. Liu and Y. Xing, Electrochem. Commun., 2011, 13, 646-649.

[30] J.O.M. Bockris and A.K.M.S. Huq, Proceedings of the Royal Society of London A: Mathematical and Physical Science, 1956, 237, 277-296.

[31] D. Gilroy, J. Electroanal. Chem. Interfacial Electrochem., 1977, 83, 329-339.

[32] A. Damjanovic and B. Jovanovic, J. Electrochem. Soc., 1976, 123, 374-381.

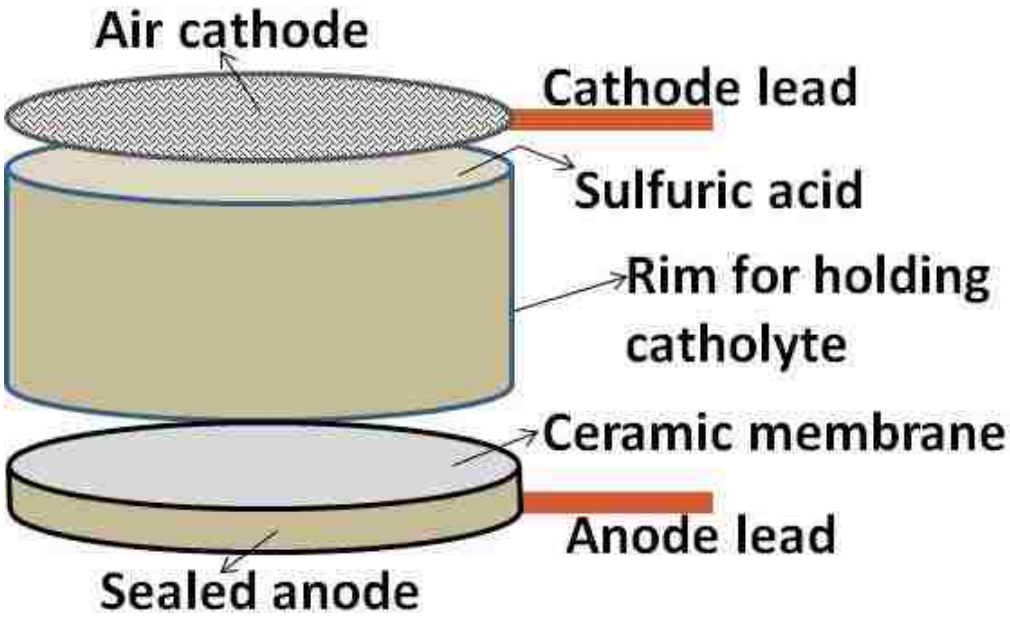

Fig. 1 Schematic diagram of the HyLAB with sulfuric acid catholyte. Sealed anode contains a Li foil, an aprotic buffer, and the top ceramic membrane.

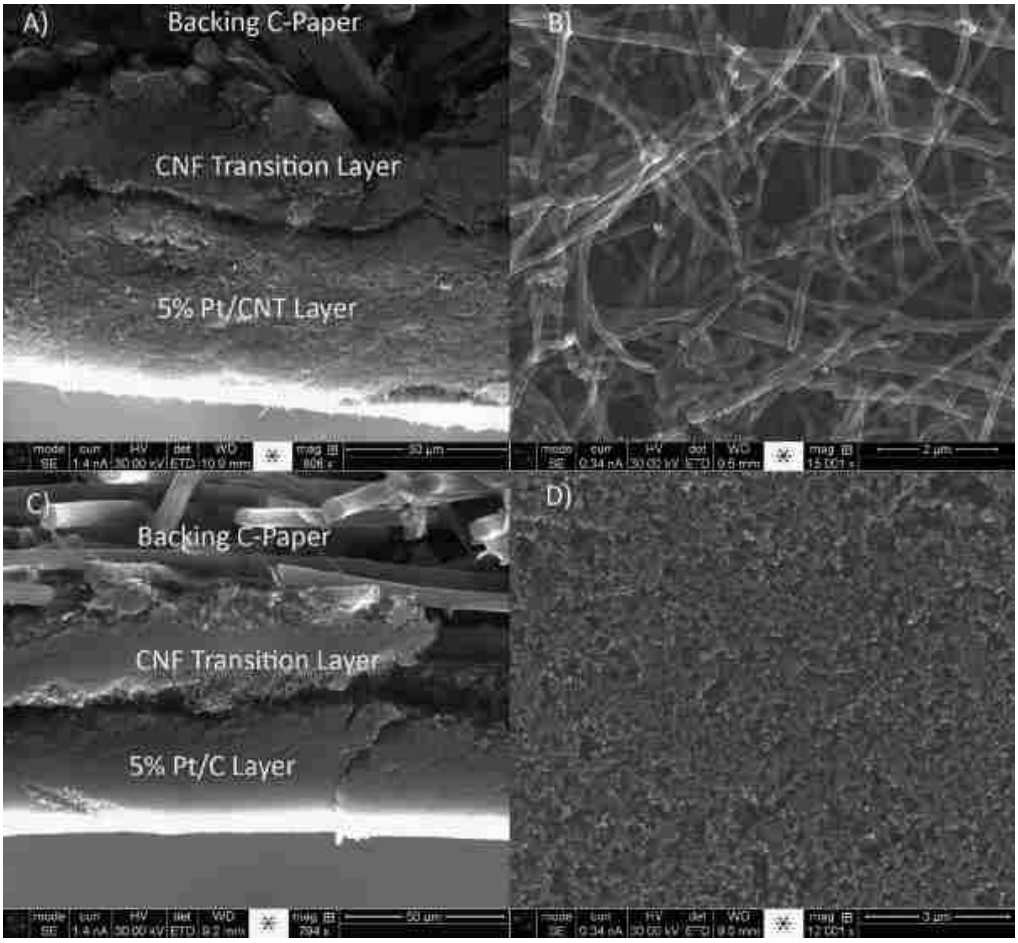

Fig. 2 SEM images of (A) a cross-section of 5 wt.% Pt/CNT buckypaper layer on a CNF transition layer, (B) surface morphology of (A), (C) a cross-section of 5 wt.% Pt/CB on a CNF transition layer, and (D) surface morphology of (C).

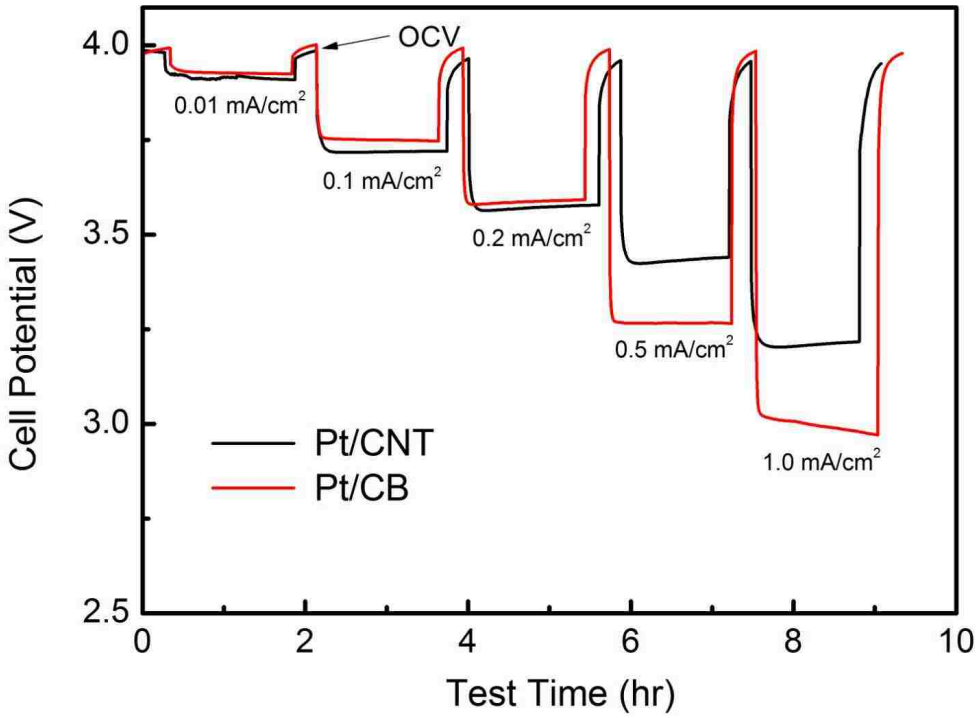

Fig. 3 10 cm^2 battery performance at different discharge current densities. The two cathodes were based on 5 wt.% Pt/CB catalyst and 5 wt.% Pt/CNT catalyst. Both cells used 1.0 M H_2SO_4 as catholyte.

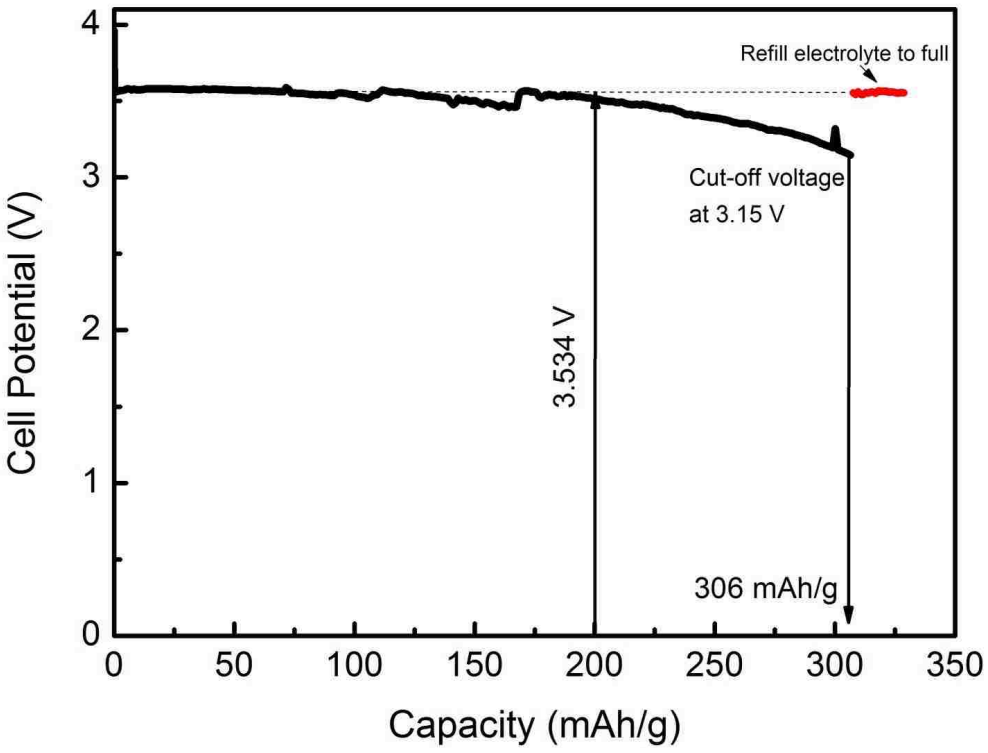

Fig. 4 Constant current density discharge (0.2 mA/cm^2) of the 10 cm^2 Li-air cell with 5 wt.% Pt/CNT cathode using 1.0 M H_2SO_4 as catholyte. Refill of fresh electrolyte in the cell recovers the cell performance.

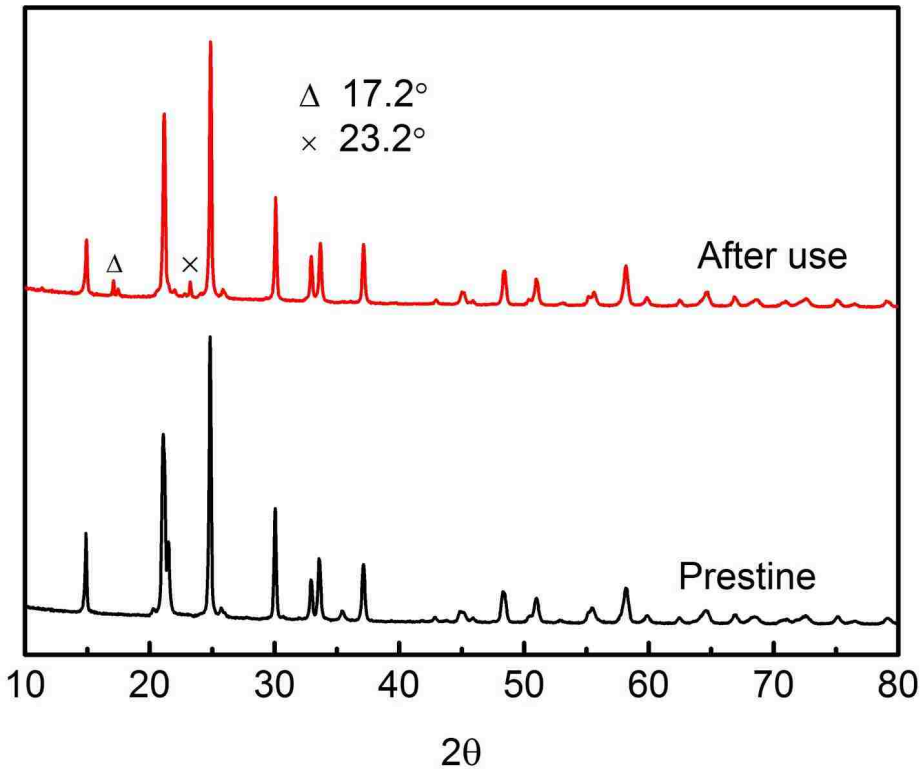

Fig. 5 XRD patterns of LICGC membranes in pristine state and after use.

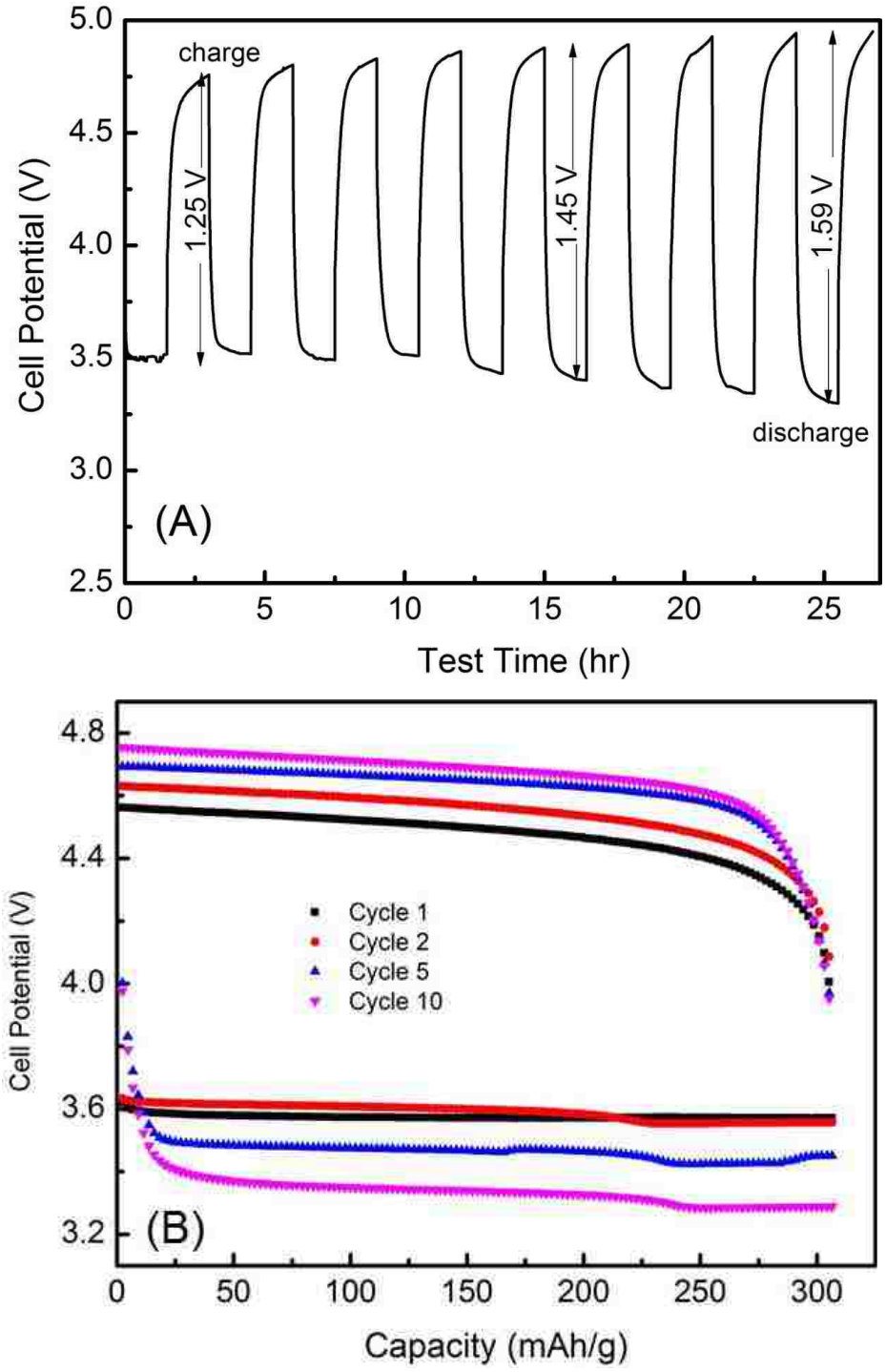

Fig. 6 Charge–discharge performance of the 10 cm^2 Li-air cell with 5 wt.% Pt/CNT cathode at 0.2 mA/cm^2 at 25 °C and in ambient air, using H_2SO_4 as catholyte with concentrations of (A) 1.0 M and (B) 0.01 M.

IV. INCREASING ROUND TRIP EFFICIENCY OF HYBRID LI-AIR BATTERY WITH BIFUNCTIONAL CATALYSTS

Kan Huang[1], Yunfeng Li[2], Yangchuan Xing[2a]

[1]Department of Chemical and Biological Engineering, Missouri University of Science and Technology, Rolla, MO, 65409
[2]Department of Chemical Engineering, University of Missouri at Columbia, Columbia, MO, 65211
[a]Address all correspondence to this author. Email: xingy@missouri.edu

ABSTRACT

We previously showed that Pt as cathode catalyst has a large overpotential during charge in rechargeable hybrid Li-air battery with sulfuric acid catholyte. This article demonstrates that a bifunctional catalyst composed of Pt and IrO_2 supported on carbon nanotubes can address this problem. The specially designed and synthesized bifunctional catalyst showed significant overpotential reduction and achieved a round trip energy efficiency of 81% after 10 cycles, much higher than those achieved in aprotic Li-O_2 batteries (*ca.* 65%). Thy hybrid Li-air battery was discharged and recharged for 20 cycles at 0.2 mA/cm^2, showing a fairly stable cell performance. A specific capacity of 306 mAh/g and specific energy of 1110 Wh/kg were obtained for the hybrid Li-battery in terms of acid weight.

1. INTRODUCTION

Lithium-air battery (LAB) has attracted intensive attention due to their high theoretical energy densities, comparable to that of gasoline [1-3]. Since Abraham and Jiang [4] proposed the rechargeable non-aqueous lithium-oxygen battery, major efforts have been paid on aprotic lithium-air battery [5-7]. A major problem with aprotic LAB is that the insoluble discharge products, lithium oxides, deposit in the porous cathode and block the further oxygen intake. Consequently, discharge ends quickly when the pores are clogged. The insulating nature of lithium oxides also lead to sudden drop of output voltage, increase of charge potential, and thus loss of capacity [1]. In addition, the contamination of moisture in the electrolyte can degrade lithium metal, causing the problems of self-charging and circuit shortening [8, 9].

The development of an aqueous version of LAB has opened an alternative way to the aprotic LAB [10]. The state-of-the-art of this LAB involves using hybrid electrolytes including a Li-ion conducting, but electronically insulating membrane, such as LISICON-type glass, that is impermeable to liquid electrolytes and can protect the Li metal from direct contact with aqueous solution [2]. Such hybrid electrolyte LABs (HyLABs) have been demonstrated in aqueous neutral [11], acidic [12, 13] and alkaline electrolytes [14, 15]. Water is reduced in neutral or basic electrolytes when batteries were discharged, which follows $O_2 + 2H_2O + 4e^- \rightarrow 4OH^-$ (E^o=0.4 V *vs.* RHE), yielding a theoretical potential at 3.43 V. In acidic electrolytes, oxygen is reduced through $O_2 + 4H^+ + 4e^- \rightarrow 2H_2O$ (E^o=1.23 V *vs.* RHE) which produces a 4.27 V theoretical potential.

To date, Pt is still the most active catalyst for oxygen reduction reaction (ORR) [16-18], even though metal free N-doped grapheme [19], manganese oxides [15] and perovskite oxides [20] were reported to exhibit some ORR activities. Pt is most suitable for use in acids for stability, and there are several studies reporting utilizing Pt as ORR catalyst in acid based LAB. Zhang *et al.* [12] reported using Pt mesh as cathode catalyst in acetic acid, demonstrating 15 charge-discharge cycles. Li *et al.* [21] used 40 wt.% Pt/C in phosphoric acid electrolyte and observed a potential difference increasing from 1.0 to 1.3 V after 20 cycles. In order to reverse a discharged LAB to its original charged state, an extra overpotential, usually positive 200-300 mV to the standard E^{o}=1.23 V, is required to electrolyze water for OER [22]. Under this overpotenial range, Pt is oxidized to form oxidized film and loss its catalytic ability [23, 24]. Our previous work [25] has demonstrated sulfuric acid as catholyte in a HyLAB. The cathode catalyst was also Pt but supported on carbon nanotubes (CNTs) with ultralow Pt loading at only 5×10^{-5} g/cm^2. While a discharge specific energy achieved was over 1000 Wh/kg, the round trip efficiency was low due to the large overpotential gap between charge and discharge. It was concluded that a bifunctional electrocatalyst is needed to reduce overpotential for OER.

Iridium oxide (IrO_2) has been found to be an active and stable OER catalyst at high current densities [26, 27]. Pt/IrO_2 as a bifunctional oxygen catalyst has been used in regenerative fuel cells [28-30], in which Pt serve for ORR and IrO_2 for OER. Here, we report a study on developing a CNT-supported Pt/IrO_2 bifunctional oxygen catalyst for

the HyLAB. It was shown that the round trip efficiency can be much improved by using the bifunctional oxygen catalyst.

2. EXPERIMENTAL

2.1. Catalysts Preparation. CNTs (Nano Lab, 50±15 nm) were treated with 3:1 H_2SO_4/HNO_3 (volume ratio) in an ultrasonic bath at 60 °C for 2 hours for surface functionalization [31], followed by filtration and thorough washing with deionized water. 10 mg of the functionalized CNTs were then dispersed in 10 ml ethylene glycol plus 5 ml de-ionized water with the aid of sonication and stirring. Pre-determined amount of 0.01 M K_3IrCl_6 (Alfa Aesar) salt solution was pipetted into the above suspension and it was stirred under reflux conditions for reactions for 2 hours. The iridium salt was reduced to metallic Ir to form Ir nanoparticles deposited on the CNTs (Ir/CNTs), which were separated out with a centrifuge. The product was thoroughly washed and dried at 80 °C in a vacuum oven overnight. It was then annealed in air at 400 °C for 2 hours to oxidize the metallic Ir nanoparticles into crystalline iridium oxide (IrO_2), leading to a final 10 wt.% IrO_2 loading on the CNTs. That catalyst was further made into a suspension, and deposition of 5 wt.% Pt on IrO_2/CNTs was achieved by a polyol process reported previously [32] to produce bifunctional catalyst Pt/IrO_2/CNTs. Using bare CNTs, Pt was also deposited on CNTs to make Pt/CNTs without iridium oxides.

2.2. Catalysts Characterization. Morphologies of the catalysts were examined by transmission electron microscope (TEM) (FEI Tecnai F20). The crystalline phase of the catalysts was analyzed by X-ray diffraction (XRD) equipped with Cu K (α) and the XRD data were collected with a Philips X-Pert Diffractometer over an angle rang of 2θ = 10 - 90° at a scanning rate of 0.026° s^{-1}.

2.3. Electrochemical Testing. All electrochemical experiments were performed with an Electrochemical Workstation (Bioanalytical Sciences, BAS 100). The working electrode was a glassy carbon rotating disk electrode (RDE) with a disk diameter at 5 mm (Gamry RDE 710). A Pt wire was used as the counter electrode and saturated Ag/AgCl as a reference electrode. The catalyst powder was dispersed in deionized water by sonication for 20 min to form 1 mg/mL catalyst suspension. 20 μL of the suspension was pipetted onto the disk and dried in air. About 5 μL Nafion solution (0.05 wt.%, Alfa Aesar) was then put on top of the catalyst. Cyclic voltammetry (CV) and OER measurements were carried out in N_2 purged 1.0 M H_2SO_4 at potential range of 0-1.5 V and 0.8-1.6 V (*vs.* RHE), respectively. ORR measurement was taken in an O_2-saturared 1.0 M H_2SO_4 at rotating speed of 1600 rpm between 0.2-1.0 V (*vs.* RHE). To study the durability of Pt/IrO_2/CNTs, CV was conducted in N_2-bubbled 1.0 M H_2SO_4 in the potential range between 0.6 and 1.5 V (*vs.* RHE) up to 1000 cycles. The initial and final CV and ORR behaviors were recorded. For comparison, Pt/CNTs catalyst was also tested under the same cycling conditions. Current densities are calculated based on the total catalyst weight normalized to mA/mg.

2.4. Li-Air Cell Test. Details of air cathode preparation and cell assembly were reported in our previous work [25]. Tests of the cell were performed in an ambient environment and at room temperature. An Arbin battery test station (GT2000) was used for charge-discharge data collection. 0.01 mA/cm^2, 0.2 mA/cm^2, 0.5 mA/cm^2, and 1.0 mA/cm^2 discharge current densities were chosen for cell test in 1.0 M sulfuric acid. For long-term discharge and charge experiments, 0.2 mA/cm^2 current density was used. In this work, Pt/CNTs and Pt/IrO_2/CNTs were compared to demonstrate the advantage of the bifunctional catalyst.

3. RESULTS AND DISCUSSION

Crystalline information of the catalyst was obtained from X-ray diffraction. XRD patterns of IrO_2/CNTs and Pt/IrO_2/CNTs were shown in Figure 1. The absence of Ir metal diffraction and the presence of characteristic peaks belonging to rutile IrO_2 [22] in IrO_2/CNTs indicate complete transformation of metallic Ir to crystalline IrO_2. After Pt deposition, the crystalline form of IrO_2 remains unchanged in the catalyst. The peak at *ca.* 26° is graphite, from the graphitic structure of the CNT support [32].

Figure 2(A) shows a TEM image of the IrO_2/CNTs. It can be seen that the nanotube surface was uniformly covered with IrO_2 particles, and despite some in agglomerates there are no apparent sintering so that their nanoparticulate entity is retained after transformation. The two-step procedure was designed to uniformly deposit Ir on the

CNTs first and then convert it to IrO_2. This method can guarantee the uniform dispersion of IrO_2 with minimum aggregation and maximize the utilization of the active oxide surface.

The mean size of IrO_2 was measured to be 3.6±0.5 nm from image analysis. A high magnification image in Figure 2(A) shows lattice spacing of the graphitic layer of CNTs and rutile IrO_2 at 0.34 and 0.26 nm, respectively. The former is characteristic of basal planes in graphite, and the latter is characteristic of the (101) planes in rutile IrO_2, which also showed up in the XRD patterns as seen in Figure 1. After deposition of Pt on IrO_2/CNTs, the morphology of IrO_2 does not shown changes, as can be gauged from Figure 2(B). XRD patterns (see Figure 1) show that Pt now appears in the catalyst. Carefully examining the surface of the catalyst Pt/IrO_2/CNTs, there exist many round darker black nanoparticles. These nanoparticles are believed to be Pt since stronger lattice diffraction occurs in metals than in oxide, giving contrast. These nanoparticles are measured to have a size of 2.3±0.2 nm.

The prepared catalysts were put under electrochemical tests in a three-electrode cell. The CV plots of Pt/CNTs, IrO_2/CNTs and Pt/IrO_2/CNTs were presented in Figure 3(A). The anodic peaks at 0.66 V and cathodic peaks at 0.58 V were associated with redox of surface oxide group, which have been found in acid-treated CNTs [31]. The anodic current occurred beyond 1.4 V (*vs.* RHE) was assigned as to water oxidation currents [22]. IrO_2 was found to be electrochemical inert in the potential range at 0-1.4V and have negligible contribution to the electrochemical surface area (ESA), while Pt/IrO_2/CNTs

exhibits the typical peaks belonging to hydrogen ad/de-sorption on the Pt surface [32]. The ESA of Pt in the catalyst was obtained using the methods commonly accepted [32, 33]. The ESA in Pt/IrO_2/CNTs is obtained to be 905.7 cm^2/mg_{Pt}, close to the 996.2 cm^2/mg_{Pt} in Pt/CNTs, indicating that Pt active surface area is large in both catalysts.

The ORR activities of IrO_2/CNT, Pt/CNT and Pt/IrO_2/CNTs were plotted in Figure 3(B). IrO_2/CNTs exhibits negligible catalytic activity and has no contribution towards ORR. Meanwhile, Pt/IrO_2/CNTs showed a similar ORR performance as Pt/CNTs with the same Pt loading, suggesting that IrO_2 has not affected Pt for catalyzing ORR. Linear sweep voltammetry (LSV) was conducted to record the OER performances of the three different catalysts. As shown in Figure 3(C), Pt has some catalytic activity towards OER (all OER currents were capacitance-corrected [22], see Figure S1), but is significantly lower when compared to that from IrO_2. The mass activity of IrO_2/CNTs at overpotential η = 0.25 V can reach 6 A/g_{IrO2} without Ohmic correction, which are comparable or better than 5 A/g_{IrO2} and 3 A/g_{IrO2} reported by Rasten *et al.* [34] and Lee *et al.* [22], respectively, at the same overpotential.

We found that by incorporating Pt with IrO_2/CNTs, a significantly higher current density can be achieved than IrO_2/CNTs alone (96 $mA/mg_{catal.}$ *vs.* 56 $mA/mg_{catal.}$ at 1.6 V), which is also higher than the sum of IrO_2/CNTs and Pt/CNTs, indicative of that there is a possible synergistic effect between Pt and the oxide IrO_2 for OER. A similar enhancement was observed by Yao *et al.* who used Pt supported on pure IrO_2 [29]. It was argued that the downshift of *d*-band center of Pt on Pt/IrO_2 weakened the O_{ads} bound to

the catalytic surface, favoring water dissociation to form oxygen. It decreases the coverage of O_2/O_{ads} on catalyst surface and thus, increases the available active sites.

To gain more information about the stability of the catalyst $Pt/IrO_2/CNTs$, accelerated cycling test was performed by applying 1000 potential cycles from 0.6-1.5 V (*vs.* RHE) in N_2-bubbled 1.0 M H_2SO_4. As shown in Figure 4(A), Pt oin this catalyst only suffered very small surface area loss, verified by negligible change in H ad/de-sorption region of 0.05-0.4 V before and after the potential cycling tests. In contrast, ESA of Pt/CNTs suffered a much larger loss after 1000 cycles, from 996 to 230 cm^2/mg_{Pt}, leading to a severe degradation of ORR performances (see Figure S2). Figure 4(B) showed that the ORR half-wave potential shifted 40 mV negatively, indicative of an ORR activity loss, but it's much smaller than that of the Pt/CNT catalyst (see Figure S2). We attributed the loss of the Pt to its easy degradation on carbon support due to weak interaction between the metal and carbon. We have previously shown that Pt severely degrades on carbon black (Vulcan-XC 72) in sulfuric acid, but it can be significantly improved by supporting the Pt on a conducting nanocoating of titanium suboxide on the CNTs [35]. The fact that oxide IrO_2 is involved may have similarly improved the stability of Pt, although perhaps to lesser degree since iridium oxide in this case is not a continuous film and some Pt is in contract with carbon. Decrease in ORR activity is also attributed to the formation of a thin Pt-oxide layer at high potentials. Reier *et al.* [36] observed electrochemical activity of Pt nanoparticle surface despite deactivation of Pt by forming an oxide layer, which is believed to be responsible for the observed ORR

activity in this work.

In the OER region (1.4-1.6 V), the CVs showed some changes of the Pt/IrO_2/CNTs after cycling. It was determined that the OER current density decreased from 105 to 86 mA/mg $_{catal.}$ at 1.6 V (see Figure 4(C)). Kötz *et al.* [37] proposed a mechanism for OER on iridium oxide. Oxygen is split off from water on IrO_3 with Ir in the hexavalent state, which was formed by two consecutive deprotonation steps from $IrO(OH)_2$. Meanwhile, IrO_3 may corrode into the electrolyte as IrO_4^{2-} ion and lead to direct the OER activity loss. Formation of poorly conductive and catalytically inactive Pt oxide species may also contribute to the loss of OER activity [36]. Nevertheless, the results showed a relatively stable performance of the bifunctional catalyst in sulfuric acid electrolyte.

Figure 5 presents the discharge of a full Li-air cell using Pt/CNTs or Pt/IrO_2/CNTs as catalysts in the cathode at different discharge current densities. The operation potentials dropped from 3.72 to 3.21 V with increasing current densities from 0.1 to 1.0 mA/cm^2, and this polarization was mainly due to the internal resistance at the anode side [12, 25]. Under 0.1~0.5 mA/cm^2 discharge current densities, the cell performance with Pt/CNTs or Pt/IrO_2/CNTs is very close as seen from Figure 5, indicative of that there are no significant catalytic differences between Pt/CNTs and Pt/IrO_2/CNTs towards ORR. This observation supports the findings that IrO_2 has negligible contribution to ORR. However, at a higher current density (*e.g.*, 1.0 mA/cm^2), Pt/CNTs yielded a slightly better performance than Pt/IrO_2/CNTs. Similar findings were reported previously, showing that Pt black is better than Pt/IrO_x in regenerative fuel cells [29, 38]. As shown in Figure 2(B),

some Pt nanoparticles were found to be on the IrO_2 surface rather than directly deposited on the CNTs. We assume that some electron conducting path maybe hindered by the less conductive IrO_2 agglomerates because the ohmic resistance of IrO_2 is nearly five times larger than that of Pt [29]. Under a high current density, the inefficiency of electron transport could result in a voltage loss.

Cycling results of the Li-air cell in Pt/CNTs and Pt/IrO_2/CNTs at 0.2 mA/cm^2 are presented in Figure 6. The duration for charge and discharge was set at 1.5 hours each, and the cell was cycled for 21 hours. Using Pt/CNTs as the cathode catalyst, the potential gap between the charge and discharge was about 1.25 V initially, and it slowly increased to 1.45 V after 6 cycles, as shown in Figure 6(A). A loss of the discharge potential was recorded from 3.50 to 3.36 V, indicative of that a higher overpotential was induced in order to initiate the ORR, attributed to surface oxide formation on Pt. It is well known that Pt is an excellent electrocatalyst for ORR but not for OER, due to its high oxygen evolution ovepotential and formation of a stable surface oxide layer [23]. The charge process requires a much higher potential to dissociate water into oxygen. The potential of the first recharge reached 4.75 V (*vs.* Li^+/Li), corresponding to OER potential of 1.7 V (*vs.* RHE). Jerkiewicz *et al.* [24] suggested that Pt^{2+}-O^{2-} is formed above 1.15 V (*vs.* RHE), and the oxide film is not reduced until the potentials are near the H potential range [23]. The loss of activity of Pt is again attributed mainly to the formation of the surface oxide.

As discussed above, intensive scanning of Pt/CNTs in a high potential range has led to a dramatic ESA and ORR loss, thus the passivation of Pt may be one of the major factors responsible for the decrease of cell performance. It was found that the charge potential gradually increased in the first charge round, and this trend became more evident in the later charge steps. On the contrary, a decreasing tendency in discharge potential was found in the second and following discharge cycles. All those observations suggested that utilizing single Pt as cathode catalyst has its limitations and could not sustain the cell for stable charge-discharge cycles.

In the case of Pt/IrO_2/CNTs, the obvious degradation was alleviated as illustrated in Figure 6(B). Each discharge/charge process exhibited flat potential curves and the corresponding potential gap at the beginning and after 6 cycles were 0.93 V and 1.11 V, respectively, showing much improved stability over Pt/CNTs. Throughout the entire cycling, the discharge potentials remained well at 3.5 V, similar to the discharging potential with catalyst Pt/CNTs. However, the charging potential stayed at around 4.5~4.6 V, approximately 0.25 V lower than that from charging with Pt alone. At lower OER overpotentials, Pt suffer less oxidation and thus form a thinner oxide layer, which may reduce the barrier to access active Pt surface for ORR. Consequently, the cell exhibited a much improved discharge performance. As an OER catalyst, IrO_2 not only decreases the charging overpotential, but also protects Pt from over-oxidation.

The Li ion conducting ceramic glass membrane (O'Hara) was reported to be unstable in strong acidic and basic media [39]. To avoid corrosion of the glass membrane

and investigate the cell performance catalyzed by bifunctional catalyst for an extended period, we further conducted cell for discharge/charge in diluted 0.01 M H_2SO_4. Our previous work has found that this concentration of sulfuric acid did not notably impact cell performance [25]. For this study, flat discharge-charge potential curves of Pt/IrO_2/CNTs at 0.2 mA/cm^2 were also found, illustrated in Figure 7. In the first cycle, the discharge and charge potential were found at 3.68 V and 4.45 V, respectively. A slightly higher discharge potential was found than that in concentrated sulfuric acid. Sulfate ion adsorption on the Pt would block active surface and impose a negative electronic effect on the ORR kinetics [40]. In addition, Li ions also affect the Pt ORR in sulfuric acid [41]. More diluted sulfuric acid may alleviate this influence and lead to slightly better ORR activity.

Our previous work has demonstrated the possibilities to achieve a discharge specific capacity of 306 mAh/g and a specific energy of 1067 Wh/kg after 75 hours (based on the weight of sulfuric acid) [25]. To keep the same capacity, the discharging capacity was also cut off at 306 mAh/g. Again, the acid was found to have a 56% utilization of the theoretical capacity 547 mAh/g, and the specific energy density at first discharge was measured at 1110 Wh/kg with a round trip energy efficiency at 81% at the 10^{th} cycle (84% for the 1^{st} cycle). This round trip efficiency is higher than that (72%) we obtained previously [25]; it is also higher than the reported values (*e.g.*, 65%) in aprotic Li-O_2 cells [1].

After 20 cycles, the charge potential raised 100 mV to 4.55 V. The potential gap between charge and discharge increased to 1.02 V, but it is much smaller than those in concentrated acids, as expected. The mild degradation of cell performance may come from the impedance change caused by the glass membrane and inevitable oxidation of Pt metal. In the case of Pt/CNTs [25], the potential gap increased quickly from 0.89 to 1.37 V after 10 cycles, demonstrating the bifunctional catalyst has significantly reduced the overpotential in the Li-air battery, increasing its round trip efficiency and rechargeability.

4. CONCLUSIONS

In summary, we have successfully developed a bifunctional catalyst, Pt/IrO_2/CNTs, for Li-air battery using sulfuric acid as catholyte. The catalyst exhibits excellent catalytic activities with smaller OER overpotentials, higher OER activity and better electrochemical stability. Compared to mono Pt catalyst, the introduction of the bifunctional catalyst significantly reduced the charge voltage by more than 300 mV, and thus increased its round trip efficiency from 72% to 81% (evaluated at the 10^{th} cycle) for mono Pt and bifunctional catalyst, respectively. The hybrid Li-air can be cycled for 20 times without significant degradation. Discharge capacity of 306 mAh/g and specific energy of 1110 Wh/kg were demonstrated for the battery.

5. ACKNOWLEDGMENTS

Financial support by the U.S. Department of Energy ARPA-E grant DEAR0000066 is gratefully acknowledged. We thank Max-Power, Inc. to supply the sealed anodes for our tests and NanoLab, Inc. to supply the carbon nanotubes. We also thank Dr. Eric Bohannan for his help in the XRD analysis and Dr. Kai Song for taking TEM images.

REFERENCES

[1] G. Girishkumar, B. McCloskey, A. C. Luntz, S. Swanson and W. Wilcke, J. Phys. Chem. Lett., 2010, 1, 2193-2203.

[2] P. G. Bruce, S. A. Freunberger, L. J. Hardwick and J.-M. Tarascon, Nat. Mater., 2012, 11, 19-29.

[3] J. Christensen, P. Albertus, R. S. Sanchez-Carrera, T. Lohmann, B. Kozinsky, R. Liedtke, J. Ahmed and A. Kojic, J. Electrochem. Soc., 2012, 159, R1-R30.

[4] K. M. Abraham and Z. Jiang, J. Electrochem. Soc., 1996, 143, 1-5.

[5] J. Read, J. Electrochem. Soc., 2002, 149, A1190-A1195.

[6] J. Read, J. Electrochem. Soc., 2006, 153, A96-A100.

[7] W. Xu, J. Xiao, D. Wang, J. Zhang and J.-G. Zhang, Electrochem. Solid-State Lett., 2010, 13, A48-A51.

[8] D. Aurbach, J. Power Sources, 2000, 89, 206-218.

[9] K. Xu, Chem. Rev., 2004, 104, 4303-4418.

[10] S. J. Visco, B. D. Katz, Y. S. Nimon and L. C. D. Jonghe, Protected Active Metal Electrode and Battery Cell Structure with Non-aqueous Interlayer Architecture. U.S. Patent # 7282295, 2007.

[11] T. Zhang, N. Imanishi, S. Hasegawa, A. Hirano, J. Xie, Y. Takeda, O. Yamamoto and N. Sammes, J. Electrochem. Soc., 2008, 155, A965-A969.

[12] T. Zhang, N. Imanishi, Y. Shimonishi, A. Hirano, Y. Takeda, O. Yamamoto and N. Sammes, Chem. Commun., 2010, 46, 1661-1663.

[13] T. Zhang, N. Imanishi, Y. Shimonishi, A. Hirano, J. Xie, Y. Takeda, O. Yamamoto and N. Sammes, J. Electrochem. Soc., 2010, 157, A214-A218.

[14] P. He, Y. Wang and H. Zhou, Electrochem. Commun., 2010, 12, 1686-1689.

[15] Y. Wang and H. Zhou, J. Power Sources, 2010, 195, 358-361.

[16] Y. Xing, Y. Cai, M. B. Vukmirovic, W.-P. Zhou, H. Karan, J. X. Wang and R. R. Adzic, J. Phys. Chem. Lett., 2010, 1, 3238-3242.

[17] J. Zhang, M. B. Vukmirovic, K. Sasaki, A. U. Nilekar, M. Mavrikakis and R. R. Adzic, J. Am. Chem. Soc., 2005, 127, 12480-12481.

[18] H. A. Gasteiger, S. S. Kocha, B. Sompalli and F. T. Wagner, Appl. Catal. B: Environmental, 2005, 56, 9-35.

[19] E. Yoo and H. Zhou, ACS Nano, 2011, 5, 3020-3026.

[20] J. Suntivich, H. A. Gasteiger, N. Yabuuchi and Y. Shao-Horn, J. Electrochem. Soc., 2010, 157, B1263-B1268.

[21] L. Li, X. Zhao and A. Manthiram, Electrochem. Commun., 2012, 14, 78-81.

[22] Y. Lee, J. Suntivich, K. J. May, E. E. Perry and Y. Shao-Horn, J. Phys. Chem. Lett., 2012, 3, 399-404.

[23] B. E. Conway and T. C. Liu, Langmuir, 1990, 6, 268-276.

[24] G. Jerkiewicz, G. Vatankhah, J. Lessard, M. P. Soriaga and Y.-S. Park, Electrochim. Acta, 2004, 49, 1451-1459.

[25] Y. Li, K. Huang and Y. Xing, Electrochim. Acta, 2012, 81, 20-24.

[26] S. Song, H. Zhang, X. Ma, Z. Shao, R. T. Baker and B. Yi, Int. J. Hydrogen Energy, 2008, 33, 4955-4961.

[27] R. E. Fuentes, J. Farell and J. W. Weidner, Electrochem. Solid-State Lett., 2011, 14, E5-E7.

[28] T. Ioroi, N. Kitazawa, K. Yasuda, Y. Yamamoto and H. Takenaka, J. Electrochem. Soc., 2000, 147, 2018-2022.

[29] W. Yao, J. Yang, J. Wang and Y. Nuli, Electrochem. Commun., 2007, 9, 1029-1034.

[30] F.-D. Kong, S. Zhang, G.-P. Yin, N. Zhang, Z.-B. Wang and C.-Y. Du, Electrochem. Commun., 2012, 14, 63-66.

[31] Y. Xing, L. Li, C. C. Chusuei and R. V. Hull, Langmuir, 2005, 21, 4185-4190.

[32] Y. Xing, J. Phys. Chem. B, 2004, 108, 19255-19259.

[33] L. Li and Y. Xing, J. Phys. Chem. C, 2007, 111, 2803-2808.

[34] E. Rasten, G. Hagen and R. Tunold, Electrochim. Acta, 2003, 48, 3945-3952.

[35] K. Huang, K. Sasaki, R. R. Adzic and Y. Xing, J. Mater. Chem., 2012, 22, 16824-16832.

[36] T. Reier, M. Oezaslan and P. Strasser, ACS Catalysis, 2012, 2, 1765-1772.

[37] R. Kötz, H. J. Lewerenz and S. Stucki, J. Electrochem. Soc., 1983, 130, 825-829.

[38] S.-D. Yim, W.-Y. Lee, Y.-G. Yoon, Y.-J. Sohn, G.-G. Park, T.-H. Yang and C.-S. Kim, Electrochim. Acta, 2004, 50, 713-718.

[39] S. Hasegawa, N. Imanishi, T. Zhang, J. Xie, A. Hirano, Y. Takeda and O. Yamamoto, J. Power Sources, 2009, 189, 371-377.

[40] J. X. Wang, N. M. Markovic and R. R. Adzic, J. Phys. Chem. B, 2004, 108, 4127-4133.

[41] H. Liu and Y. Xing, Electrochem. Commun., 2011, 13, 646-649.

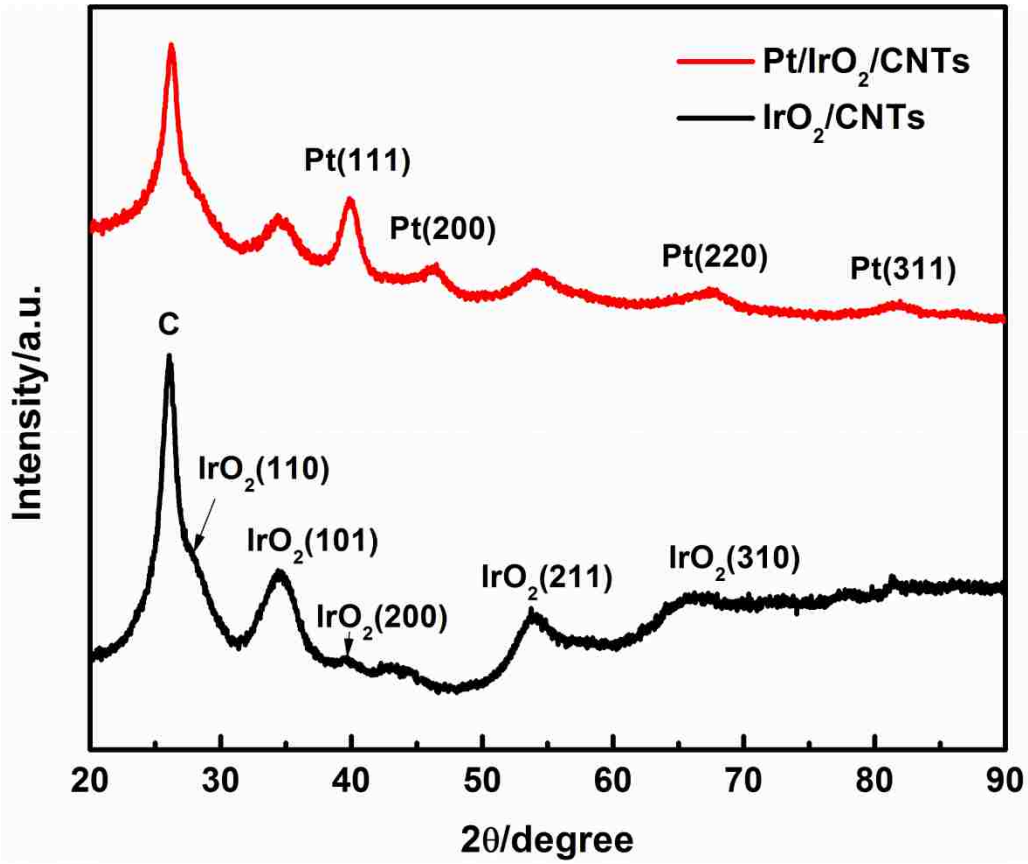

Fig. 1 X-ray diffraction patterns of catalysts IrO_2/CNTs and Pt/IrO_2/CNTs, showing a rutile IrO_2 and fcc Pt supported on carbon nanotubes. For clarity, the IrO_2 peaks are not marked on the pattern of catalyst Pt/IrO_2/CNTs.

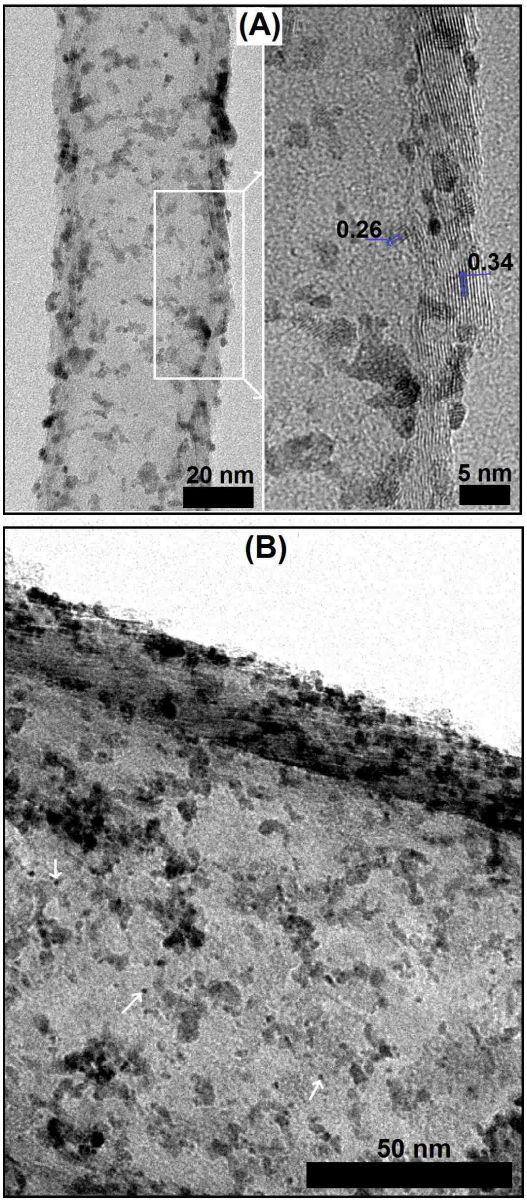

Fig. 2 TEM images of: (A) IrO_2/CNT, shown are a low and a high magnification images. The numbers on the right image are lattice spacing (in nanometers), with 0.34 nm for graphite and 0.26 nm corresponding to rutile IrO_2 crystalline plane (101). (B) Pt/IrO_2/CNTs, showing the round dark black dots as Pt nanoparticles (e.g., those indicated by arrows); no obvious morphological changes of the IrO_2 particles were observed.

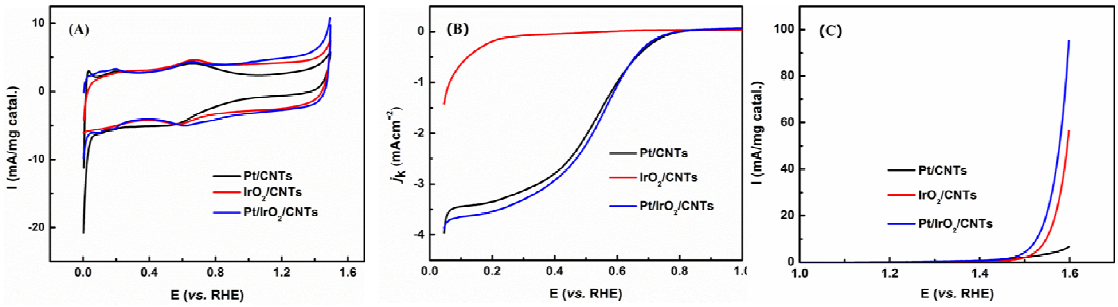

Fig. 3 Electrochemical characterizations of catalysts. (A) cyclic voltammetry curves of Pt/CNTs, IrO_2/CNTs and Pt/IrO_2/CNTs; (B) polarization curves of ORR on Pt/CNTs, IrO_2/CNTs and Pt/IrO_2/CNTs; (C) polarization curves of OER on Pt/CNTs, IrO_2/CNTs and Pt/IrO_2/CNTs.

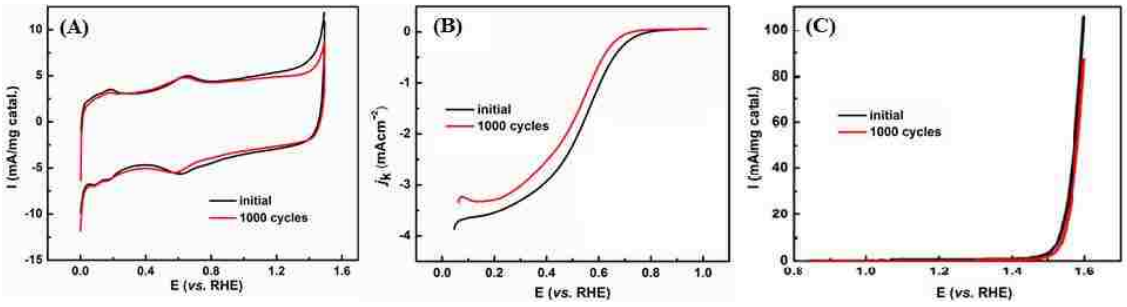

Fig. 4 Electrochemical characterizations of catalyst Pt/IrO_2/CNTs before and after 1000 cycles. (A) Cyclic voltammetry curves; (B) Polarization curves of ORR; (C) OER activities.

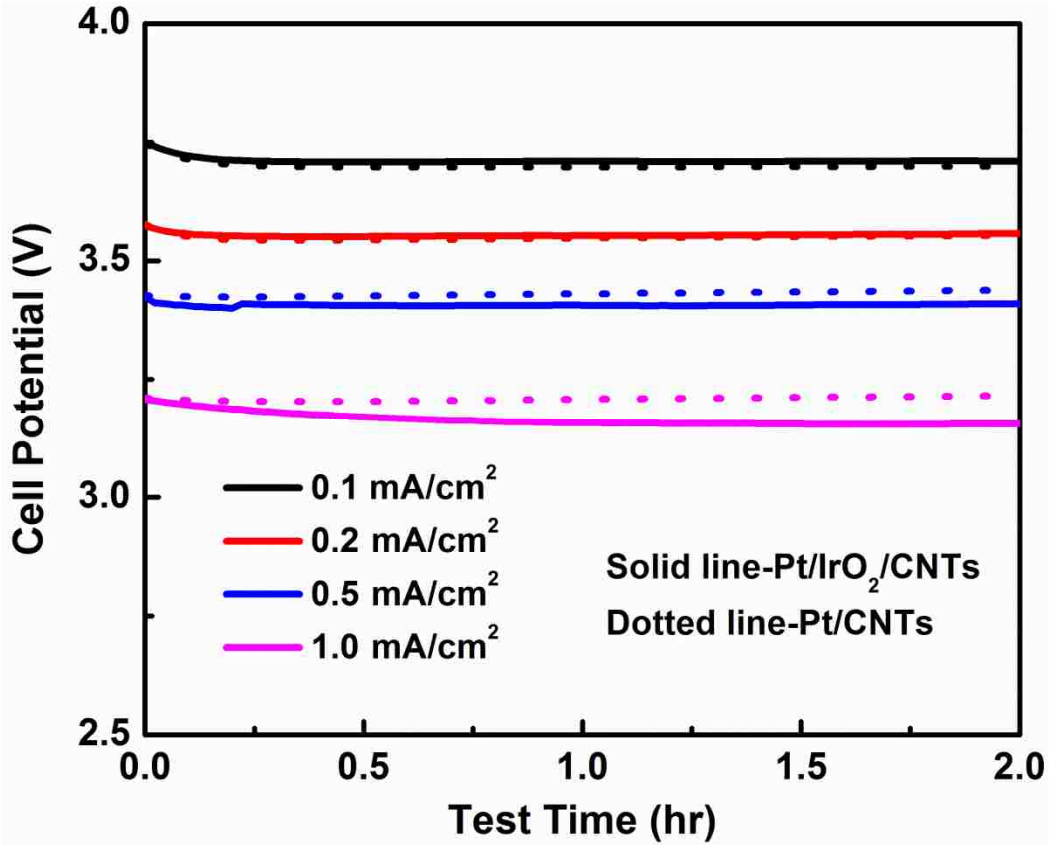

Fig. 5 Performance in discharge of Li-air battery catalyzed by Pt/CNTs and Pt/IrO_2/CNTs at different discharge current densities.

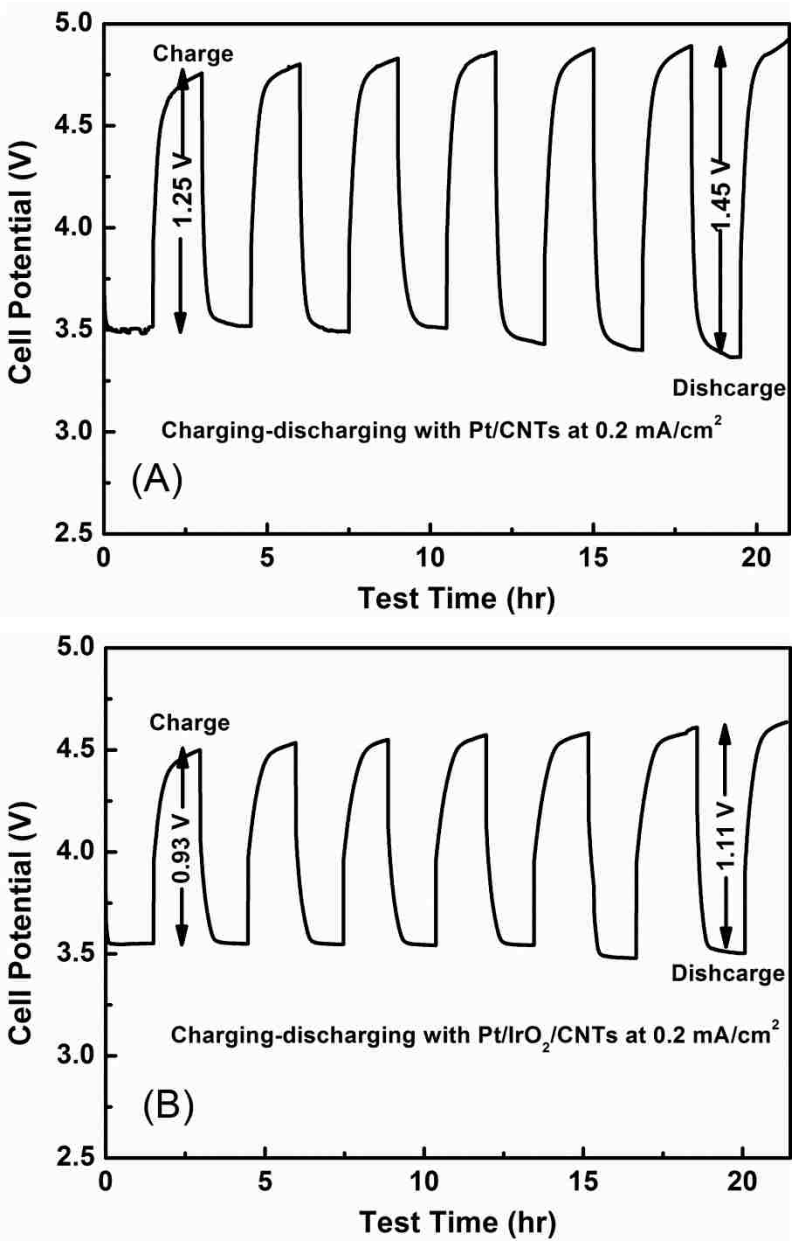

Fig. 6 Charge-discharge performance of Li-air cell at 0.2 mA/cm^2 in 1.0 M H_2SO_4 with (A) cathode with Pt/CNTs, and (B) cathode with Pt/IrO_2/CNTs cathode.

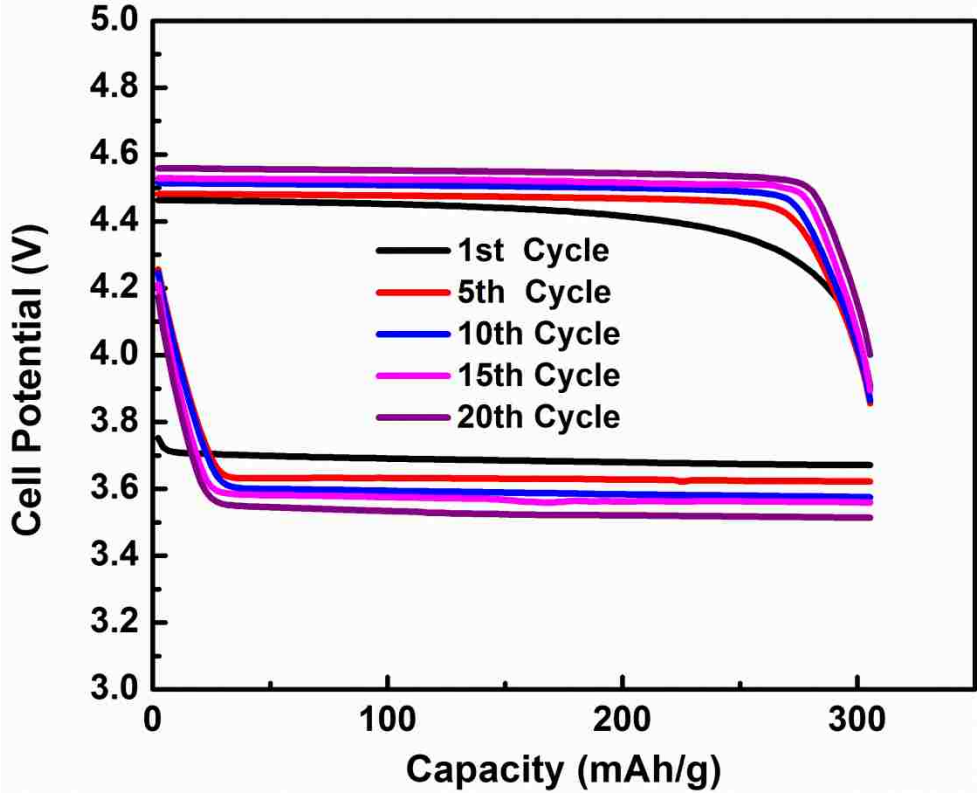

Fig. 7 Cycling performance of Li-air cell catalyzed by $Pt/IrO_2/CNTs$ at 0.2 mA/cm^2 in 0.01 M H_2SO_4 catholyte.

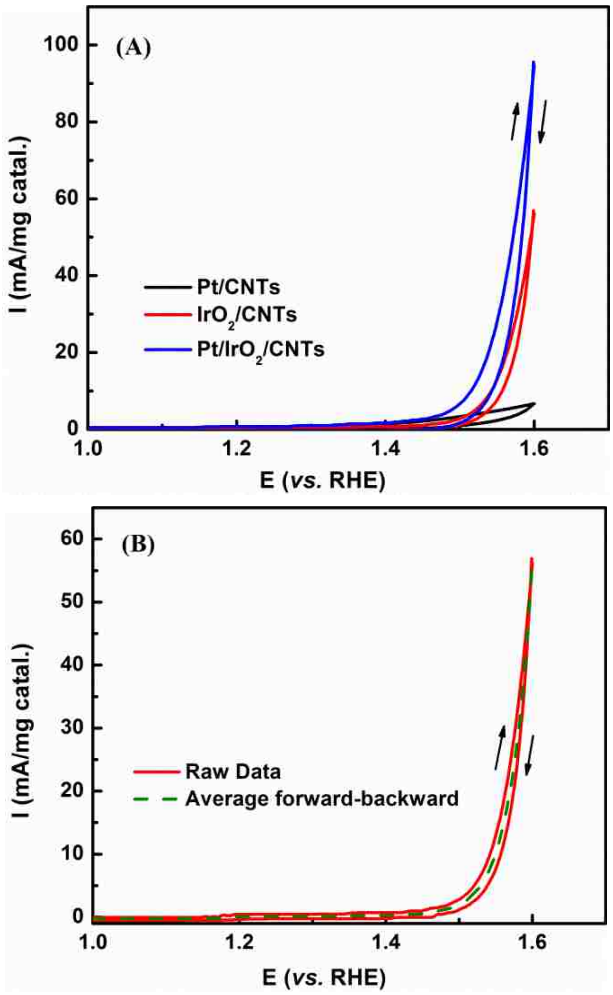

Figure S1. OER activity with capacitive correction. (A) OER activities of Pt/CNT, IrO_2/CNTs and Pt/IrO_2/CNTs taken by forward and backward scans with scan rate of 5 mV/s and 1600 rpm in N_2-saturated 1.0 M H_2SO_4. (B) Example of capacitive correction of the as-measured OER activity of catalysts. The as-measured OER activity of IrO_2/CNTs is capacitance-corrected by taking an average of forward and backward scans.

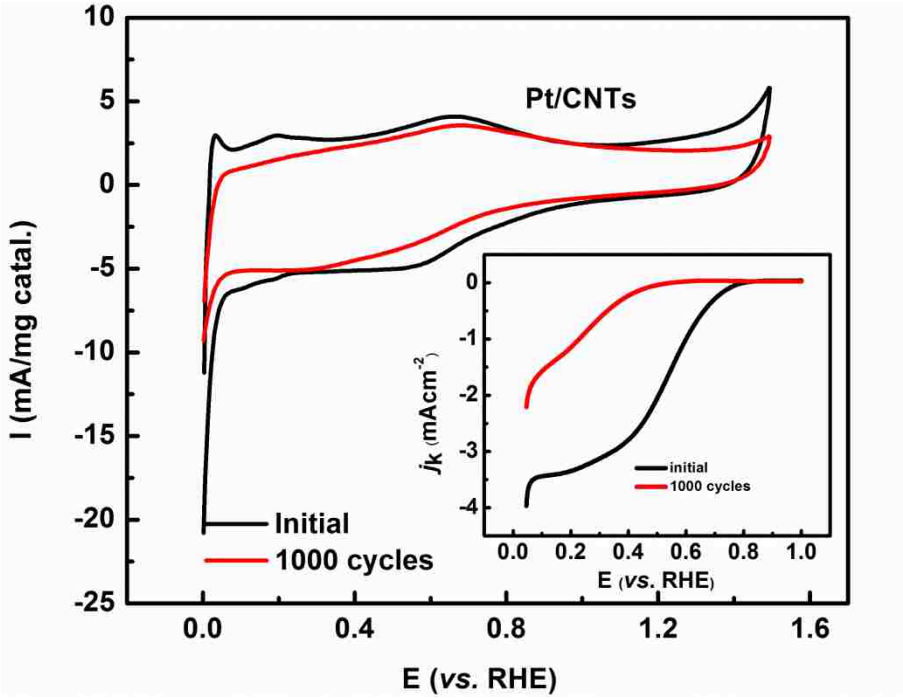

Figure S2. CV curves of Pt/CNTs before and after 1000 cycles. The durability protocol was carried in N_2-bubbled 1.0 M H_2SO_4 in the potential range between 0.6-1.5 V for 1000 cycles with scan rate of 50 mV/s. The inset figure shows the ORR curves before and after 1000 cycles. ORR measurement was taken in an O_2-saturared 1.0 M H_2SO_4 at rotating speed of 1600 rpm between 0.2-1.0 V.

V. SYNTHESIS OF NIOBIUM OXID-CARBON NANOTUBE SUPPORTED PLATINUM FOR OXYGEN RECUTION REACTION

Kan Huang[1], Yunfeng Li[2], Yangchuan Xing[2a]

[1]Department of Chemical and Biological Engineering, Missouri University of Science and Technology, Rolla, MO, 65409
[2]Department of Chemical Engineering, University of Missouri at Columbia, Columbia, MO, 65211
[a]Address all correspondence to this author. Email: xingy@missouri.edu

ABSTRACT

Niobium oxide nanocoating on carbon nanotubes (CNTs) was synthesized via a sol-gel method, followed by thermal carbon doping. By using CNTs as template for nanocoating, the nanoscale morphology of oxide was retained during thermal treatment. Annealing carbon doped niobium oxide under H_2/N_2 atmosphere at lower temperature, X-ray diffraction showed that niobium pentoxide (Nb_2O_5) was reduced to niobium dioxide (NbO_2). In the contrast, directly annealing Nb_2O_5 under the same condition would not complete the phase transformation to NbO_2, suggesting that carbon doping can facilitate the phase transformation. X-ray photoelectron spectroscopy also suggested a shift of Nb 3d to the lower binding energy, which implies that a formation of suboxide layer on the surface. Electrochemical studies showed that Pt supported on the carbon doped Nb_2O_5/CNTs has a greater electrochemical activity than that of on the undoped Nb_2O_5/CNTs. However, Pt supported on the carbon doped Nb_2O_5/CNTs exhibited an

inferior oxygen reduction activity and stability than a commercial Pt/C catalyst, implying that carbon doped Nb_2O_5/CNTs may not be considered as a suitable eletrocatalyst support.

1. INTRODUCITON

Oxygen reduction reaction (ORR) in acidic and alkaline media has been being an intensive research hotspot in proton exchange membrane fuel cell (PEMFC) [1-4]. To date, Pt is still the most active catalyst for ORR [5], however, the persistent challenges with Pt-based catalysts are their sluggish kinetics of ORR. At potential over 0.75 V, OH and O groups form strong bonds with Pt surface sites, which block the further access of O_2 to the active Pt sites [6]. Another problem associated with practical utilization of Pt is its instability during electrochemical process. Carbon was widely used as Pt support, unfortunately, carbon corrosion and ORR activity loss became a principal drawback [7, 8]. The emergence of more corrosion resistant carbon nanotubes (CNTs) was found to mitigate the corrosion, however, degradation of catalyst was still found [9, 10].

To stabilize Pt electrocatalyst, TiO_2 based oxide as supports were proposed and obvious improvements were observed [11-15]. Among them, Magneli phase of Ti_4O_7, was commercialized under Ebonex® trade name and proved to be stable under corrosive circumstance [16, 17]. Recently, niobium oxides (NbO, Nb_2O_5 and NbO_2) as Pt supports have been investigated [18-20]. Sasaki *et al.* [18] demonstrated that deposition of

ultra-low Pt on niobium oxide exhibited higher ORR activity and improved stability against Pt dissolution. They argued that the lateral repulsion between OH/O and oxide surface was responsible for the ORR activity enhancement. Zhang *et al.* [19] also found the improved ORR activity and stability of Pt/NbO_2/CNTs electrocatalyst, which were attributed to the electronic charge density change on the Pt surface.

In this work, we demonstrate a nanoscale carbon doped niobium oxide coating on CNTs as Pt support. A sol-gel process was used to obtain a Nb_2O_5 nanocoating and subsequent carbon doping [13] was applied. It was observed that carbon doping not only facilitates the phase transformation from Nb_2O_5 to NbO_2 at lower temperature, but also increases the conductivity of supports. Furthermore, electrochemical measurements were carried out to characterize the oxide supported Pt electrocatalyst.

2. EXPERIMENTAL

CNTs (Pyrograf Products, Inc., 60~150 nm in diameter and 30~100 microns in length) were treated with 3:1 H_2SO_4/HNO_3 (volume ratio) in an ultrasonic bath at 60 °C for 2 hours for surface functionalization [13], followed by filtration and thorough washing with deionized water. 10 mg treated CNTs were dispersed in a solution containing 8 mL ethanol, 2 mL benzyl alcohol plus excess water with aid of ultrasonication and stirring. Desired amount of niobium ethoxide (Sigma-Aldrich) was dissolved in N_2-saturated ethanol and slowly dipped into CNTs suspension and stirred for

2 hr, followed by vacuum filtration and dried at 80 ^{o}C in oven overnight. The synthesized Nb_2O_5/CNTs were thermally doped under 10% acetylene in N_2 at 700 ^{o}C for 20 min (designated as c-Nb_2O_5/CNTs). Some c-Nb_2O_5/CNTs and Nb_2O_5/CNTs were further annealed under 10% H_2 in N_2 at 700-800 ^{o}C for another 3hr, named as c-Nb_2O_5/CNTs-700 and c-Nb_2O_5/CNTs-800, respectively. Finally, deposition of Pt on carbon doped or undoped niobium oxide-CNTs was achieved by polyol reduction method [21], keeping Pt loading at 10 wt.%.

The morphologies were examined by transmission electron microscope (TEM) (Philips EM430) operating at 300 kV. The crystalline of catalysts were analyzed by X-ray diffraction (XRD) (X-Pert Philips) equipped with Cu K(α) X-ray photoelectron spectroscopy (XPS) (Kratos Axis 165) was used to analyze Nb (3d) and O (1s) by employing Al K (α) excitation, operated at 150W and 15kV.

All electrochemical experiments were performed with an Electrochemical Workstation (Bioanalytical Sciences, BAS 100). The working electrode was a glassy carbon rotating disk electrode (RDE) with a disk diameter at 5 mm (Gamry RDE 710). A Pt wire was used as the counter electrode and saturated Ag/AgCl as a reference electrode. The catalyst powder was dispersed in deionized water by sonication for 20 min to form 1 mg/mL catalyst suspension. 20 μL of the suspension was pipetted onto the disk and dried in air. About 5 μL Nafion solution (0.05 wt.%, Alfa Aesar) was then put on top of the catalyst. Cyclic voltammetry (CV) was carried out in N_2 purged 1.0 M H_2SO_4 at potential range of 0-1.2 V (*vs.* RHE). ORR measurement was taken in an O_2-saturared 1.0 M

H_2SO_4 at rotating speed of 1600 rpm between 0.2-1.0 V (*vs.* RHE). To study the durability of Pt on niobium oxide-CNTs, CV was conducted in air saturated 1.0 M H_2SO_4 in the potential range between 0.6 and 1.0 V (*vs.* RHE) up to 5000 cycles. The initial and final CV and ORR behaviors were recorded. For comparison, commercial E-TEK (20 wt.% Pt/C) was also tested under the same cycling conditions.

3. RESULTS AND DISCUSSION

Morphology of Nb_2O_5 coated CNTs was presented in Fig. 1 (A) and EDX analysis confirmed the presence of Nb element in Nb_2O_5/CNTs sample. The nanocoating was found to be uniform and smooth, and the thickness of coating can be easily adjusted by varying the niobium ethoxide amount. Removing the CNTs backbone by annealing Nb_2O_5/CNTs in air at 600 ^oC, pure Nb_2O_5 nanotubes was obtained as shown in Fig. (B). It provides an easy route to synthesize oxide nanotubes.

Crystalline information of catalyst and supports were illustrated in Fig. 2. The Nb_2O_5/CNTs obtained by sol-gel method has an amorphous structure, and the crystallized Nb_2O_5 were obtained after annealing under N_2, as seen in Fig. 2 (A). After carbon doping, crystal pattern of c-Nb_2O_5/CNTs exhibited similar crystal pattern as Nb_2O_5/CNTs, suggesting that the bulk crystal pattern has not changed. Hahn *et al.* [22] suggested that at lower temperature, carbon doping is mostly a surface deposition process and only distorts the surface lattice rather than the bulk. Huang *et al.* [23] also observed that

carbon doping pure TiO_2 nanoparticles at 700 ^oC would not create a new phase, but a surface distortion. As presented in Fig. 2(B) and (C), characteristic peaks belonging to NbO_2 *e.g.* NbO_2 (400) began to appear after post-thermal annealing c-Nb_2O_5/CNTs under H_2/N_2, indicating that Nb_2O_5 was reduced to NbO_2. Annealing at 700 ^oC, the oxide was a mixture of Nb_2O_5 and NbO_2. Increasing to 800 ^oC, the main composite of oxide was found to be NbO_2. Higher annealing temperature was not chosen in order to avoid the nanocoating pealing from CNTs surface. In a separate experiment, undoped Nb_2O_5/CNTs was annealed under the same conditions as c-Nb_2O_5/CNTs and comparison of XRD pattern were shown in Fig. 2(B) and (C). It was found that directly annealing undoped Nb_2O_5/CNTs would not transform Nb_2O_5 to NbO_2, which usually required higher calcinations temperature *e.g.* 900 ^oC under H_2 atomosphere [18, 24]. Toyoda *et al.* [25] annealed the mixture of TiO_2 with carbon source in N_2 instead of directly reducing TiO_2 in pure H_2. They found the formation of titanium suboxide such as Ti_4O_7 at a lower temperature. Koc and Folmer thermal treated carbon coated TiO_2 nanoparticles in argon and found the generation of titanium suboxide, and they suggested that carbon was involved in the reduction of TiO_2 by the partially substitution of oxygen atom in TiO_2 [26]. Huang *et al.* [13] also found that carbon atom can be interstitially incorporated into TiO_2 lattice, resulting the lattice expansion. We speculated that doped carbon may partially react with oxygen atom in Nb_2O_5, as well as expand the Nb_2O_5 lattice which may favor the phase transformation in the post-thermal treatment. Finally, Pt nanoparticles are crystalline, as indicated by the characteristic peaks of Pt [21].

The chemical states of Nb and O were investigated by XPS, and the results were shown in Fig. 3. In Fig. 3(A), the binding energy (BEs) of Nb $3d_{5/2}$ and Nb $3d_{3/2}$ in Nb_2O_5/CNTs were found at 208.1 eV and 210.9 eV, respectively, in a good agreement with those of Nb_2O_5 reported by U.S. National Institute of Standards and Technology (NIST) with Nb $3d_{5/2}$ at 208.1 eV and Nb $3d_{3/2}$ at 210.2 eV. In the scenario of c-Nb_2O_5/CNTs-700, a negative shift towards lower BEs was observed and BEs of Nb $3d_{5/2}$ and Nb $3d_{3/2}$ were observed at 207.3 eV and 210.9 eV, respectively. According to Jung [27] and NIST, Nb $3d_{5/2}$ in NbO_2 displays BEs of Nb $3d_{5/2}$ at 205.7 eV. Huang *et al.* [13] suggested that carbon doping can change the TiO_2 electron structure between conducting band and valence band, resulting a BEs shift. Therefore, the Nb 3d BEs in c-Nb_2O_5/CNTs-700 shift towards lower oxidation state may suggest a formation of suboxide layer. The O 1s found at 530.3 eV in c-Nb_2O_5/CNTs-700 also suffered a negative shift compared with Nb_2O_5/CNT, as presented in Fig. 3(B). XPS analysis corroborated the XRD finding that a reduced phase of NbO_2 was partially formed.

Fig. 4 shows typical TEM images of Pt nanoparticles dispersed on Nb_2O_5/CNTs and c-Nb_2O_5/CNTs-700. The thin Nb_2O_5 coating was found to be well maintained during doping process and the thickness was measured at 5~8 nm. From the image, Pt nanoprticles is uniformly dispersed on the support and aggregation is minimal. The Pt average particles sizes are estimated to be 2.3±0.4 nm on Nb_2O_5/CNTs and 3.2±0.5 nm on c-Nb_2O_5/CNTs-700, respectively, which are based on counting over 100 randomly picked particles.

Fig. 5(A) showed the CV curves of Nb_2O_5/CNTs and c-Nb_2O_5/CNTs-700 in N_2-saturated 1.0 M H_2SO_4. No specific oxidation and reduction current peaks emerged, demonstrating that Nb_2O_5/CNTs and c-Nb_2O_5/CNTs-700 were catalytic inactive in acid electrolyte. ORR polarization curves of Nb_2O_5/CNTs and c-Nb_2O_5/CNTs-700 were presented in Fig. 5(B). Both possessed negligible catalytic activity towards ORR, only a minor increase in the cathodic current below 0.2 V is apparent, which supports our argument that Nb_2O_5/CNTs and c-Nb_2O_5/CNTs-700 were catalytic inert at ORR potential range. Fig. 5(C) plotted CV curves of Pt on Nb_2O_5/CNTs, c-Nb_2O_5/CNTs-700 and carbon black. Pt on Nb_2O_5/CNTs did not show obvious Pt oxidation and Pt-oxide reduction peaks as Pt on c-Nb_2O_5/CNTs-700, only hydrogen adsorption/desorption peaks appeared distinguishable. Nb_2O_5 has an orthorhombic pseudohexagonal structure and is an insulator, whereas NbO_2 is an n-type semiconductor at room temperature [18, 19]. Our previous investigation showed that Pt on undoped TiO_2/CNTs has a delay in the reduction of Pt-oxides compared to on carbon doped TiO_2/CNTs, which can be attributed to the difference in the electronic conductivity [13]. The different electrochemical behaviors of Pt on supports demonstrated that carbon doping and post thermal treatment indeed increased the conductivity of support. The electrochemical surface areas (ESA) of catalysts were obtained from the CV curves by integrating the area of hydrogen adsorption region (~0.05-0.3 V) [21, 28], and were calculated to be 1075 cm^2/mg_{Pt} and 1114.285 cm^2/mg_{Pt} for E-TEK and Pt/c-Nb_2O_5/CNTs-700, which makes them suitable for comparing their catalytic activities. The measurements of ORR for Pt/Nb_2O_5/CNTs,

Pt/c-Nb_2O_5/CNTs-700 and E-TEK are illustrated in Fig. 5(D). The half-wave potentials for Pt/Nb_2O_5/CNTs, Pt/c-Nb_2O_5/CNTs-700 and E-TEK are measured to be 0.569 V, 0.734 V and 0.766 V, respectively. The better ORR performance of E-TEK than Pt/c-Nb_2O_5/CNTs-700 is mainly due to the double Pt loading (20 wt.% in Pt/C vs.10 wt.% in Pt/c-Nb_2O_5/CNTs-700). Sasaki *et al.* [18] suggested that the difference in electrical conductivity between Pt/Nb_2O_5/C and Pt/NbO_2/C is likely to be one of plausible causes of difference in ORR activity. The low electrical conductivity of Nb_2O_5 would hamper the electron transfer between Pt and CNTs, consequently, degrade the electrocatalytic performance.

Tafel plots derived from the kinetic currents, j_k, using Koutecky-Levich theory [29] are shown in Fig. 6; all the Tafel curves are normalized to the individual ESA of Pt and total mass of Pt. In the kinetically controlled region (~0.67-0.85 V), E-TEK displays the highest kinetic current based on either ESA or mass.

To gain information about the stability of the catalysts, cycling test was carried by applying 5000 potential cycles from 0.6-1.0 V (*vs.* RHE) in N_2-bubbled 1.0 M H_2SO_4. Comparison of the ORR activity before and after cycles was made. As shown in the inset of Fig. 7, the ESA loss was found to be 40% in Pt/c-Nb_2O_5/CNTs-700 *vs.* 30% in E-TEK [13]. And the half-wave potential of Pt/c-Nb_2O_5/CNTs-700 suffers obvious shift after cycles, from 0.734 V to 0.653 V. In the contrast, the half-wave potential loss in E-TEK was observed from 0.766 V to 0.736 V. Especially, the loss in ORR mass activity of Pt/c-Nb_2O_5/CNTs-700 is 68% at 0.75 V and 65% at 0.8 V. In comparison, the ORR mass

activity loss in E-TEK was found to be 53% at 0.75V and 56% at 0.8 V. All those findings suggested that Pt/c-Nb_2O_5/CNTs-700 exhibited inferior stability than commercial E-TEK. Senevirathne *et al.* [24] observed ~57% of ORR activity loss and ~60% ESA loss in Pt/NbO_2, which was cycled in 0.1 M $HClO_4$. Through XPS measurements of Pt/NbO_2 before and after cycles, they found the formation of electronically insulating Nb_2O_5 that can be partially responsible for the loss of ORR activity. Therefore, the rapid deterioration of ORR activity in Pt/c-Nb_2O_5/CNTs-700 may be attributed to the following two factors (1) Re-oxidation of NbO_2 layer into electronic insulating Nb_2O_5 during cycles that limits the electron transport between oxide layer and CNTs; and (2) Possible dissolution and agglomeration of Pt particles that evidently decrease the ESA.

4. CONCLUSIONS

Here we report a study of carbon doped Nb_2O_5 nanocoating on CNTs as Pt electrocatalyst support for ORR. Nb_2O_5 coated CNTs was achieved via a sol-gel method, leading to a nanoscale thin Nb_2O_5 coating. By removing the CNTs template, pure Nb_2O_5 nanotube can be obtained. One step carbon doping Nb_2O_5/CNTs and further annealing under H_2/N_2 were carried. It was found that carbon doping can facilitate the phase transformation from Nb_2O_5 to NbO_2 at lower temperature, which was not observed in undoped Nb_2O_5. Electrochemical measurements were performed to characterize the ORR

activity of Pt supported on doped (undoped) Nb_2O_5/CNTs. The results indicated that Pt on c-Nb_2O_5/CNTs-700 exhibited superior electrochemical activities than Pt on Nb_2O_5/CNTs, suggesting that carbon doping and post thermal treatment can improve the catalyst activity. However, Pt/c-Nb_2O_5/CNTs-700 showed less ORR activity than commercial E-TEK. Under oxidizing conditions of 5000 potential cycles from 0.6-1.0 V, Pt on c-Nb_2O_5/CNTs-700 suffers 40% loss of its original ESA and 68% loss of its mass ORR activity at 0.75 V, compared with 30% ESA loss and 53% ORR activity loss. The ORR activity loss may come from the re-oxidation of Nb_2O_5 layer into electronic insulator Nb_2O_5 during cycles that limits the electron transport between oxide layer and CNTs. This work demonstrated that carbon doped Nb_2O_5/CNTs may not be suitable as Pt supports for ORR.

5. ACKNOWLEDGMENTS

The authors would like to thank partial financial support for this research from the U.S. Department of Energy ARPA-E grant DE-AR0000066. We thank Dr. Eric Bohannan for XRD analysis, Mr. Brian Porter for XPS analysis and Dr. Kai Song for taking TEM images.

REFERENCES

[1] X. Wang, N. M. Markovic and R. R. Adzic, J. Phys. Chem. B, 2004, 108, 4127-4133.

[2] H. A. Gasteiger, S. S. Kocha, B. Sompalli and F. T. Wagner, Appl. Catal. B: Environmental, 2005, 56, 9-35.

[3] J. Zhang, M. B. Vukmirovic, K. Sasaki, A. U. Nilekar, M. Mavrikakis and R. R. Adzic, J. Am. Chem. Soc., 2005, 127, 12480-12481.

[4] R. Adzic, J. Zhang, K. Sasaki, M. Vukmirovic, M. Shao, J. Wang, A. Nilekar, M. Mavrikakis, J. Valerio and F. Uribe, Top. Catal., 2007, 46, 249-262.

[5] Y. Xing, Y. Cai, M. B. Vukmirovic, W.-P. Zhou, H. Karan, J. X. Wang and R. R. Adzic, J. Phys. Chem. Lett., 2010, 1, 3238-3242.

[6] J. K. Nørskov, J. Rossmeisl, A. Logadottir, L. Lindqvist, J. R. Kitchin, T. Bligaard and H. Jónsson, J. Phys. Chem. B, 2004, 108, 17886-17892.

[7] P. J. Ferreira, G. J. la O, Y. Shao-Horn, D. Morgan, R. Makharia, S. Kocha and H. A. Gasteiger, J. Electrochem. Soc., 2005, 152, A2256-A2271.

[8] K. J. J. Mayrhofer, J. C. Meier, S. J. Ashton, G. K. H. Wiberg, F. Kraus, M. Hanzlik and M. Arenz, Electrochem. Commun., 2008, 10, 1144-1147.

[9] L. Li and Y. Xing, J. Electrochem. Soc., 2006, 153, A1823-A1828.

[10] L. Li and Y. Xing, J. Power Sources, 2008, 178, 75-79.

[11] J. R. Smith, F. C. Walsh and R. L. Clarke, J. Appl. Electrochem., 1998, 28, 1021-1033.

[12] A. Bauer, K. Lee, C. Song, Y. Xie, J. Zhang and R. Hui, J. Power Sources, 2010, 195, 3105-3110.

[13] K. Huang, K. Sasaki, R. R. Adzic and Y. Xing, J. Mater. Chem., 2012, 22, 16824-16832.

[14] S.-Y. Huang, P. Ganesan and B. N. Popov, Appl. Catal. B: Environmental, 2010, 96, 224-231.

[15] N. R. Elezovic, B. M. Babic, V. R. Radmilovic, L. M. Vracar and N. V. Krstajic, Electrochim. Acta, 2011, 56, 9020-9026.

[16] T. Ioroi, H. Senoh, S.-i. Yamazaki, Z. Siroma, N. Fujiwara and K. Yasuda, J. Electrochem. Soc., 2008, 155, B321-B326.

[17] F. C. Walsh and R. G. A. Wills, Electrochim. Acta, 2010, 55, 6342-6351.

[18] K. Sasaki, L. Zhang and R. R. Adzic, Phys. Chem. Chem. Phys., 2008, 10, 159-167.

[19] L. Zhang, L. Wang, C. M. B. Holt, T. Navessin, K. Malek, M. H. Eikerling and D. Mitlin, J. Phys. Chem. C, 2010, 114, 16463-16474.

[20] L. Zhang, L. Wang, C. M. B. Holt, B. Zahiri, Z. Li, K. Malek, T. Navessin, M. H. Eikerling and D. Mitlin, Energy & Environmental Science, 2012, 5, 6156-6172.

[21] Y. Xing, J. Phys. Chem. B, 2004, 108, 19255-19259.

[22] R. Hahn, A. Ghicov, J. Salonen, V.-P. Lehto and P. Schmuki, Nanotechnology, 2007, 18, 105604.

[23] K. Huang, Y. Li and Y. Xing, J. Mater. Res., 2013, 28, 454-460.

[24] K. Senevirathne, R. Hui, S. Campbell, S. Ye and J. Zhang, Electrochim. Acta, 2012, 59, 538-547.

[25] M. Toyoda, T. Yano, B. Tryba, S. Mozia, T. Tsumura and M. Inagaki, Appl. Catal. B: Environmental, 2009, 88, 160-164.

[26] R. Koc and J. S. Folmer, J. Mater. Sci., 1997, 32, 3101-3111.

[27] K. Jung, J. Appl. Phys., 2011, 109, 054511.

[28] L. Li and Y. Xing, J. Phys.Chem. C, 2007, 111, 2803-2808.

[29] Allen J. Bard and L. R. Faulkner, Electrochemical Methods: Fundamentals and Applications., John Wiley &Sons, New York, 2001.

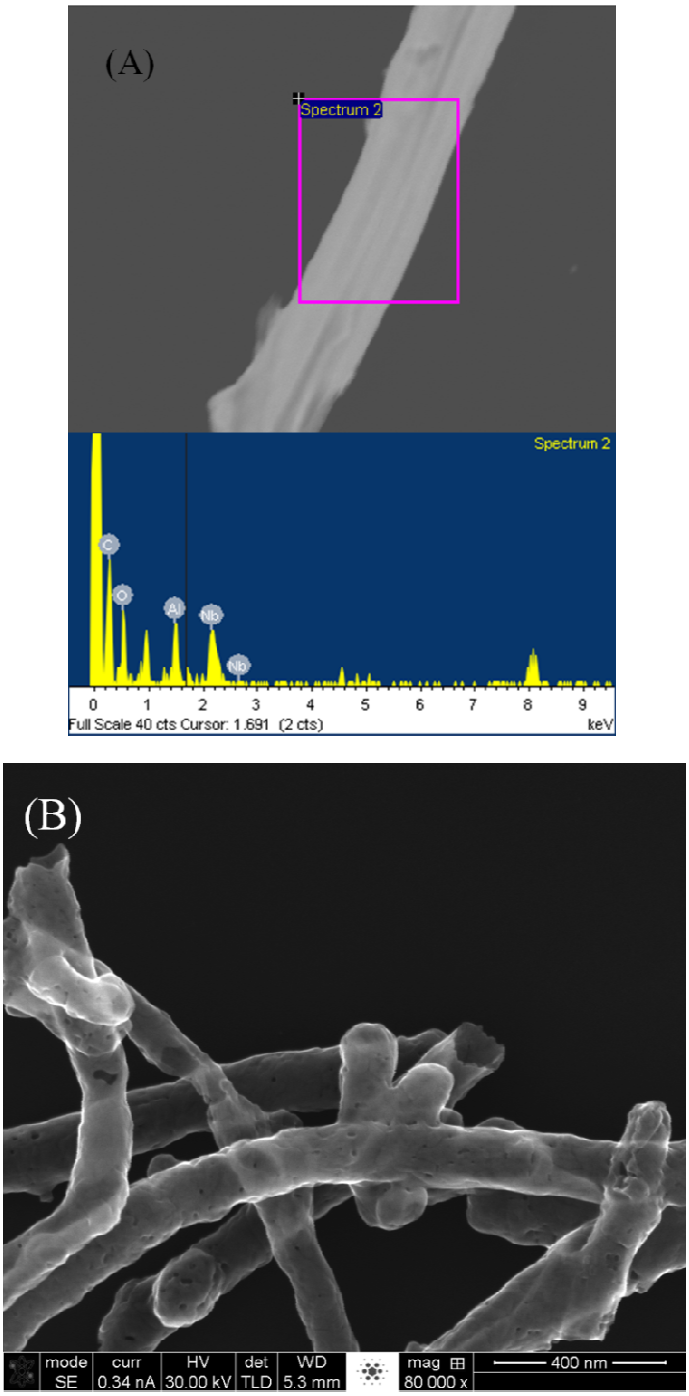

Fig. 1 (A) EDX of a Nb_2O_5/CNT sample supported on a copper mesh TEM grid, showing the presence of Ti element. (B) thin Nb_2O_5 nanotubes after removing CNTs template.

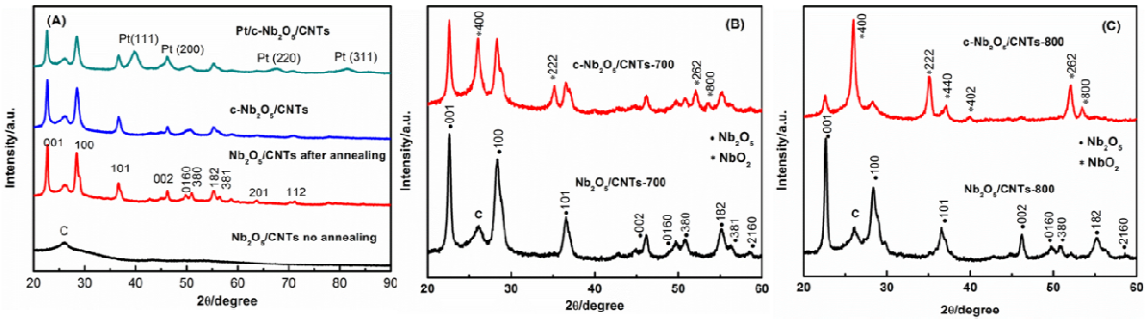

Fig. 2 (A) XRD pattern of Nb_2O_5/CNTs, c-Nb_2O_5/CNTs and Pt/c-Nb_2O_5/CNTs. (B) XRD pattern comparison of c-Nb_2O_5/CNTs and Nb_2O_5/CNTs annealed in H_2/N_2 at 700 ^oC. (C) XRD pattern comparison of c-Nb_2O_5/CNTs and Nb_2O_5/CNTs annealed in H_2/N_2 at 800 ^oC.

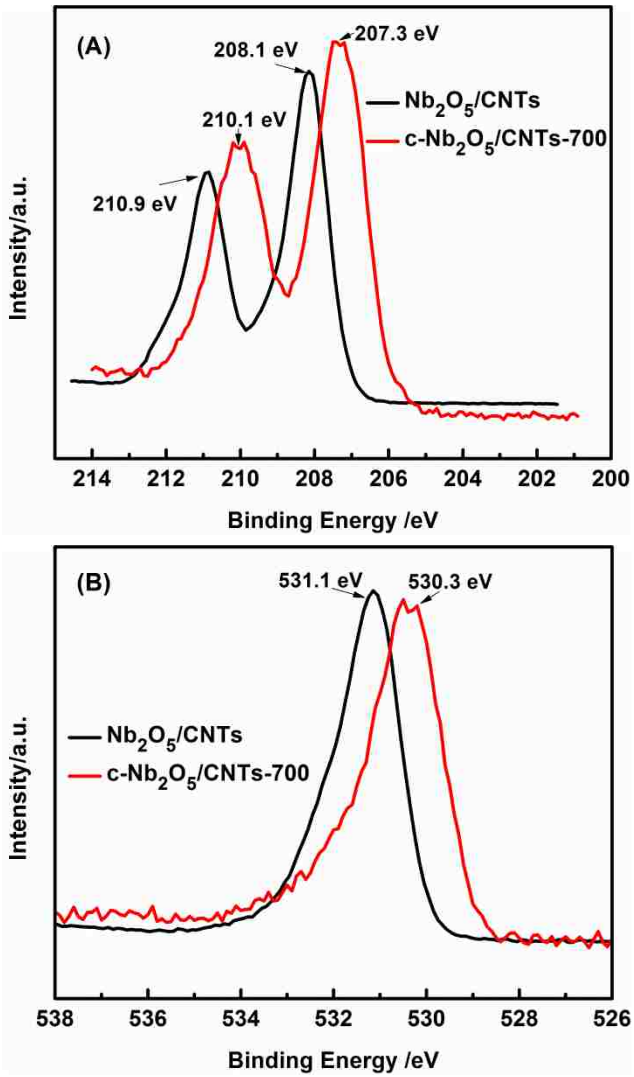

Fig. 3 XPS result of Nb 3d and O 1s from c-Nb_2O_5/CNTs-700 and Nb_2O_5/CNTs.

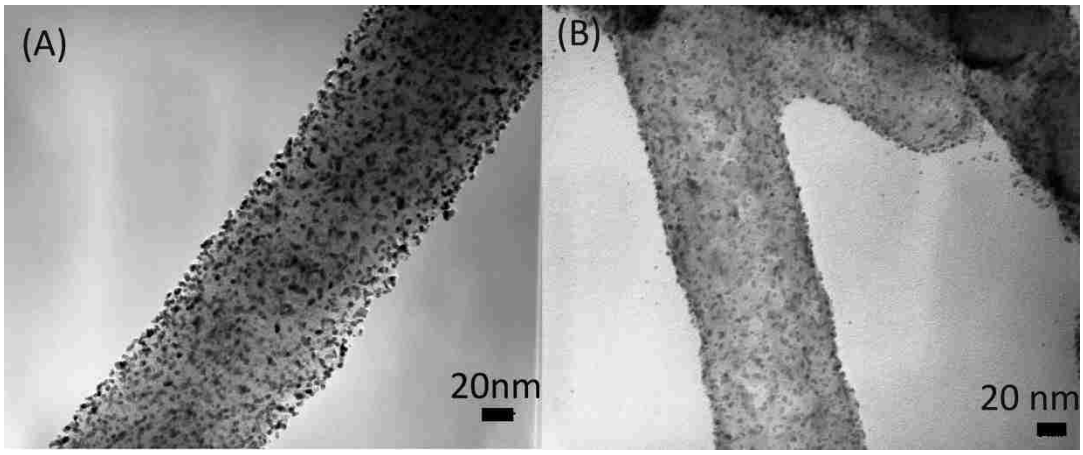

Fig. 4 TEM images of 10wt.% Pt nanoparticles on (A) c-Nb_2O_5/CNTs-700 and (B) Nb_2O_5/CNTs.

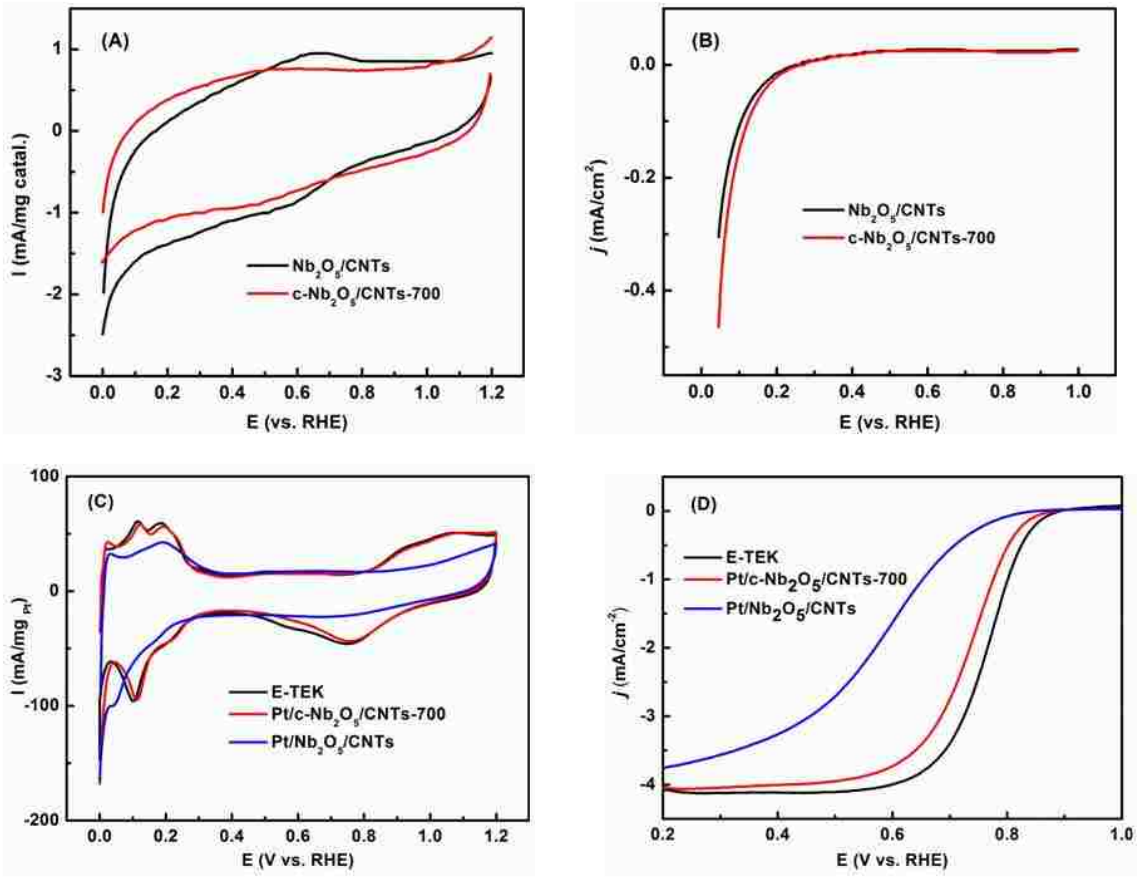

Fig. 5 Electrochemical characterizations of catalysts. (A) cyclic voltammetry curves of Nb_2O_5/CNTs and c- Nb_2O_5/CNTs-700. (B) polarization curves of ORR on Nb_2O_5/CNTs and c- Nb_2O_5/CNTs-700. (C) cyclic voltammetry curves of Pt/ Nb_2O_5/CNTs, Pt/Nb_2O_5/CNTs-700 and E-TEK. (D) polarization curves of ORR on Pt/Nb_2O_5/CNTs, Pt/Nb_2O_5/CNTs-700 and E-TEK.

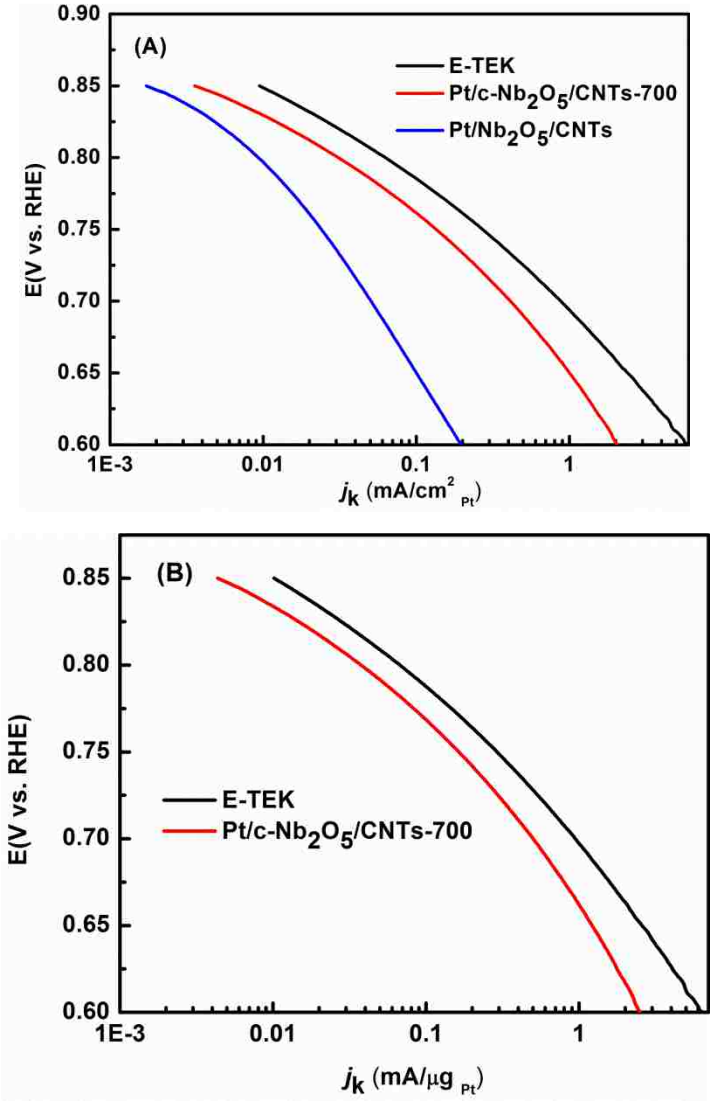

Fig. 6 Tafel plots derived from the ORR curves for various catalysts. (A) normalized to the individual ESA of Pt. (B) normalized to the mass of Pt.

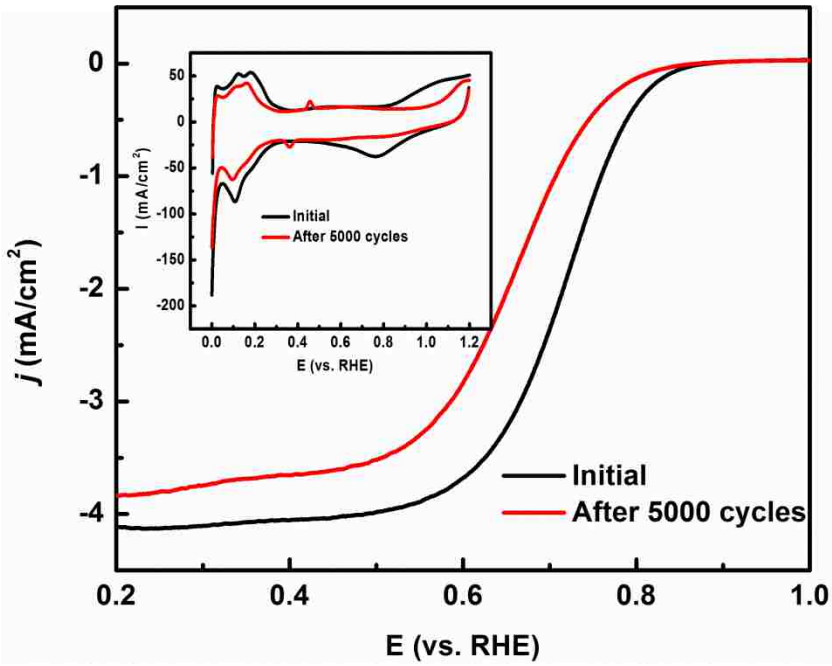

Fig. 7 Polarization curves of the ORR before and after 5000 cycles for Pt/c-Nb_2O_5/CNTs-700. The inset figure shows the CV curves before and after 5000 cycles.

2. SUMMARY AND FUTURE WORK

This work described developing catalysts and preparing air breathing cathode for hybrid lithium-air battery. In the catalysts sections, we focused on synthesizing metal oxides nanocoating on CNTs as precious metal Pt electrocatalyst support, great efforts were paid on TiO_2 and Nb_2O_5. Thermal carbon doping was the main technique used in this work to modify the metal oxides. Pt supported on c-TiO_2/CNTs showed a better oxygen reduction activity than a commercial Pt/C catalyst. The catalyst only has a less than 3% loss in activity after electrochemical cycling 5000 times, as compared to about 55% activity loss for the Pt/C catalyst. In the scenario of Pt supported on c-Nb_2O_5/CNTs, the intrinsic oxygen reduction activity and stability were inferior to the commercial Pt/C, suggesting c-Nb_2O_5/CNTs may not be suitable as an ideal support. Finally, titanium oxy carbide was synthesized by carbon doping and post thermal treatment, and titanium oxy carbide exhibited high oxygen revolution reaction activity.

In the hybrid Li-air battery section, we concentrated on developing CNTs fabricated air cathode. At high discharge densities, CNTs based cathode showed better performance than carbon black based cathode which was attributed to the high porous structure of CNTs based cathode. With mono Pt/CNTs cathode, the cell achieved a specific capacity of 306 mAh/g and a specific energy of 1067 Wh/kh, and a round trip efficiency of 72% after 10 cycles. In order to reduce the charge overpotential and extend the cell life time, a bifunctional catalyst Pt/IrO_2/CNTs was developed. It was found that the round trip

efficiency can be elevated to 81% after 10 cycles and mild degradation of cell performance was observed after 20 cycles.

Our futhre work will mainly focus on phase transition between Nb_2O_5/CNTs and NbO_2/CNTs. In Paper V it was found that carbon doping could faciliate the phase transition from Nb_2O_5/CNTs to NbO_2/CNTs at lower temperature and it was speculated that interstial carbon may expand the lattice which may possibly favor the this transition. XANES technique will be used to measure the bond length and coordinate number.

BIBLIOGRAPHY

[1] 2012 The Outlook for Energy: A View to 2040, ExxonMobile, 2012.

[2] BP Statistical Review of World Energy June 2012, BP, 2012.

[3] http://www.nissanusa.com/leaf-electric-car/index.

[4] http://www.toyota.com/prius-hybrid/.

[5] T. Nagaura and K. Tozawa, Prog. Batteries Sol. Cells, 1990, 9, 209-217.

[6] G. Girishkumar, B. McCloskey, A. C. Luntz, S. Swanson and W. Wilcke, J. Phys. Chem. Lett., 2010, 1, 2193-2203.

[7] B. Richter, D. Goldston, G. Crabtree, L. Glicksman, D. Goldstein, D. Greene, D. Kammen, M. Levine, M. Lubell, M. Savitz and D. Sperling, American Physical Society: Gollege Park, MD, 2008.

[8] P. G. Bruce, S. A. Freunberger, L. J. Hardwick and J.-M. Tarascon, Nat. Mater., 2012, 11, 19-29.

[9] K. M. Abraham and Z. Jiang, J. Electrochem. Soc., 1996, 143, 1-5.

[10] T. Zhang, N. Imanishi, Y. Shimonishi, A. Hirano, Y. Takeda, O. Yamamoto and N. Sammes, Chem.Commun., 2010, 46, 1661-1663.

[11] T. Zhang, N. Imanishi, Y. Shimonishi, A. Hirano, J. Xie, Y. Takeda, O. Yamamoto and N. Sammes, J. Electrochem. Soc., 2010, 157, A214-A218.

[12] J.-S. Lee, S. Tai Kim, R. Cao, N.-S. Choi, M. Liu, K. T. Lee and J. Cho, Adv. Energy Mater., 2011, 1, 34-50.

[13] B. Kumar, J. Kumar, R. Leese, J. P. Fellner, S. J. Rodrigues and K. M. Abraham, J. Electrochem. Soc., 2010, 157, A50-A54.

[14] H. Kitaura and H. Zhou, Adv. Energy Mater., 2012, 2, 889-894.

[15] J. Read, J. Electrochem. Soc., 2002, 149, A1190-A1195.

[16] T. Ogasawara, A. Débart, M. Holzapfel, P. Novák and P. G. Bruce, J. Am. Chem. Soc., 2006, 128, 1390-1393.

[17] J. Read, J. Electrochem. Soc., 2006, 153, A96-A100.

[18] A. Débart, J. Bao, G. Armstrong and P. G. Bruce, J. Power Sources, 2007, 174, 1177-1182.

[19] I. Kowalczk, J. Read and M. Salomon, Pure Appl. Chem., 2007, 79, 851-860.

[20] J. S. Hummelshoj, J. Blomqvist, S. Datta, T. Vegge, J. Rossmeisl, K. S. Thygesen, A. C. Luntz, K. W. Jacobsen and J. K. Norskov, J. Chem. Phys., 2010, 132, 071101-071104.

[21] C. O. Laoire, S. Mukerjee, K. M. Abraham, E. J. Plichta and M. A. Hendrickson, J. Phys. Chem. C, 2009, 113, 20127-20134.

[22] P. Albertus, J. Christensen, G. Girishkumar, B. McCloskey and A. Luntz, Meeting Abstracts, 2010, MA2010-02, 339.

[23] K. Xu, Chem. Rev., 2004, 104, 4303-4418.

[24] D. Aurbach, J. Power Sources, 2000, 89, 206-218.

[25] S. A. Freunberger, Y. Chen, N. E. Drewett, L. J. Hardwick, F. Bardé and P. G. Bruce, Angew. Chem. Int. Ed., 2011, 50, 8609-8613.

[26] R. R. Mitchell, B. M. Gallant, C. V. Thompson and Y. Shao-Horn, Energy & Environmental Science, 2011, 4, 2952-2958.

[27] V. Giordani, S. A. Freunberger, P. G. Bruce, J.-M. Tarascon and D. Larcher, Electrochem.Solid-State Lett., 2010, 13, A180-A183.

[28] S. J. Visco, B. D. Katz, Y. S. Nimon and L. C. D. Jonghe, Protected Active Metal Electrode and Battery Cell Structure with Non-aqueous Interlayer Architecture. U.S. Patent # 7282295, 2007.

[29] J. Fu, Lithium ion conductive glass-ceramics and electric cells and gas sensors using the same. U.S. Patent # 6485622, 2002.

[30] A. J. Cowan, J. Tang, W. Leng, J. R. Durrant and D. R. Klug, J. Phys. Chem. C, 2010, 114, 4208-4214.

[31] L. Li, X. Zhao and A. Manthiram, Electrochem. Commun., 2012, 14, 78-81.

[32] E. Yoo and H. Zhou, ACS Nano, 2011, 5, 3020-3026.

[33] Y. Li, K. Huang and Y. Xing, Electrochim. Acta, 2012, 81, 20-24.

[34] P. Stevens, G. Toussaint, G. Caillon, P. Viaud, P. Vinatier, C. Cantau, O. Fichet, C. Sarrazin and M. Mallouki, ECS Transactions, 2010, 28, 1-12.

[35] P. He, Y. Wang and H. Zhou, Electrochem. Commun., 2010, 12, 1686-1689.

[36] O. Crowther, B. Meyer, M. Morgan and M. Salomon, J. Power Sources, 2011, 196, 1498-1502.

[37] L. Jörissen, J. Power Sources, 2006, 155, 23-32.

[38] Y. Xing, Y. Cai, M. B. Vukmirovic, W.-P. Zhou, H. Karan, J. X. Wang and R. R. Adzic, J. Phys. Chem. Lett., 2010, 1, 3238-3242.

[39] J. Zhang, M. B. Vukmirovic, K. Sasaki, A. U. Nilekar, M. Mavrikakis and R. R. Adzic, J. Am. Chem. Soc., 2005, 127, 12480-12481.

[40] H. A. Gasteiger, S. S. Kocha, B. Sompalli and F. T. Wagner, Appl. Catal. B: Environmental, 2005, 56, 9-35.

[41] J. Suntivich, H. A. Gasteiger, N. Yabuuchi and Y. Shao-Horn, J. Electrochem. Soc., 2010, 157, B1263-B1268.

[42] B. E. Conway and T. C. Liu, Langmuir, 1990, 6, 268-276.

[43] S. Song, H. Zhang, X. Ma, Z. Shao, R. T. Baker and B. Yi, Int. J. Hydrogen Energy, 2008, 33, 4955-4961.

[44] R. E. Fuentes, J. Farell and J. W. Weidner, Electrochem. Solid-State Lett., 2011, 14, E5-E7.

[45] J. Suntivich, K. J. May, H. A. Gasteiger, J. B. Goodenough and Y. Shao-Horn, Science, 2011, 334, 1383-1385.

[46] Y.-C. Lu, Z. Xu, H. A. Gasteiger, S. Chen, K. Hamad-Schifferli and Y. Shao-Horn, J. Am.Chem.Soc., 2010, 132, 12170-12171.

[47] T. Ioroi, N. Kitazawa, K. Yasuda, Y. Yamamoto and H. Takenaka, J. Electrochem. Soc., 2000, 147, 2018-2022.

[48] T. Ioroi, N. Kitazawa, K. Yasuda, Y. Yamamoto and H. Takenaka, J. Appl. Electrochem., 2001, 31, 1179-1183.

[49] S.-D. Yim, W.-Y. Lee, Y.-G. Yoon, Y.-J. Sohn, G.-G. Park, T.-H. Yang and C.-S. Kim, Electrochim. Acta, 2004, 50, 713-718.

[50] F.-D. Kong, S. Zhang, G.-P. Yin, N. Zhang, Z.-B. Wang and C.-Y. Du, Electrochem. Commun., 2012, 14, 63-66.

[51] A. Rabis, P. Rodriguez and T. J. Schmidt, ACS Catalysis, 2012, 2, 864-890.

[52] L. Li and Y. Xing, J. Electrochem. Soc., 2006, 153, A1823-A1828.

[53] S. K. Natarajan and J. Hamelin, J. Electrochem. Soc., 2009, 156, B210-B215.

[54] L. Li and Y. Xing, J. Power Sources, 2008, 178, 75-79.

[55] Y. Xing, J. Phys. Chem. B, 2004, 108, 19255-19259.

[56] K. J. J. Mayrhofer, J. C. Meier, S. J. Ashton, G. K. H. Wiberg, F. Kraus, M. Hanzlik and M. Arenz, Electrochem. Commun., 2008, 10, 1144-1147.

[57] J. Osman, J. Crayston, A. Pratt and D. Richens, J. Sol-Gel Sci. Tech., 2007, 44, 219-225.

[58] E. Formo, E. Lee, D. Campbell and Y. Xia, Nano Letters, 2008, 8, 668-672.

[59] A. Bauer, K. Lee, C. Song, Y. Xie, J. Zhang and R. Hui, J. Power Sources, 2010, 195, 3105-3110.

[60] L. Zhang, L. Wang, C. M. B. Holt, B. Zahiri, Z. Li, K. Malek, T. Navessin, M. H. Eikerling and D. Mitlin, Energy & Environmental Science, 2012, 5, 6156-6172.

[61] F. C. Walsh and R. G. A. Wills, Electrochim. Acta, 2010, 55, 6342-6351.

[62] W.-Q. Han and Y. Zhang, Appl. Phys. Lett., 2008, 92, 203117-203113.

[63] X. Li, A. L. Zhu, W. Qu, H. Wang, R. Hui, L. Zhang and J. Zhang, Electrochim. Acta, 2010, 55, 5891-5898.

[64] T. Ioroi, H. Senoh, S.-i. Yamazaki, Z. Siroma, N. Fujiwara and K. Yasuda, J. Electrochem. Soc., 2008, 155, B321-B326.

[65] T. Tsumura, Y. Hattori, K. Kaneko, Y. Hirose, M. Inagaki and M. Toyoda, Desalination, 2004, 169, 269-275.

[66] M. Toyoda, T. Yano, B. Tryba, S. Mozia, T. Tsumura and M. Inagaki, Appl. Catal. B: Environmental, 2009, 88, 160-164.

[67] Y. Liu, J. M. Szeifert, J. M. Feckl, B. Mandlmeier, J. Rathousky, O. Hayden, D. Fattakhova-Rohlfing and T. Bein, ACS Nano, 2010, 4, 5373-5381.

[68] N. R. Elezovic, B. M. Babic, V. R. Radmilovic, L. M. Vracar and N. V. Krstajic, Electrochim. Acta, 2011, 56, 9020-9026.

[69] S.-Y. Huang, P. Ganesan and B. N. Popov, Appl. Catal. B: Environmental, 2010, 96, 224-231.

[70] N. R. Elezovic, B. M. Babic, L. Gajic-Krstajic, V. Radmilovic, N. V. Krstajic and L. J. Vracar, J. Power Sources, 2010, 195, 3961-3968.

[71] R. Hahn, F. Schmidt-Stein, J. Salonen, S. Thiemann, Y. Song, J. Kunze, V.-P. Lehto and P. Schmuki, Angew. Chem. Inter. Ed., 2009, 48, 7236-7239.

[72] K. Huang, K. Sasaki, R. R. Adzic and Y. Xing, J. Mater. Chem., 2012, 22, 16824-16832.

[73] S. Tominaka, Chem. Commun., 2012, 48, 7949-7951.

[74] J. X. Wang, N. M. Markovic and R. R. Adzic, J. Phys. Chem. B, 2004, 108, 4127-4133.

[75] K. Sasaki, L. Zhang and R. R. Adzic, Phys. Chem. Chem. Phys., 2008, 10, 159-167.

[76] L. Zhang, L. Wang, C. M. B. Holt, T. Navessin, K. Malek, M. H. Eikerling and D. Mitlin, J. Phys. Chem. C, 2010, 114, 16463-16474.

[77] D. Eder, I. A. Kinloch and A. H. Windle, Chem. Commun., 2006, 1448-1450.

[78] D. Eder and A. H. Windle, J. Mater. Chem., 2008, 18, 2036-2043.

[79] D. Eder and A. H. Windle, Adv. Mater., 2008, 20, 1787-1793.

VITA

Mr. Kan Huang was born in 1984 in China. He earned a bachelor's degree in Chemical Engineering from China University of Petroleum in 2006, and a master's degree also in Chemical Engineering from East China University of Science and Technology in 2009. He entered Missouri University of Science and Technology in January, 2010 and obtained his Doctor of Philosophy in Chemical Engineering from Department of Chemical and Biochemical Engineering in May, 2013.